Master of science in AEROSPACE ENGINEERING

A.a. 2024/2025

Graduation Session July 2025

Solar-Sail trajectory optimization for close proximity operations and rendezvous of space debris

Supervisors:
Prof. Lorenzo Casalino
Prof. Jeannette Heiligers
Ir. Andrea Minervino Amodio

Candidate:
Margherita Michahelles

Abstract

Active debris removal (ADR) is recognized as one of the most effective strategies to address the ever-increasing problem of space debris. This thesis highlights the potential of solar sailing as a propellant-free propulsion method that offers an unlimited ΔV budget suitable for multiple debris removal missions. Traditional proximity operations are considered and their feasibility when using a solar sail is established for Low Earth Orbit (LEO) scenarios where space debris density is higher. Given the unique dynamics of solar sails, the study explores alternative trajectories such as Hold trajectories and Walking Safety Ellipses for target inspection, which improve passive safety by maintaining a collision-free path even in the event of sail failure. The transfer from a far-range phase point to an Inspection Loop is then examined. GPOPS-II, a software based on direct collocation methods, is employed to optimise these trajectories and to evaluate the effectiveness of these methods in addressing optimisation challenges specific to close-proximity operations. The results demonstrate that the proposed Hold and Inspection Loop Trajectories enable a safe approach to target debris, potentially reducing overall ADR mission costs due to the sailcraft's propellantless nature.

Acknowledgements

This thesis is the result of seven months of work and marks the conclusion of my university studies. These university years have been intense, fun, and at times tiring. Still, when I look back, I have wonderful memories, and for this, I must thank many people who have been close to me, motivating and supporting me.

First of all, I would like to thank my supervisors at TU Delft, Prof. Jeannette Heiligers and Ir. Andrea Minervino Amodio. I want to thank Jeannette for placing her trust in me and allowing me to gain this experience at TU Delft from October 2024, giving me the opportunity to conduct some of my thesis work in her "PhD room" at the Department of Astrodynamics, be among her thesis students, develop a passion for this field, and expand my knowledge of the fascinating field of solar sails. I would also like to thank Andrea, who has supported me throughout this period, especially in the last few months, despite being in very different time zones and attending meetings at very early hours for him. Thank you both for your passion, experience, and attention to detail. I come away from this experience greatly enriched in terms of technical knowledge and personal growth.

I would like to thank Prof. Anli V. Rao from the University of Florida for his generosity and incredible availability. He provided me with a GPOPS-II license and support for it, without which I could not have conducted this thesis research.

I would also like to thank Prof. Casalino, whose lectures on space propulsion sparked my interest in orbital mechanics and advanced propulsion. He agreed to supervise me in this thesis work and, even from a distance, was always available to answer any questions I had. His help was truly fundamental.

A big thank you also goes to my oldest friends in Florence and to all those I have met over the years since I moved to Turin six years ago, as well as to my most recent friends in Delft. I am very grateful to all of you. It is not something to be taken for granted, and it takes a lot of luck to find good friends. To my friends in Turin, thank you. Thanks to you, I now think of Turin as a second home. Alessandra, Matilde, and Virginia, with your enthusiasm, you made everything feel lighter, from all the exam sessions to everyday life. With you, I've shared some of my most unforgettable adventures. To my colleagues and friends from the student teams at Politecnico, with a special mention to Gloria, thank you for motivating me academically through our projects and for the valuable experiences we shared. To my friends in Florence, thank you. Even though we don't see each other for months at a time, you are always there. This is especially true with Eleonora and Irene, who have been close to me all these years. To my friends in Delft, some of whom I found again from Turin, and others I met there, thank you because even though I was in another country, I immediately felt at home. Thank you to Giuseppe and Riccardo, who shared with me these months of thesis work and life in the Netherlands.

Last but not least, thank you to my family and thank you to my sisters, Beatrice and Domitilla, who have always supported me and are always there.

Table of Contents

List of Figures

List of Tables

Nomenclature

Table 1: Abbreviations

Abbreviation	Definition
ACS3	Advanced Composite Solar Sail System
ADR	Active Debris Removal
CW	Clohessy–Wiltshire equations
ECI	Earth-Centered Inertial frame
ESA	European Space Agency
GPOPS-II	General Purpose Optimal Control Software II
IL	Inspection Loop
IR	Infrared
JAXA	Japan Exploration Agency
KOE	Keep-Out Ellipsoid
KOS	Keep-Out Sphere
KOZ	Keep-Out Zone
LEO	Low Earth Orbit
LiDAR	Light Detection and Ranging
LVLH	Local Vertical Local Horizontal frame
NASA	National Aeronautics and Space Administration
NLP	Nonlinear Programming
NFOV	Narrow Field-of-View camera
OCP	Optimal Control Problem
RAAN	Right Ascension of the Ascending Node
RPOs	Rendezvous and Proximity Operations
SE	Safety Ellipse
SRP	Solar Radiation Pressure
SSA	Solar Sail Acceleration
ToF	Time-of-Flight
WFOV	Wide Field-of-View camera

Table 2: Latin Symbols

Symbol	Definition
a	Orbit semi-major axis
a_0	Characteristic acceleration of the sail
a, b, c	Semi-axes of the keep-out ellipsoid
e	Orbit eccentricity
i	Orbit inclination
J	Objective functional (cost)
M	Mesh intervals
n	Mean motion of the target orbit
n	Sail normal unit vector
r	Magnitude of the position vector
S	Sun-sail line reference frame
t	Time
t_f	Final optimization time
t_{obs}	Observation start time
u, $u(t)$	Control vector (sail attitude)
x, y, z	Coordinates in the LVLH frame
$\dot{x}, \dot{y}, \dot{z}$	Velocity components in the LVLH frame
$x_{\max}, z_{\max}$	Maximum offsets of the safety ellipse
y_c	In-track offset of the safety ellipse centre

Table 3: Greek Symbols

Symbol	Definition
α	Cone angle
β	Sail lightness number
χ	In-plane phase angle
δ	Clock angle
δ_r	tolerance on position
δ_r	tolerance on velocity
ϵ	Tolerance threshold
η	Eclipse factor (shadow function)
ϕ	Hyperbolic tangent function
μ	Earth's gravitational parameter
ν	True anomaly
ρ	Initial radial offset or ellipsoid radius
σ^*	Critical sail loading

Table 4: Subscripts (Indices)

Subscript	Definition
$\odot$	Sun
$\oplus$	Earth

Chapter 1

Introduction

Since the beginning of space exploration, the number of artificial objects in orbit—ranging from decommissioned satellites to mission-related debris—has steadily increased, raising serious concerns regarding space traffic and the risk of collisions. Low Earth Orbit (LEO) [1] has become increasingly congested, populated by miniaturized space systems and large constellations. The dominant sources of space debris are fragmentation and collision, such as the 2009 collision between Cosmos and Iridium satellites [2] and accidental or intentional fragmentations, like the 2007 destruction of the Chinese Fengyun satellite, or more recently in 2023 the VESPA adapter, a target selected for the ClearSpace-1 debris removal mission, which due to fragmentation had to be replaced [3].

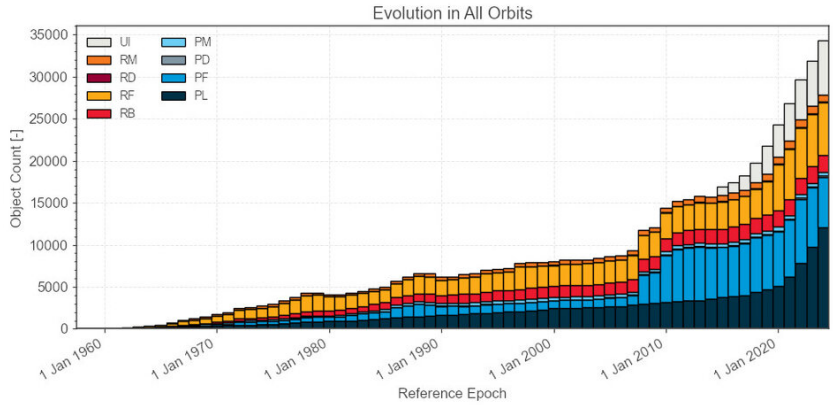

Figure 1.1: Spatial and temporal distribution of space debris and orbital objects [1].

As of August 2024, ESA estimates over 54,000 objects larger than 10 cm are in orbit, including 9,300 active payloads, along with 1.2 million objects between 1-10 cm and 130 million between 1 mm–1 cm. Figure 1.1 clearly shows that the number of space debris has grown quickly since the 1960s. Objects are classified as PL (active payloads), PF/RF (fragmentation debris), RB (rocket bodies), and UI (unidentified).

Space debris mitigation guidelines have been identified to protect the space environment from the "Kessler Syndrome", which predicted the formation of a debris belt in 1978 [4, 5].

A first mitigation measure was the reduction of post-mission lifetime limit from 25 down to 5 years [6]. However post-mission disposal alone may not be sufficient in highly congested orbital regions, indicating a crucial role for active debris removal (ADR) strategies [7] as shown in Fig. 1.2. Simulations conducted by NASA show that removing as few as 5 to 20 high-risk objects per year can significantly slow debris growth until stabilizing the space environment for the next 200 years [8, 9]. These findings demonstrate how ADR must be considered as an option to preserve near Earth space.

There are several Active Debris Removal (ADR) missions which have been launched or are currently under development to validate key technologies. The RemoveDEBRIS mission, led by the University of Surrey, demonstrated experimental capture techniques such as a net and harpoon system for debris collection [10]. The ELSA-d mission, launched by Astroscale and JAXA in April 2021, is operating in orbit to test technologies for rendezvous, capture, and de-orbiting of defunct objects [11]. In parallel, ESA's CleanSpace initiative is advancing preparations for ClearSpace-1, a mission aimed at removing a specific non-cooperative payload using robotic arms, while also serving as a platform for validating proximity operations in orbit [12].

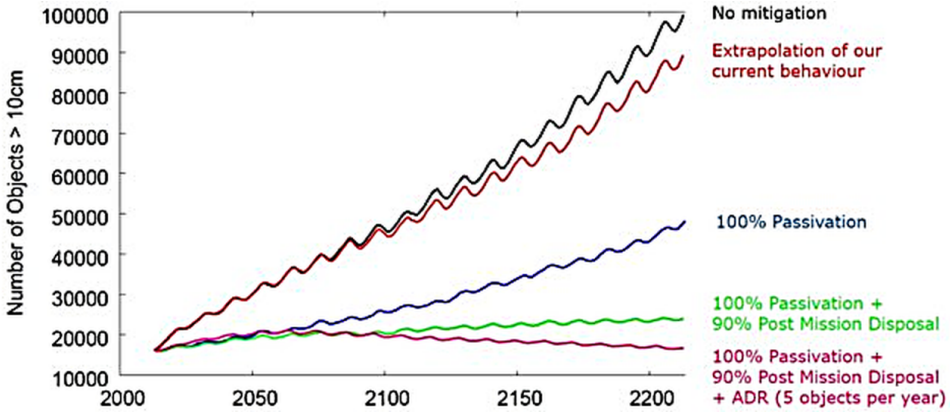

Figure 1.2: Evolution of space debris environment and effectives of mitigation measures [7].

Most ADR demonstration missions currently in flight or planned are based on conventional propulsion systems, such as chemical or electric thrusters. These systems offer high manoeuvrability, allowing the spacecraft to actively target and rendezvous with debris objects. However, their effectiveness is limited by the constrained amount of propellant that can be stored on board, which directly affects the mass of the spacecraft and the cost of the mission. An alternative approach to conventional propulsion in ADR missions involves the use of propellant-free systems, such as solar sails, which leverage the momentum of Sun-emitted photons to generate thrust. As outlined by McInnes in Fig. 1.3 [13], for conventional propulsion systems, the specific impulse (I_{sp}) characterizes performance, as described by the Tsiolkovsky equation. Since a solar sail operates without propellant consumption, its mass remains constant, resulting in an effectively infinite I_{sp}. However, this is not valid for finite-time missions if the sail is a low-performance one. In such cases,

solar sails are only competitive over long durations. While low-performance sails require extended timescales to be effective, high-performance solar sails can quickly outperform conventional propulsion systems.

A few examples of flown missions are: IKAROS, the first full solar-sailing demonstration, NanoSail-D (2010) by NASA, LightSail-1 & 2[14], for Earth-bound missions and the more recent ACS3 [15], currently in orbit. These missions have primarily focused on validating sail deployment and flight capabilities.

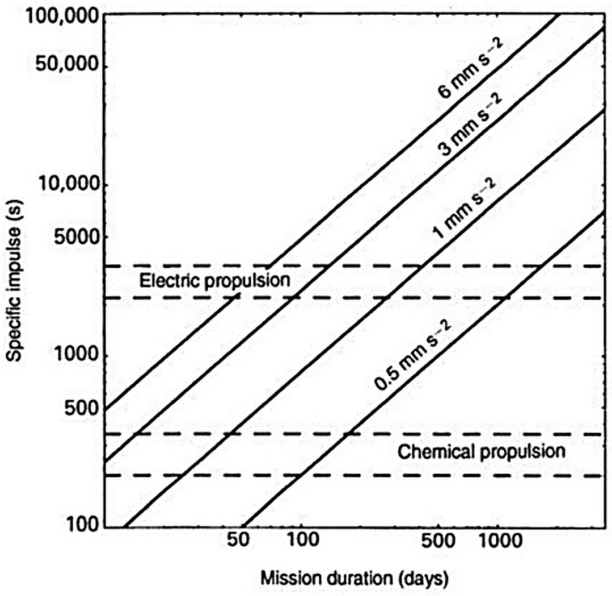

Figure 1.3: Solar sail effective I_{sp} as a function of mission duration at 1 au [13].

While solar sails have been extensively studied for interplanetary missions, their application to Rendezvous and Proximity Operations (RPOs) remains almost unexplored. Proximity operations that include far range operations, close proximity operations, final approach and docking, have been studied for spacecraft employing conventional propulsion systems [16] but they present significant challenges due to the dynamic constraints and safety considerations, especially if the target is uncooperative like a space debris. The use of a solar sail for debris removal around Earth, has been studied in [17, 18], demonstrating a successful orbit transfer from a lower parking orbit to the target orbit in LEO. In this context, the sailcraft serves as a chaser, moving between multiple non-cooperative debris targets within a single ADR mission.

The SWEEP (Space Waste Elimination around Earth by Photon Propulsion) project also follows this principle, exploiting solar-sailing technologies to "clean up space and preserve the near-Earth environment"[19]. As part of the above-mentioned project, research has been conducted on close-proximity operations in ADR missions using solar sails. It was shown that far-range operations are feasible and the concept of hold trajectories (instead of traditional hold points required in this mission phase) was introduced, accounting for operational and dynamical constraints [20]. This leads to the need of filling the research

gap on the next phase of RPOs: close-range rendezvous operations and their feasibility using solar-sail propulsion.

1.1 Research Objective and Questions

This research aims to investigate the feasibility and performance of solar-sail-based ADR missions, with a particular focus on the close-range phase of rendezvous operations. Previous studies have primarily addressed the phasing and far-range rendezvous phases — demonstrating successful orbit transfers from lower parking orbits to target orbits in LEO, and showing the feasibility of hold trajectories under solar-sail constraints . Instead, close-range operations remain largely unexplored [17, 20].

During proximity operations with solar sails, hold trajectories — time-flexible paths where the chaser can remain indefinitely — are employed instead of fixed hold points. This is because the unique dynamics and operational constraints of solar sails make it infeasible to maintain a hold point, as the sail inevitably drifts over time. Building upon the far-range research, this work explores whether similar strategies can be applied in the close-range domain.

The objective of this thesis is to design optimal close-proximity trajectories toward a non-cooperative target, while considering solar-sail dynamics and enforcing safety constraints. RPOs with non-cooperative targets represent the most critical segment of ADR missions. Given the collision risk with passive debris, a robust trajectory optimization is essential. The optimal control problem is solved using direct collocation methods implemented through GPOPS-II, aiming to produce feasible and safe trajectories for ADR missions with solar sails.

The initial state vector for the relative motion is defined following standard RPO strategies, with the chaser located behind the target along the negative V-bar direction. The final position is defined at a relative distance of about 40-50 m, accounting for realistic navigation uncertainties, including GPS and relative position estimation errors.

To connect the far-range rendezvous phase with close-proximity operations, an intermediate transfer segment is also investigated. During the trajectory design, Keep-Out Zones (KOZs) are defined around the target to ensure safety. Within this framework, inclined passive-safe trajectories are considered, using the safety ellipse concept as a dynamic hold trajectory. A walking safety ellipse, also referred to in the literature as a spiralling approach, is then employed for close-range inspection and target characterization [21].

Therefore the subject of this work is to answer the following research questions:

1. What does an optimal trajectory for close-range operations look like with solar-sail propulsion?

2. Is direct collocation accurate, robust and suitable to obtain optimal close-range trajectories incorporating the main constraints?

    - *Accurate*: Does it compute trajectories that satisfy dynamics and constraints with sufficient precision not only at the collocation nodes?

- *Robust*: Can it consistently find feasible solutions even with uncertain inputs or poor initial guesses?
- *Suitable*: Is it capable of handling complex constraints (e.g., keep-out zones) efficiently?

By addressing these questions, this work contributes to the understanding of if and how solar sails can be effectively utilized in constrained proximity operations and provides a foundation for future investigation for RPOs using solar-sail propulsion.

1.2 Thesis Outline

This thesis has the following outline to address the research questions on close-proximity operations using solar-sail propulsion previously presented.

The methodology employed is presented in Chapter 2 . It begins with a review of solar-sail fundamentals and environmental models, followed by an overview of proximity-operations phases, direct-collocation optimization problems and setup of the software GPOPS-II.

The results are presented in two dedicated chapters: Chapter 3 analyses Hold Trajectories (Safety Ellipse), presents the Inspection Loop, and proposes a transfer strategy; Chapter 4 investigates, through a parametric analysis, different scenarios for the Safety Ellipse case, exploring different: altitudes, orbit geometries, AA, characteristic acceleration (a_c) and initial true anomaly.

In Chapter 5 conclusions are drawn: first the key findings are summarised, then the research questions are answered, and then recommendations are offered for future work.

Appendix provides (A) verification and validation details, Appendix (B) includes GPOPS-II input configurations and sensitivity results, and Appendix (C) contains additional figures and tables.

Chapter 2

Methodology

This chapter presents the assumptions used for the environmental and dynamic model and the setting of the optimisation problem used for the simulation of proximity operations with a solar sail. First, the reference frames are defined, including the inertial, co-moving (LVLH), and Sunlight frame. Then, the main phases of rendezvous and proximity operations are described, including the assumptions made on the sensors and the safety constraints (like the KOZs).

The dynamical model used for the sailcraft is then introduced. The model includes the Clohessy-Wiltshire equations defined in the LVLH frame and the SRP acceleration using an ideal flat sail.

Next, a brief overview of commonly used optimisation methods is presented. This work employs direct collocation as its chosen solution method, implemented using the GPOPS-II software.

Finally, the simulation and optimization setup is presented. This includes the initial conditions, the sail parameters, the definition of the optimization problems for the hold phase, the inspection loop, and the transfer trajectory.

2.1 Reference Frames

This study employs three primary reference frames to model spacecraft dynamics and control: the Sunlight reference frame, the Earth-Centred Inertial (ECI) frame, and the Local Vertical Local Horizontal (LVLH), also referred to as co-moving frame.

Sunlight Reference Frame The Sunlight reference frame (S), $O_S(\hat{x}_S, \hat{y}_S, \hat{z}_S)$, is centred on the sailcraft and is used to model the orientation of the sail with respect to incident sunlight. The $\hat{x}_S$-axis is aligned with the sunlight direction $\hat{s}$ (from Sun to sail), the $\hat{y}_S$-axis is given by $\hat{y}_S = \hat{Z}_I \times \hat{s}$, and $\hat{z}_S$ completes the right-handed set [17, 22].

The transformation matrix from the Sunlight frame to the ECI (I) frame is:

$$\mathbf{R}_{S\to I} = \begin{bmatrix} -\cos\alpha_\odot \cos\delta_\odot & \sin\alpha_\odot & -\cos\alpha_\odot \sin\delta_\odot \\ -\sin\alpha_\odot \cos\delta_\odot & -\cos\alpha_\odot & -\sin\alpha_\odot \sin\delta_\odot \\ -\sin\delta_\odot & 0 & \cos\delta_\odot \end{bmatrix} \tag{2.1}$$

where $\alpha_\odot$ and $\delta_\odot$ are the right ascension and declination of the Sun, respectively.

Earth-Centred Inertial (ECI) Frame The ECI frame, $\mathcal{I}(X, Y, Z)$, is a non-rotating inertial frame with origin at Earth's centre. The $\hat{X}$-axis points toward the mean vernal equinox (J2000 epoch), the $\hat{Z}$-axis aligns with Earth's mean rotation axis, and the $\hat{Y}$-axis completes the right-handed triad. This frame serves as the baseline for defining motion and transformations of all other frames [23].

Local Vertical Local Horizontal (LVLH) Frame The LVLH, or co-moving frame, is a rotating reference frame centred on the target spacecraft in orbit. It is defined by:

- $\hat{i}$ (R-bar): along the radial vector $\vec{r}_A/|\vec{r}_A|$.
- $\hat{k}$ (H-bar): orbit angular momentum vector $\vec{h}_A = \vec{r}_A \times \vec{v}_A$.
- $\hat{j}$ (V-bar): completes the triad, $\hat{j} = \hat{k} \times \hat{i}$.

This frame, shown in Fig. 2.1, is commonly used in relative motion analysis [16] to simplify the equations for rendezvous dynamics.

The rotation matrix from ECI to LVLH is:

$$[\mathbf{Q}]_{\mathbf{I}\to\mathbf{x}} = \begin{bmatrix} \hat{\imath}_x & \hat{\jmath}_x & \hat{k}_x \\ \hat{\imath}_y & \hat{\jmath}_y & \hat{k}_y \\ \hat{\imath}_z & \hat{\jmath}_z & \hat{k}_z \end{bmatrix} \tag{2.2}$$

Utility in Proximity Operations

Using the LVLH frame allows to express conveniently the relative position $\vec{\delta r}$ and velocity $\vec{\delta v}$ of the chaser spacecraft as the chaser approaches the target. This reference frame simplifies equations of motion, such as the Clohessy-Wiltshire or Hill-Clohessy-Wiltshire (HCW) equations, which describe linearized relative dynamics near circular orbits [23].

The LVLH frame is critical for onboard guidance, navigation, and control (GNC) systems, especially when dealing with constraints such as line-of-sight limitations, sensor fields of view, and approach direction preferences (e.g., V-bar or R-bar approaches).

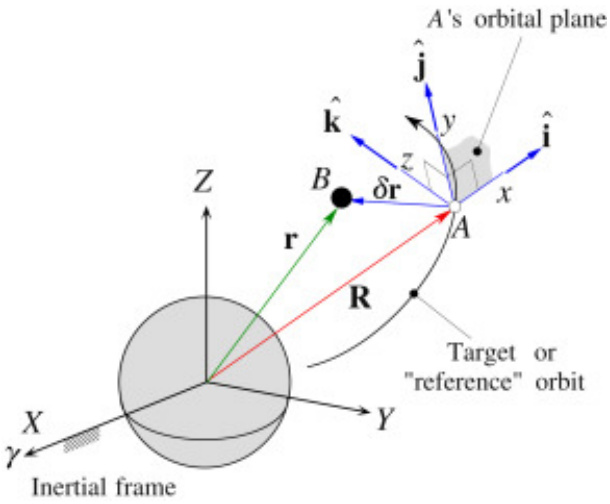

Figure 2.1: Co-moving LVLH reference frame attached to A (target), from which the body B (chaser) is observed.

2.2 Rendezvous and Proximity Operations

The purpose of this first section is to give an overview on the main phases of a rendezvous approach, based on [16].

Main phases of a rendezvous mission

Rendezvous and proximity operations (RPO) are divided in: **launch, phasing, far-range rendezvous, close-range rendezvous** and **mating**.

During the launch, a chaser spacecraft is injected into the orbital plane of the target[1], constrained by a specific launch window to minimize phase angle and plane change requirements.

The first major phase, *phasing*, aims to reduce the phase angle between the chaser and the target through a series of orbital manoeuvrers such as perigee/apogee raising or Hohmann transfers. These manoeuvrers correct injection errors and gradually bring the chaser to an *initial aim point*, also known as the *entry gate*. This gate is located near the target's orbit and is strategically chosen based on factors like sensor range, docking axis orientation, and safety. The final phasing manoeuvrer must place the chaser within the acquisition range of the far-range relative navigation sensors. The most convenient solution to locate this point is behind (V-bar) and slightly below (R-bar) the target, because the natural drift will move the chaser slowly toward the target without needing propelled correction manoeuvres. During launch and phasing, navigation is based on absolute measurements in an Earth-Centred inertial frame.

The *far-range rendezvous* phase or 'homing' begins at distances on the order of 10

[1]The chaser will be launched into a 'virtual' target plane, as the target orbit plane will drift with time.

km and continues until the chaser closes in to a few kilometres from the target. In this phase, the chaser trajectory, using a co-moving frame centred on the target, is guided using relative navigation sensors. The major objectives of this phase are: the acquisition of the target orbit, the reduction of approach velocity and the synchronisation of the mission timeline. Hold points may be inserted in this phase, serving as time-flexible waiting zones where the chaser can remain without active propulsion. These allow synchronization of the mission timeline with external elements such as communication windows or Sun illumination.

During the *close-range rendezvous*, safety-critical operations dominate. All out-of-plane errors, such as inclination and right ascension of the ascending node (RAAN), must be corrected to match the accuracy of in-plane errors. This phase includes *closing*—a preparatory trajectory aligning the chaser with the final approach corridor—and the *final approach*, where specific mating conditions in position, velocity, attitude, and angular rates must be met. The approach can follow either a V-bar (velocity vector) or R-bar (radial vector) trajectory Fig. 2.2. In V-bar approaches, closing and final approach phases often merge due to the constant direction of motion. For R-bar strategies, transition trajectories such as fly-around or radial transfers are employed to safely align the chaser with the target corridor.

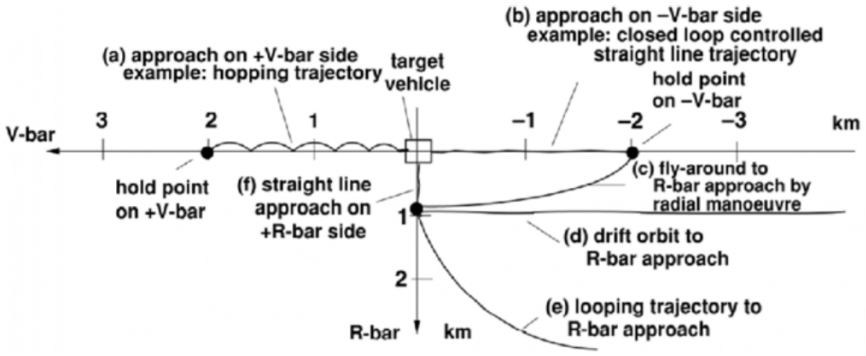

Figure 2.2: V-bar and R-bar final approach.

The final stage, *mating*, involves either docking or berthing. Docking is an active procedure where the chaser controls the approach to align and engage with the docking interface of the target. In contrast, berthing uses robotic arms or external grappling mechanisms to capture and secure the chaser. In both cases, the process must ensure a condition of no escape, attenuation of residual motion, alignment of capture interfaces, and establishment of a rigid structural connection.

Keep-Out Zones (KOZs)

Safety is the primary design driver during RPOs (far and close operations). To minimize the risk of collision with the target spacecraft or debris, the rendezvous trajectory must be carefully planned to account for navigation uncertainties and the physical dimensions of both the chaser and the target. The basic concept of safe relative trajectory design is to

define a series of nested *Keep-Out Zones* (KOZ) around the target Fig. 2.3. These zones are constructed based on the estimated navigation uncertainty at different stages of the approach and become increasingly restrictive as the chaser approaches.

The sizing of the KOZs used in this work is based on the following references [12, 24, 25, 26]. The KOZs considered are:

- **Keep-out Sphere (KOS)**: represents the inner keep-out volume, whose size is based on the geometry of both the chaser and the target. It is defined as a sphere, centred on the target, with a radius equal to the worst-case sum of the radii of the chaser and target, plus the maximum position uncertainty (σ) and a safety factor κ (which can be either 1.5 or 2). Entry in the KOS is permitted when the target has been fully inspected and when the closing and mating phases start. If a target of 0.58 m hard-body radius is considered (as in the case of PROBA-1, the target of the ClearSpace-1 Mission [27]), and a radius of 7 m is assumed for the solar sail (as in ACS3 [15]), and a 1σ uncertainty of 10 m per Cartesian component is assumed, the resulting total positional 1σ uncertainty is approximately 17.5 m. This leads to the following radius of the KOS:

  $$r_{KOS} = \kappa(r_{chaser} + r_{taregt} + 1\sigma) \approx 50m \tag{2.3}$$

  We can confirm that this value is accurate and that a similar value was used in the ADRAS-J mission [28].

- **Keep-out Ellipsoid (KOE)**: defines the outer safety volume, also referred to as the *approach zone*. The chaser enters the KOE after an in-flight inspection of the target. It is determined by the sum of the maximum target error and the expected navigation uncertainty (3σ= 10 m) of the onboard navigation system (e.g., GPS), multiplied by a safety factor κ [24]. Considering a=c, the semi-minor axes of the ellipsoid, and b the semi-major axis, the following values are obtained applying a κ = 2. A value of $3\sigma_{tracker}$ of 358 m is chosen for the daily target uncertainty along-track (AT) direction [25]:

  $$b_{KOE} = \kappa(\sigma_{\text{chaser}} + \sigma_{\text{target}}) \approx 740\,\text{m} \tag{2.4}$$

  For the cross-track (CT) and radial direction (RA) the uncertainty 3σ is evaluated with the following proportion CT:AT $\approx$ 0.4:1 found in [25].

  $$a_{KOE} = c_{KOE} = \kappa(\sigma_{\text{chaser}} + \sigma_{\text{target}}) \approx 160\,\text{m} \tag{2.5}$$

Main navigation sensors for RPOs

During the final kilometres of an autonomous rendezvous, the chaser's navigation performance must transition from a coarse, hundred-of-meter accuracy to ten/few meters. To support the whole phase of proximity-operations Active Debris Removal (ADR) and On-Orbit-Servicing (OOS) servicers are equipped with a set of sensors, including the

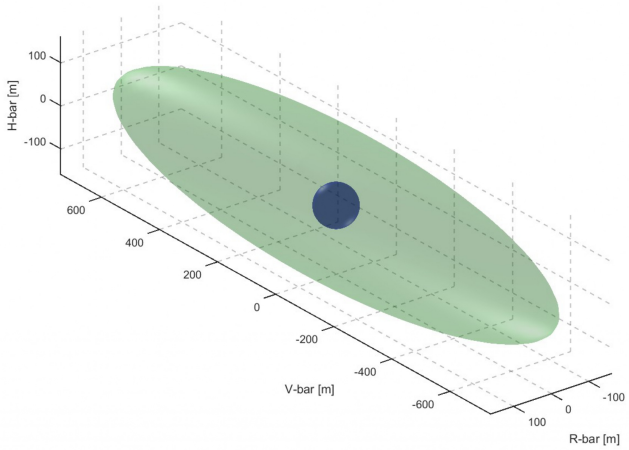

Figure 2.3: Keep-Out Zones: KOE in green and KOS in blue.

ones in Tab. 2.1 which ensure redundancy and robustness. Wide-Field-of-View (WFOV) cameras maintain target vision up to a maximum distance of ∼50 km, while Narrow-Field cameras are used up to a maximum distance from the target of ∼10 km, and relative navigation sensors such as LiDAR provide information even at close ranges. An infrared (IR) thermal camera will also be used to take measurements in poor lighting conditions. The data of the navigation sensors used in the table are from the following references [21],[29] and [28].

Table 2.1: ADR payload sensors employed for the proximity operations.

Sensor	$r_{\max}$ [km]
VIS NFOV	50
VIS WFOV	10
Flash LiDAR	1
IR camera	3

2.3 Dynamical Model

In this section the dynamical model used in the study is explained. First the environmental model is described with particular focus on the ideal solar-sail model and finally the equations (EoM) of motion are explained.

2.3.1 Environmental model

To focus on the primary dynamics of the sailcraft, a simplified environmental model is adopted that intentionally excludes the complexity introduced by additional perturbing forces such as gravitational harmonics, third-body effects, atmospheric drag, and magnetic forces. This allows for a clearer analysis of the sail's response to solar radiation pressure (SRP), which is the dominant non-gravitational perturbation for a solar-sail mission. As described in McInnes [13], solar sails are continuously accelerated by Solar Radiation Pressure (SRP) so that their orbits are quite different from the usual ballistic arcs followed by conventional spacecraft. SRP, which varies inversely with the square of the distance between the spacecraft and the Sun, can be visualized as the momentum transferred to the solar sail by photons. When photons are reflected, they exert a reaction impulse, in addition to the momentum transferred upon incidence on the sail film. The sum of these impulses leads to a force directed normal to the solar sail.

These assumptions, further explained in the following paragraphs, simplify the force model and enables more direct insight into how sail orientation influences trajectory.

Sun position and illumination

What previously stated about photon reflection and reaction impulse is true only if the sun is considered as a point source (at a large distance: > 10 solar radii) and therefore it can be assumed that sunlight reaches Earth parallel. Moreover, the Sun is assumed to be stationary at the location of the autumnal equinox in the inertial frame.

Ideal solar-sail model

To model the sail behaviour the ideal model is widely used in preliminary mission design because it is simpler for an initial analysis. In contrast, more realistic models exist such as the optical model, which accounts for the sail's reflection, absorption, and re-radiation, and the parametric model, which includes the effects of sail shape under load. These models introduce additional complexity into trajectory analysis and optimization, therefore they are discarded and the ideal force model is preferred. The Ideal solar-sail model chosen follows the assumptions present in [18]:

1. The square is a flat, rigid surface;
2. The solar sail is perfectly reflective;
3. The local SRP is constant ($\bar{P}_\odot = 1360\,\mathrm{W/m^2}$);
4. The SRP effect on the spacecraft bus is negligible;

5. The SRP acceleration is applied through the spacecraft's center of mass (CoM);
6. The area-to-mass ratio of the system is constant;

The orientation of the sailcraft is uniquely determined by the normal direction of the sail $\hat{n}$: the force generated by an ideal and perfectly reflecting solar sail is normal to the sail flat surface. To define $\hat{n}$, the sunlight reference frame is introduced 2.1. $\hat{n}$ is defined by two attitude angles: the cone angle α, defined as the angle between the sail normal and the incident radiation $\hat{s}$, δ defined to be the angle between the projection of the sail normal and some reference direction onto a plane normal to $\hat{s}$. Only one side of the sail can be exposed to direct sunlight hence the sail normal has no component towards the sun. This leads to the following constraints: $\alpha \in [-\frac{\pi}{2}, \frac{\pi}{2}]$ and $\delta \in [-\pi, \pi]$. The sail normal expressed in the sunlight frame, $\hat{n}_S$, is then found as:

$$\hat{n}_S = \cos\alpha\,\hat{x}_S + \sin\alpha\sin\delta\,\hat{y}_S + \sin\alpha\cos\delta\,\hat{z}_S \tag{2.6}$$

As can be deducted from the cone and clock angle limitation, unlike conventional propulsion systems, solar sails cannot produce thrust in any arbitrary directions. The direction of the solar radiation pressure (SRP) force is constrained to lie within a hemisphere oriented away from the Sun. This geometric limitation, commonly illustrated as a Solar-Sail Acceleration (SSA) bubble shown in Figure 2.4, has a central role in sailcraft control design [30].

Remembering that $P = \frac{W}{c} \approx 4.56 \times 10^{-6}$ N/m^2 is the solar radiation pressure at 1 AU, where W is the solar flux at distance r, given by $W = W_\odot \left(\frac{R_E}{r}\right)^2$, the sail acceleration can now be formulated as [13]:

$$\mathbf{a} = \frac{2W_\odot}{c\sigma}\left(\frac{R_E}{r}\right)^2 \cos^2\alpha\,\hat{\mathbf{n}}_\mathbf{I} \tag{2.7}$$

where:

- $W_\odot = 1368\,\mathrm{W/m^2}$ is the solar constant;
- c is the speed of light;
- r is the s/c distance;
- R_E is the Sun-Earth distance, one astronomical unit (1 AU);
- $\sigma = \frac{m}{A}$ is the sail loading (mass per unit area);
- α is the cone angle between the sail normal and the Sun direction;
- $\hat{n}_I = \hat{n}_S$ is the unit normal vector of the sail in ECI frame;

This can be reformulated, defining the characteristic acceleration of the sail as:

$$a_c = \frac{2\eta P}{\sigma}, \quad \text{with} \quad \sigma = \frac{m}{A} \tag{2.8}$$

where η is the efficiency parameter accounting for imperfect reflectivity and sail billowing ($\eta \approx 0.85 - 0.9$). In this case given perfect reflectivity assumption $\eta = 1$.

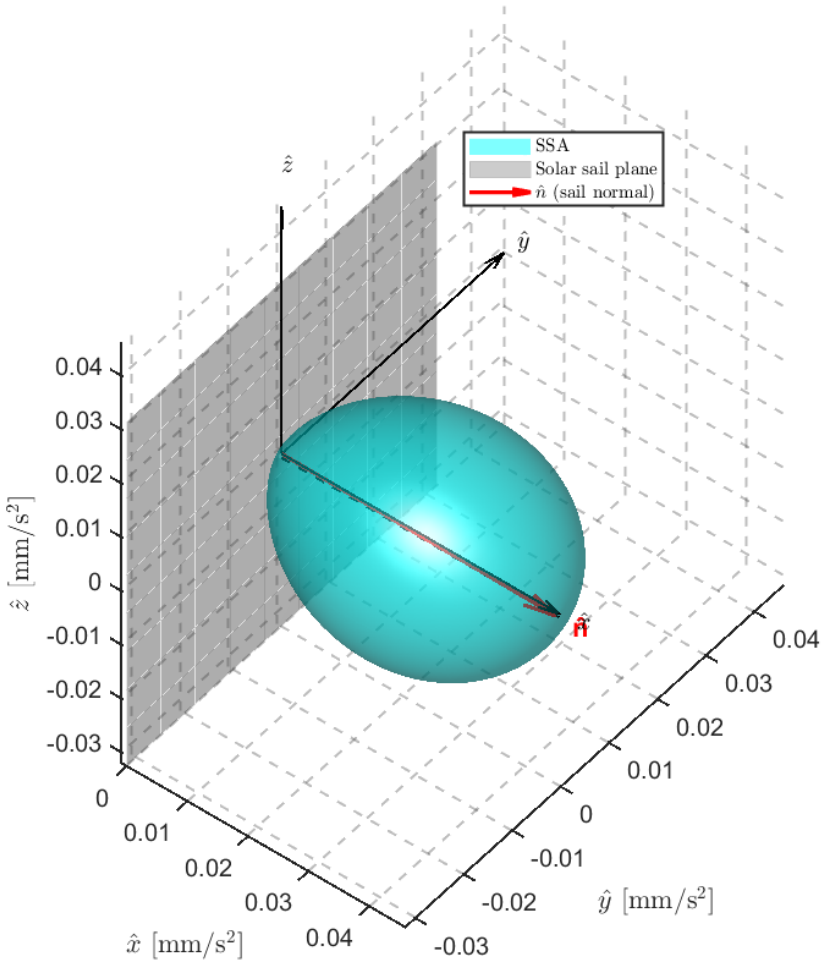

Figure 2.4: Schematic illustrations of the solar-sail normal vector $\hat{n}$ defined by cone angle α (0°) clock angle δ (90°) and the SSA bubble.

The formulation used for acceleration experienced by the sail in this study is then:

$$\mathbf{a} = 2a_c \cos^2 \alpha \, \hat{\mathbf{n}}_\mathbf{I} \tag{2.9}$$

The solar-sail characteristic acceleration can be derived from a sail performance parameter, the dimensionless lightness number β. β is the ratio of the SRP acceleration to the Sun's gravitational acceleration:

$$\beta = \frac{\sigma^*}{\sigma}, \quad a_c = \frac{9.12 \times 10^{-3} \, \beta}{\sigma^*} \quad [\mathrm{m/s^2}], \tag{2.10}$$

with the critical sail loading $\sigma^* \approx 1.53\,\mathrm{g/m^2}$.

Shadow model

To account for eclipse periods when SRP is not active, a simple cylindrical shadow model is employed. This model only makes a distinction between either sunlit (shadow factor η=1) and a shadow phase (shadow factor η=0). Although simplistic, this approach is sufficient for capturing the on/off nature of SRP availability [17, 31].

Three angles are defined using the sail and Sun positions with respect to the Earth: θ which is the angle between sun and satellite position vectors, $\theta_\odot$ which is the angle between the sun position vector and the radial to the point of tangency with the earth of a line from the sun, θ_{sail} which is the angle between the satellite position vector and the radial to the point of tangency with the earth of a line from the satellite. They can be computed as:

$$\begin{aligned} \theta &= \arccos\left(\frac{\vec{r}_\odot \cdot \vec{r}}{r_\odot\, r}\right) \\ \theta_\odot &= \arccos\left(\frac{R_\oplus}{r_\odot}\right) \\ \theta_{\text{sail}} &= \arccos\left(\frac{R_\oplus}{r}\right) \end{aligned} \tag{2.11}$$

With simple geometrical considerations, if $\theta_\odot + \theta_{\text{sail}} < \theta$, the sail is in eclipse condition and thus $\eta = 0$. On the contrary, when $\theta_\odot + \theta_{\text{sail}} \geq \theta$, $\eta = 1$ and the solar radiation pressure acts on the sail. This shadow model, although simplified, provides an efficient representation of eclipse conditions. The transition from sunlight to eclipse is a discontinuous function, which poses difficulties for gradient-based optimization methods (like GPOPS-II) that require differentiable functions. To overcome this a smoothed eclipse model is introduced using a logistic function to represent the eclipse transition:

$$\eta(i) = \frac{1}{1 + \exp\left(-c_s\left(\theta_{\text{tot}} - c_t \cdot \theta\right)\right)} \tag{2.12}$$

Equation 2.12 is the logistic function, θ_{tot} is $=\theta_\odot + \theta_{sail}$, c_s and c_t are, respectively, the sharpness coefficient and the transition coefficient. The parameter c_s determines the slope of the curve at the transition point, while c_t scales the total angle between the apparent solar and body radii and thus effectively shifts the transition point [32]. The choice of these coefficients may be driven by numerical behaviour, model accuracy, or mission-operations considerations.

2.3.2 Equation of motion

The following paragraph is based on [31] and [33]. In a rendezvous manoeuvrer, two orbiting vehicles can be defined: a target (A) and a chaser (B) which actively performs the rendezvous towards the target. In the inertial frame $\mathcal{I}$, the equation of motion (EoM) is governed by Newton's second law of gravitation.

$$\ddot{\mathbf{r}} = -\mu_{\oplus} \frac{\mathbf{r}}{\|\mathbf{r}\|^3} \tag{2.13}$$

where $\mu_{\oplus}$ is the Earth gravitational constant and r is the position vector in the frame I.

In this work, the motion of orbiting objects is referenced to a moving reference systems called LVLH, which is co-moving with the target. In this frame, the non-linear two-body dynamics can be linearized under the assumptions:

- A circular reference orbit for the target,
- Small relative distances between the chaser and the target,
- Negligible perturbations beyond Earth's point-mass gravity and user-defined accelerations (a_x, a_y, a_z).

Leading to a set of linear differential equations known as the *Clohessy-Wiltshire* (CW) or *Hill's* equations. These equations, were first found by G.W. Hill (1838-1914) around 1878 and are known in celestial mechanics as the Hill equations. They were re-discovered in the era of spaceflight for the analysis of rendezvous missions by W.H. Clohessy and R.S. Wiltshire around 1960 , and are therefore also known as the Clohessy-Wiltshire equations.

Let n denote the mean motion of the target, and let (a_x, a_y, a_z) represent additional non-gravitational accelerations acting on the chaser in the directions of the R-bar (x), V-bar (y), and H-bar (z) axes, respectively. The relative motion equations in the LVLH frame are given by:

$$\ddot{x} - 2n\dot{y} - 3n^2 x = a_x \tag{2.14}$$

$$\ddot{y} + 2n\dot{x} = a_y \tag{2.15}$$

$$\ddot{z} + n^2 z = a_z \tag{2.16}$$

The acceleration components (a_x, a_y, a_z) in the simulation's frame (co-moving frame) correspond solely to SRP-induced acceleration.

A key advantage of the CW equations is that they admit closed-form analytical solutions for both position and velocity components of the chaser relative to the target. This analytical nature provides significant computational efficiency and is especially useful in preliminary mission analysis and optimization.

$$x = x_0\,(4 - 3\cos nt) + \frac{\dot{x}_0}{n}\,\sin nt + \frac{2\dot{y}_0}{n}\,(1 - \cos nt) \tag{2.17a}$$
$$+ \frac{f_x}{n^2}\,(1 - \cos nt) + \frac{2f_y}{n^2}\,(nt - \sin nt)$$

$$y = y_0 - \frac{\dot{y}_0}{n}\,(3nt - 4\sin nt) - 6\,x_0\,(nt - \sin nt) \tag{2.17b}$$
$$- \frac{\dot{x}_0}{n}\,(1 - \cos nt) - \frac{2f_x}{n^2}\,(nt - \sin nt) + \frac{2f_y}{n^2}\Big(2 - \tfrac{3}{4}n^2t^2 - 2\cos nt\Big)$$

$$z = z_0 \cos nt + \frac{\dot{z}_0}{n}\,\sin nt + \frac{f_z}{n^2}\,(1 - \cos nt) \tag{2.17c}$$

$$\dot{x} = 3x_0 n\,\sin nt + \dot{x}_0\,\cos nt + 2\dot{y}_0\,\sin nt \tag{2.17d}$$
$$+ \frac{f_x}{n}\,\sin nt + 2\frac{f_y}{n}\,(1 - \cos nt)$$

$$\dot{y} = -\,\dot{y}_0\,(3 - 4\cos nt) - 6x_0 n\,(1 - \cos nt) - 2\dot{x}_0\,\sin nt \tag{2.17e}$$
$$- \frac{2f_x}{n}\,(1 - \cos nt) - 2\frac{f_y}{n}\Big(\tfrac{3}{2}\,nt - 2\sin nt\Big)$$

$$\dot{z} = -\,z_0 n\,\sin nt + \dot{z}_0\,\cos nt + \frac{f_z}{n}\,\sin nt \tag{2.17f}$$

where the additional force f is solely the SRP force.

It is important to underline that the CW model is an approximation. Despite its limitations, the CW model remains widely used in proximity operations due to its simplicity and accuracy within its domain of validity.

Safe relative motions

This section has as reference [34], [35] and [36]. The analytical solution of the CW equations can be used to design safe relative trajectories for spacecraft. These relative motions are natural motions and exploit the geometry of orbits to inspect and circumnavigate the target. The Hill-Clohessy-Wiltshire equations can be rewritten in a more intuitive form to better highlight the key parameters governing natural relative motions:

$$x(\chi) = x_{\max} \cdot \sin(\chi) - \frac{2\dot{y}_c}{3n} \tag{2.18}$$

$$y(\chi) = 2x_{\max} \cdot \cos(\chi) + \dot{y}_c \cdot \left(\frac{\chi - \pi/2}{n}\right) + y_c \tag{2.19}$$

$$z(\theta) = z_{\max} \cdot \sin(\theta) \tag{2.20}$$

$$v_x(\chi) = x_{\max} \cdot n \cdot \cos(\chi) \tag{2.21}$$

$$v_y(\chi) = -2x_{\max} \cdot n \cdot \sin(\chi) + \dot{y}_c \tag{2.22}$$

$$v_z(\theta) = z_{\max} \cdot n \cdot \sin(\theta) \tag{2.23}$$

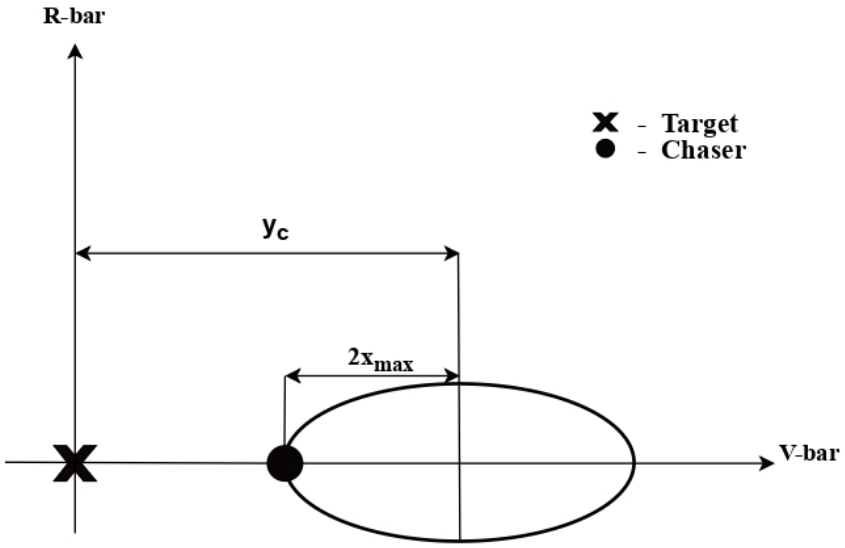

Figure 2.5: In-plane relative spacecraft motion in Hill's frame [35]

This equations can be used to obtain the initial state ($t = 0$) of the spacecraft if the following initial parameters are known:

- x_{max} maximum radial offset.
- z_{max} maximum cross-track offset.
- y_c initial along V-bar (or in-track) separation (Fig. 2.5).
- χ initial in-plane phase angle (Fig. 2.6).
- θ initial cross-track phase angle (Fig. 2.6).
- n mean motion of the target $[rad/s]$.

Varying these parameters two main configurations can be obtained, which are presented in the following sections.

Safety Ellipse concept A widely adopted strategy for safe observation and hold operations is the use of a *safety ellipse* (SE) , which defines an out-of-plane, elliptical periodic relative motion around the target. The ellipse is designed such that:

- The trajectory does not intersect the target's velocity vector (along V-bar direction).
- The orbital period of the chaser's relative motion matches that of the target, resulting in no net drift in the along-track direction: this is referred to as the *period matching condition*. To avoid secular growth of the spacecraft relative range the secular term

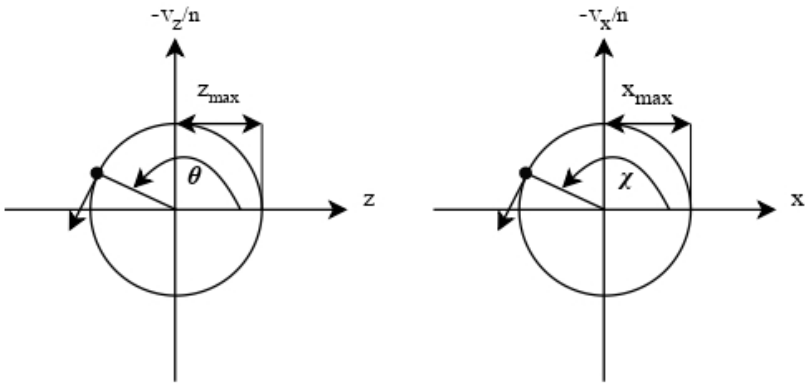

Figure 2.6: Variables describing relative in-plane and out-of-plane phase [35].

in eq. (2.17b), $-\left(6nx_0 + 3y_0\right)t$, is removed by enforcing the following constraint on the radial position and V-bar velocity:

$$\dot{y}_0 = -2x_0 n \tag{2.24}$$

Rewriting (2.18) - (2.23), and imposing $\dot{y}_c$=0, leads the following simplification:

$$x(\chi) = x_{\max} \cdot \sin(\chi) - \frac{2\dot{y}_c}{3n} \tag{2.25}$$
$$y(\chi) = 2x_{\max} \cdot \cos(\chi) + y_c \tag{2.26}$$
$$z(\theta) = z_{\max} \cdot \sin(\theta) \tag{2.27}$$
$$v_x(\chi) = x_{\max} \cdot n \cdot \cos(\chi) \tag{2.28}$$
$$v_y(\chi) = -2x_{\max} \cdot n \cdot \sin(\chi) + \dot{y}_c \tag{2.29}$$
$$v_z(\theta) = z_{\max} \cdot n \cdot \sin(\theta) \tag{2.30}$$

It can be relevant to observe that the centre of the safety ellipse can be offset with the term y_c from the target's centre of mass along the in-track direction.

Walking Safety Ellipse concept An extension of the safety ellipse is the *Walking Safety Ellipse* (WSE), which introduces controlled drift along the V-bar direction. It allows for continuous circumnavigation of the target, while maintaining a predefined safe distance, enabling observation and a safe approach of the target in close-proximity operations. This trajectory is obtained when $\dot{y}_c \neq 0$, so the period matching constraint is no longer met.

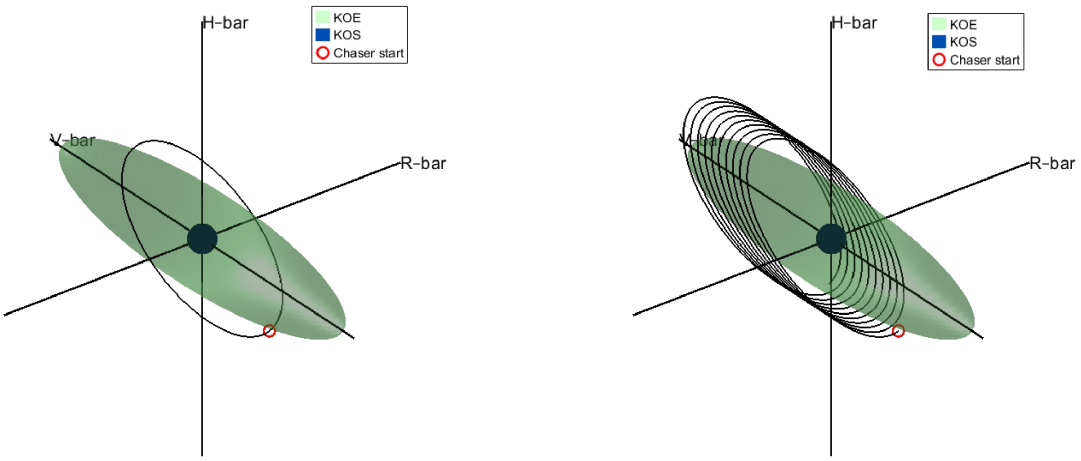

(a) Safety Ellipse **(b)** Walking Safety Ellipse

Figure 2.7: (a) Safety Ellipse. (b) Walking Safety Ellipse.

2.4 Trajectory optimization using Direct Collocation Methods — GPOPS-II

This section will first expand on the main optimization solution methods with references [37],[38] and [39]. Secondly will focus on direct collocation methods using GPOPS-II, which is a commercial optimization software used in this work [40], [41].

2.4.1 Optimization solution methods

The optimization of low-thrust trajectories for solar-sail proximity operations has been extensively studied and approached through various methods, each with distinct advantages and limitations. The trajectory optimization problem is commonly formulated as an optimal control problem (OCP), characterized by non-linear dynamics, multiple constraints, and often multiple objectives. The principal solution approaches can be grouped into the following categories:

1. **Indirect Methods:** These rely on Pontryagin's Maximum Principle (PMP), translating the OCP into a multipoint boundary value problem (MPBVP). Though they offer high precision and insight into the problem structure, they are sensitive to initial guesses and challenging to implement due to the need for solving co-state functions.

2. **Direct Methods:** Widely used for their robustness and flexibility, direct methods discretize the OCP into a non-linear programming problem (NLP) using transcription techniques such as single or multiple shooting and collocation. They are especially

suitable for problems with complex constraints, which can be directly enforced in the dynamics.

3. **Dynamic Programming (DP):** DP techniques, including Differential Dynamic Programming (DDP), solve the Hamilton-Jacobi-Bellman equation to derive optimal feedback control policies. These methods are well-suited for large-scale problems but may suffer from the curse of dimensionality.

4. **Heuristic and Metaheuristic Algorithms:** These global optimization techniques do not require initial guesses and are effective for exploring large solution spaces. Key examples include:

   - *Genetic Algorithms (GA):* Suitable for generating diverse initial solutions; however, they may struggle with constraint enforcement.
   - *Particle Swarm Optimization (PSO):* Inspired by swarm behaviour, these algorithms iteratively refine solutions based on local and global best positions.
   - *Neuroevolution (NE):* Combines neural networks with evolutionary strategies to learn control policies directly, as in the InTrance approach.

5. **Convex Programming:** An increasingly popular method in real-time and autonomous applications. These techniques transform the original problem into a convex form via linearization and convex relaxation.

6. **Hybrid Approaches:** To balance global search and precision, hybrid methods integrate gradient-based techniques with heuristic algorithms. This dual-layer optimization provides both robustness and accuracy, particularly valuable in complex, constrained environments.

Trade-off Considerations: Each method presents a trade-off between accuracy, robustness, and computational efficiency 2.8. For proximity operations, direct collocation, convex programming, and evolutionary algorithms are particularly suitable. Direct methods offer structured flexibility, while evolutionary algorithms provide adaptability in the absence of reliable initial guesses and convex approaches guarantee convergence and efficiency and do not require initial guess, however the convexification of non-convex constraint is often challenging.

2.4.2 Direct collocation methods

Direct collocation methods are robust, flexible, and easy to initialize, variables have a clear physical meaning, and complex control or state constraints are easily handled [39]. This method belongs to the family of direct methods, where the continuous optimal control problem is transcribed into a finite-dimensional non-linear programming (NLP) problem.

In direct collocation, both the state and control trajectories are approximated using piecewise continuous polynomials over discrete segments of the time domain. The key idea

		Flexibility	Robustness	Optimality
Numerical Approaches	Indirect	low	low	high
	Direct	high	high	low
	Dynamic Programming	low	high	high
Numerical solutions	Deterministic	low	high	high
	Heuristic	high	low	low
	Hybrid	medium	medium	medium

Figure 2.8: Trade-off main numerical approaches and numerical solution methods[39]

is to impose the dynamic constraints not continuously, but at a finite set of strategically chosen intermediate points, within each segment, known as *collocation points*.

These collocation points are where the differential equations describing the system's dynamics must be satisfied. Instead of solving the system dynamics through time-marching integration (as in shooting methods), the system dynamics are enforced algebraically by requiring that the derivative of the interpolating polynomial at each collocation point matches the dynamics function:

$$\dot{x}(\tau_j) = f(x(\tau_j), u(\tau_j), \tau_j) \quad \text{for all collocation points } \tau_j \tag{2.31}$$

where

- x(τ_j): state vector at collocation point τ_j.
- $\dot{x}(\tau_j)$ time derivative of the state at τ_j.
- u(τ_j) control at collocation point τ_j.

This approach provides several advantages:

- **Accuracy:** The use of higher-order polynomials allows for accurate trajectory representation even over relatively coarse time grids.
- **Efficiency:** The NLP formulation enables the use of efficient sparse optimization solvers.
- **Flexibility:** Constraints such as bounds on state and control, path constraints, and terminal conditions can be easily incorporated.
- **Robustness:** Compared to indirect methods, direct collocation is less sensitive to initial guesses and can handle complex, constrained problems more reliably.

Because the conditions for dynamic feasibility are only enforced at collocation points, rather than across the entire continuous trajectory, the solution obtained is an approximation. However, with a sufficient number of collocation points and appropriate polynomial degree, the resulting trajectory can achieve a high level of fidelity while maintaining

computational manageability. Direct collocation is widely used in aerospace trajectory optimization and is chosen in this work. It has been implemented in several state-of-the-art software tools such as GPOPS-II.

2.4.3 GPOPS-II

General Purpose Optimal Control Software (GPOPS-II) is an advanced general purpose solver, gradient-based, specifically designed to solve continuous-time optimal control problems (OCPs). It employs an **adaptive orthogonal collocation method** based on *Legendre-Gauss-Radau* (LGR) collocation points, combined with sparse non-linear programming techniques.

Collocation method GPOPS-II uses an **hp-adaptive Gaussian quadrature collocation** approach. The time domain of each phase is divided into mesh intervals, and within each interval, the state and control variables are approximated using polynomials whose degrees can vary across intervals (ph-adaptation), and the length of each interval can also change (hp-adaptation). The collocation points are chosen as the nodes of the LGR quadrature.

Problem transcription The continuous-time OCP is transcribed into a finite-dimensional non-linear programming problem (NLP). This is achieved by enforcing the system dynamics and path constraints at the LGR collocation points, effectively discretizing the control and state trajectories. The transcription leverages polynomial interpolation and Gaussian quadrature integration to approximate the cost functional and defect constraints.

Mesh refinement and error estimation A distinctive feature of GPOPS-II is its **automated mesh refinement algorithm**, as it employs hybrid methods (hp-methods and ph-methods). The solver evaluates the local discretization error based on the collocation defect and determines whether the solution satisfies a user-defined error tolerance. If not, the mesh is refined - by either increasing the polynomial order (ph-refinement), subdividing the time intervals (hp-refinement), or both - and the solution process is repeated using the previously obtained solution as an initial guess.

Solver integration GPOPS-II interfaces with state-of-the-art NLP solvers such as SNOPT and IPOPT. These solvers efficiently handle the large, sparse constraint Jacobians that arise from collocation-based transcriptions, ensuring fast convergence even in complex multi-phase OCPs.

Scaling and derivatives As stated in [42], to ensure convergence of direct collocation methods the NLP problem should be properly scaled, so that variables are close to unity; GPOPS-II then scales the constraints and objectives based on the scaling parameters.GPOPS-II offers multiple automatic scaling strategies (e.g., `automatic-bounds`, `automatic-guess update`) to improve problem conditioning. However in this work a

user-defined scaling is used because using automatic scaling the problem is struggling to converge. Derivatives can be provided via sparse finite-differencing method, by providing user-supplied (analytic) derivatives or automatic differentiation using ADiGator.

Algorithmic flow The computational procedure in GPOPS-II consists of:

1. **Input Setup:** User defines the structure and components of the OCP.
2. **Preprocessing:** Dependency and scaling analysis are performed.
3. **Transcription:** The OCP is converted into an NLP using the current mesh.
4. **Error Estimation and Refinement:** Mesh is adapted if error tolerances are not met.
5. **Solution Output:** The final optimal solution and mesh history are returned.

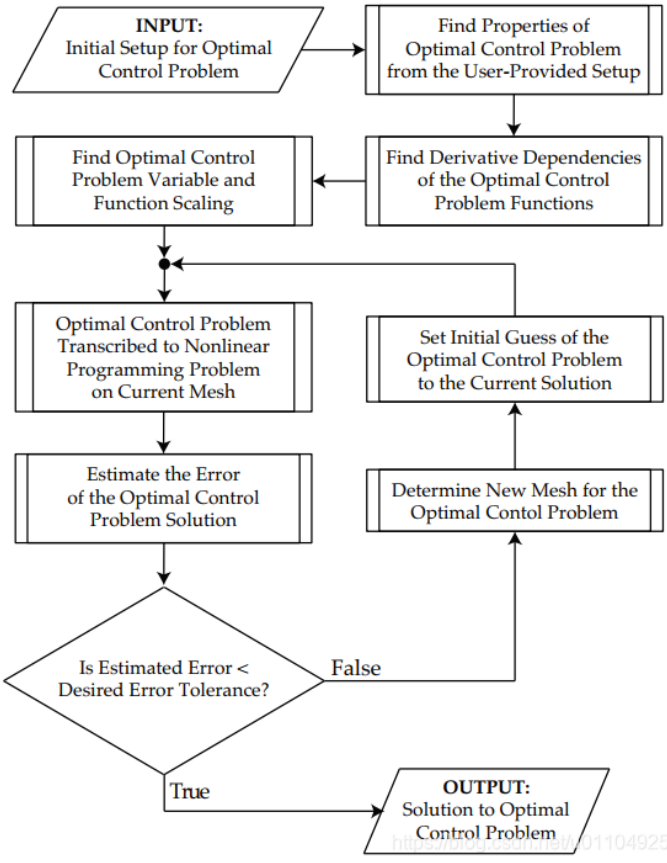

Figure 2.9: Flowchart of the GPOPS - II algorithm [40]

2.5 Simulation and Optimization Setup

2.5.1 GPOPS-II setup

Users must define the OCP using a structured input in MATLAB, including the following functions:

- **Continuous function:** Describes the system dynamics in any phase of the problem, the integrands that are required to compute any integrals and the path constraints in any phase of the problem.

- **Endpoint function:** Specifies the cost to be minimized and how the start and/or end in any of the phases, the integrals in any phase of the problem and the static parameters are related to one another.

- **Bounds and guesses:** Include initial and final states, control limits, and initial guesses.

Next the user must specify the lower and the upper limits on:

- the time at the start and end of a phase.

- the state at the start of a phase, during a phase, and at the end of a phase.

- the control during a phase.

- the path constraints.

- the event constraints.

- the static parameters.

In Table 2.2 a summary of the setting of the optimizer is shown. Values for each parameters are found by trial and error and by comparison with solved optimization problems with the example provided in the GPOPS-II software and partially illustrated in [40]. In Appendix B.1 a sensitivity analysis has been carried to try to find tuning criteria for the collocation point number, the number of mesh intervals and mesh tolerance.

GPOPS-II setup	User Input
Mesh method	'hp-LiuRao-Legendre'
Mesh tolerance	10^{-5}
Mesh maximum iterations	10
Mesh maximum collocation points	20
Mesh mimimum collocation points	10
Mesh collocation point per phase	10
Number of mesh intervals	100
NLP solver	'ipopt'
IPOPT linear solver	'ma57'
IPOPT tolerance	10^{-7}
IPOPT maximum iterations	2000
Derivative supplier	'Foward differences'
Derivative level	'second'
Derivative dependencies	'sparseFD'
Method	'Differentiation'

Table 2.2: General overview of the GPOPS-II settings to solve the optimal control problem.

2.5.2 Close-Proximity scenario definition and optimization

In this section the close-proximity scenario is characterized. First the design parameters (sail and target parameters) are defined and then main optimization problems covered in this study are formulated.

Design parameters

Regarding the target (i.e., the debris), its initial state at $t = 0$ s is assumed to be on a circular orbit at 1000 km altitude, with zero eccentricity ($e = 0°$) and zero inclination ($i = 0°$), resulting in an equatorial orbit. The simulation begins when the target is located at the vernal equinox, at a true anomaly of $\nu = 0°$ and a right ascension of the ascending node (RAAN) of 0°. At this position the target is initially fully eclipsed by Earth. As for the chaser (i.e., the solar sail), it is considered to be in relative motion around the target, since in close-proximity conditions and it is assumed that the sail has already reached the orbital plane of the target. To conduct the study with a lightness number achievable by current state-of-art technology, the lightness number of the ACS3 [15] mission is chosen. Unless otherwise specified, the sail parameters adopted in this study correspond to a lightness number of $\beta = 7.7 \times 10^{-3}$, yielding a characteristic acceleration of $a_c = 4.6 \times 10^{-5}$ m/s^2. The control angles are constrained such that the cone angle $\alpha \in [-\pi/2, \pi/2]$ and

the clock angle $\delta \in [-\pi, \pi]$.

All simulation are carried out propagating the CW equations with an initial step size of $dt = 10$ s, see Appendix for further details on this choice A.1.3.

Optimization problem formulation

Two types of close-proximity trajectories are explored: inclined Hold Trajectories (addressed in this thesis also as SE) and Inspection Loop Trajectories (addressed in this thesis also as WSE). Lastly a Transfer is found from a hold trajectory located behind the target and outside the outer KOE volume to the Inspection Loop.

Each problem has different objectives and constraints, necessitating of different formulations. The results of these optimization problems are discussed in Chapter 3, while more details on the optimization can be found in Appendix B.2 .

Hold Trajectory optimization

The optimal control problem is maximizing the time the Hold Trajectory (SE) stays within the KOZs. Maximizing the time t_f is mathematically equivalent to minimizing $-t_f$. t_f is bounded between 0 and a maximum of $t_{f_{\max}}$. The problem is formulated to include geometric path constraints that require the sail to remain outside a safety sphere of radius R_s (the KOS constraint) while remaining inside a ellipsoid defined by the semi-axes (a, b, c) (KOE constraint). The dynamics of the system uses the Clohessy-Wiltshire equations with the sail normal vector as control $\vec{u}(t)$. Sail normal vector and so thrusting is constrained so that the normal is never directed towards the sun.

In this section, we present a general formulation of the problem, with $\alpha \in \left[-\frac{\pi}{2}, \frac{\pi}{2}\right]$ and $\delta \in [-\pi, \pi]$. However, in this study further constraints are imposed on the cone angle; see Section 3.1 and Appendix B.3 for the numerical values used.

Having defined the following variables:

- $x(t) = [x, y, z, \dot{x}, \dot{y}, \dot{z}]^T$: state vector (position and velocity).
- $u(t) = [a_x, a_y, a_z]^T$: control acceleration vector (non-gravitational).
- a_x, a_y, a_z: non-gravitational accelerations along the x, y, and z axes.
- n: orbital mean motion.
- $v_{i,f}^{\min}$, $v_{i,f}^{\max}$: minimum and maximum allowable terminal velocity along axis $i \in \{x, y, z\}$.

The general Hold Trajectory problem formulation is the following:

$$\min_{x(t),\,u(t)} \quad -t_f$$

subject to:

$$\begin{cases} \ddot{x} - 2n\dot{y} - 3n^2 x = a_x \\ \ddot{y} + 2n\dot{x} = a_y \\ \ddot{z} + n^2 z = a_z \end{cases} \qquad \text{(State dynamics)}$$

$$x_{0,\text{lower}} = [-a,\ -b,\ -c,\ -v_{x,f}^{\min},\ -v_{y,f}^{\min},\ -v_{z,f}^{\min}] \qquad \text{(State initial condition)}$$

$$x_{0,\text{upper}} = [a,\ 0,\ c,\ v_{x,f}^{\max},\ v_{y,f}^{\max},\ v_{z,f}^{\max}]$$

$$x_{\text{lower}} = [-a,\ -b,\ -c,\ -v_{x,f}^{\min},\ -v_{y,f}^{\min},\ -v_{z,f}^{\min}] \qquad \text{(State bounds)}$$

$$x_{\text{upper}} = [a,\ b,\ c,\ -v_{x,f}^{\max},\ -v_{y,f}^{\max},\ -v_{z,f}^{\max}]$$

$$x_{t_f,\text{lower}} = x_{\text{lower}} \qquad \text{(State final condition)}$$

$$x_{t_f,\text{upper}} = x_{\text{upper}}$$

$$x^2 + y^2 + z^2 \geq R_s^2 \qquad \text{(KOS path constraint)}$$

$$\left(\frac{x}{a}\right)^2 + \left(\frac{y}{b}\right)^2 + \left(\frac{z}{c}\right)^2 \leq 1 \qquad \text{(KOE path constraint)}$$

$$\|\vec{u}(t)\| \in [0, 1] \qquad \text{(Control path constraint)}$$

$$[0,\ -1,\ -1]^T \leq \vec{u}(t) \leq [1,\ 1,\ 1]^T \qquad \text{(Control bounds)}$$

$$t_f \in [t_0,\, t_{f_{\max}}] \qquad \text{(Time bounds)}$$

Inspection Loop

This is the optimization setup for the Inspection Loop (IL) problem, a tubular motion around the target, which maintain the spacecraft near the observation zone for as long as possible, allowing drifting along the V-bar and thereby ensuring view of the target from a broad range of angles. The primary objective is to observe the target for a minimum and a maximum of observation time t_{obs}, maximizing the time spent outside the KOE satisfying state, control, time and integral bounds and eventgroup and path constraints.

For what concern eventgroup constraints they are used to constrain the final position on a certain state, which is a target point on the Hold Trajectory (SE). A small tolerance is set on the position, tol, and the velocity, tol_v, and lowered throughout the optimization so that the final state of the IL is as close as possible to the target point on the Hold trajectory . The logic followed is explained in the flowchart 2.10a.

The final time of flight (ToF) is fixed and set to a value greater than the maximum observation duration. This guarantees that the spacecraft can both maximize its observation window outside the keep-out ellipsoid (KOE) and then reach the target point inside the ellipsoid. If t_f were set equal to or below $t_{\text{obs,max}}$, the sail would be forced to shorten its loiter time outside the KOE to satisfy the transfer requirement. By decoupling t_f from $t_{\text{obs,max}}$, the initial portion of the trajectory is allocated to maximizing the actual observation time t_{obs} within its prescribed bounds, and then the remaining interval is used to intercept the target point inside the ellipsoid.

Compared to the Hold Trajectory case, the KOE constraint is relaxed from ≤ 1 to ≤ 4. This additional margin allows the optimizer to maintain the trajectory just outside the ellipsoid,

maximizing observation opportunities while keeping it close to the target region.

The objective function is formulated as a weighted sum of two objectives: maximizing the total duration of the trajectory and encouraging the system to spend more time outside a predefined ellipsoidal region. Specifically, the time outside the KOE is slightly favoured and the integral is formulated with a smoothed function that reflects whether the state lies outside the ellipsoid.

To achieve differentiability in GPOPS-II, indeed, the binary indicator function is replaced with a smooth function defined by a hyperbolic tangent as in [43]:

$$\phi(x, y, z) = \frac{1}{2}\left(1 + \tanh\left(\frac{\left(\frac{x}{a}\right)^2 + \left(\frac{y}{b}\right)^2 + \left(\frac{z}{c}\right)^2 - 1}{\rho}\right)\right) \tag{2.32}$$

Here, ρ is a smoothing parameter that controls the sharpness of the transition from inside to outside the ellipsoid. A smaller value of ρ produces a steeper approximation, approaching the original indicator function. In our implementation, $\rho = 0.3$ is selected, following the approach discussed in [43] and for empirical attempts made with the problem in question.

The overall cost function is thus expressed as:

$$\min_{u(t)} \; -w_1 t_f - w_2 \int_{t_{\text{obs}}}^{t_f} \phi(x(t), y(t), z(t))\, dt \tag{2.33}$$

A weighted sum approach is adopted [44], where w_1 and w_2 are scalar weights used to balance the contribution of each term. This formulation allows to explore different trade-off between maximizing ToF and the time spent outside the ellipsoid. Prior to summing them up, each of the two variables is normalised with respect to its own reference interval (e.g. for time of flight we use $t_f/t_{f,\max}$). In this way, each term is dimensionless and comparable. The specific values of the weights chosen are discussed in section 3.2, and the numerical values used in the optimization setup can be found in section B.4. In Section 2.5.2 the Inspection Loop (IL) optimization problem is formulated as follows:

$$\min_{x(t),\,u(t)} \; -w_1\, t_f - w_2 \int_{t_{\text{obs}}}^{t_{\max,\text{obs}}} \phi(x(t), y(t), z(t))\, dt$$

$$\text{where} \;\; \phi(x,y,z) = \tfrac{1}{2}\Big(1 + \tanh\Big(\tfrac{(\frac{x}{a})^2 + (\frac{y}{b})^2 + (\frac{z}{c})^2 - 1}{\rho}\Big)\Big)$$

$$\begin{cases} \ddot{x} - 2n\dot{y} - 3n^2 x = a_x, \\ \ddot{y} + 2n\dot{x} = a_y, \\ \ddot{z} + n^2 z = a_z, \end{cases} \qquad \text{(State dynamics)}$$

$$x_{0,\text{lower}} = [\, x_{\min},\, y_{\min},\, z_{\min},\, -v_{x,f}^{\min},\, -v_{y,f}^{\min},\, -v_{z,f}^{\min} \,] \qquad \text{(State initial condition)}$$

$$x_{0,\text{upper}} = [\, x_{\max},\, 0,\, z_{\max},\, v_{x,f}^{\max},\, v_{y,f}^{\max},\, v_{z,f}^{\max} \,]$$

$$x_{\text{lower}} = [\, x_{\min},\, y_{\min},\, z_{\min},\, -v_{x,f}^{\min},\, -v_{y,f}^{\min},\, -v_{z,f}^{\min} \,] \qquad \text{(State bounds)}$$

$$x_{\text{upper}} = [\, x_{\max},\, y_{\max},\, z_{\max},\, -v_{x,f}^{\max},\, -v_{y,f}^{\max},\, -v_{z,f}^{\max} \,]$$

$$x_{t_f,\text{lower}} = x_{\text{lower}} \qquad \text{(State final condition)}$$

$$x_{t_f,\text{upper}} = x_{\text{upper}}$$

$$t_{\text{obs}} \le \int_{t_0}^{t_f} \mathbb{I}_{\text{outside}}\, dt \le t_{\max,\text{obs}} \qquad \text{(Integral constraint)}$$

$$\|r(t_f) - r_{\text{target}}\| \le [tol, tol, tol] \qquad \text{(Eventgroup on position)}$$

$$\|v(t_f) - v_{\text{target}}\| \le [tol_v, tol_v, tol_v] \qquad \text{(Eventgroup on velocity)}$$

$$x^2 + y^2 + z^2 \ge R_s^2 \qquad \text{(KOS)}$$

$$\left(\tfrac{x}{a}\right)^2 + \left(\tfrac{y}{b}\right)^2 + \left(\tfrac{z}{c}\right)^2 \le 4 \qquad \text{(KOE)}$$

$$\|u(t)\| \in [0,1] \qquad \text{(Control path constraint)}$$

$$[0,-1,-1]^T \le u(t) \le [1,1,1]^T \qquad \text{(Control bounds)}$$

$$t_f \in [\, t_{\max,\text{obs}},\, t_{f_{\max}} \,] \qquad \text{(Time bounds)}$$

Transfer

This optimization setup defines the Transfer trajectory from a starting point on the Hold trajectory, positioned outside the KOE behind the target, to a designated interception point on the Inspection Loop (IL) trajectory. The quantities $x_f,\ v_f$ denote the spacecraft's final state (position and velocity) at the end of the transfer, whereas $x_t,\ v_t$ represent the target state on the IL trajectory. The objective is to minimize the mismatch between these two states. Defining:

$$\Delta\mathbf{x} = \mathbf{x}_f - \mathbf{x}_t, \qquad \Delta\mathbf{v} = \mathbf{v}_f - \mathbf{v}_t,$$

the objective function is written as a weighted combination of the relative errors of position and velocity:

$$J \;=\; w_r \,\frac{\|\Delta\mathbf{x}\|^2}{\|\mathbf{x}_t\|^2} \;+\; w_v \,\frac{\|\Delta\mathbf{v}\|^2}{\|\mathbf{v}_t\|^2} \tag{2.34}$$

In addition to the primary optimization objective, a bound constraint is enforced to ensure that the transfer's final state remains within a prescribed tolerance *tol* of the desired target state. The same logic is followed to bound the initial state so that it deviates by a set tolerance *tol*

from the wanted initial state on the SE. Since bounding immediately with tight tolerances the initial state do not allow convergence to an optimal solution, these tolerances are then decreased iteratively in a loop (see flowchart 2.10b) until the minimum feasible tolerances are found.

More details on numerical values used in the corresponding section 3.3 of the transfer results and in Appendix B.5.

The general optimization problem is formulated as follows:

$$\min_{x(t),\,u(t)} \quad J = w_r \frac{\|\Delta \mathbf{x}\|^2}{\|\mathbf{x}_t\|^2} + w_v \frac{\|\Delta \mathbf{v}\|^2}{\|\mathbf{v}_t\|^2}$$

$$\text{subject to:} \quad \begin{cases} \ddot{x} - 2n\dot{y} - 3n^2 x = a_x, \\ \ddot{y} + 2n\dot{x} = a_y, \\ \ddot{z} + n^2 z = a_z, \end{cases} \qquad \text{(State dynamics)}$$

$$x_{\text{lower}} = [\, x_{\min},\, y_{\min},\, z_{\min},\, -v_{x,f}^{\min},\, -v_{y,f}^{\min},\, -v_{z,f}^{\min} \,] \quad \text{(State bounds)}$$

$$x_{\text{upper}} = [\, x_{\max},\, y_{\max},\, z_{\max},\, -v_{x,f}^{\max},\, -v_{y,f}^{\max},\, -v_{z,f}^{\max} \,]$$

$$x_{0,\text{lower}} = \|\mathbf{x}_{\text{SE\_target}}\| - tol \quad \text{(Initial state bound)}$$

$$x_{0,\text{upper}} = \|\mathbf{x}_{\text{SE\_target}}\| + tol$$

$$x_{t_f,\text{lower}} = \|\mathbf{x}_{\text{IL\_target}}\| - tol \quad \text{(Final state bound)}$$

$$x_{t_f,\text{upper}} = \|\mathbf{x}_{\text{IL\_target}}\| + tol$$

$$\left(\frac{x}{a}\right)^2 + \left(\frac{y}{b}\right)^2 + \left(\frac{z}{c}\right)^2 \geq 1 \quad \text{(KOE path constraint)}$$

$$\|\vec{u}(t)\| \in [0,1] \quad \text{(Control path constraint)}$$

$$[0,\, -1,\, -1]^T \leq \vec{u}(t) \leq [1,\, 1,\, 1]^T \quad \text{(Control bounds)}$$

$$t_f \in [t_{f_{\min}},\, t_{f_{\max}}] \quad \text{(Time bounds)}$$

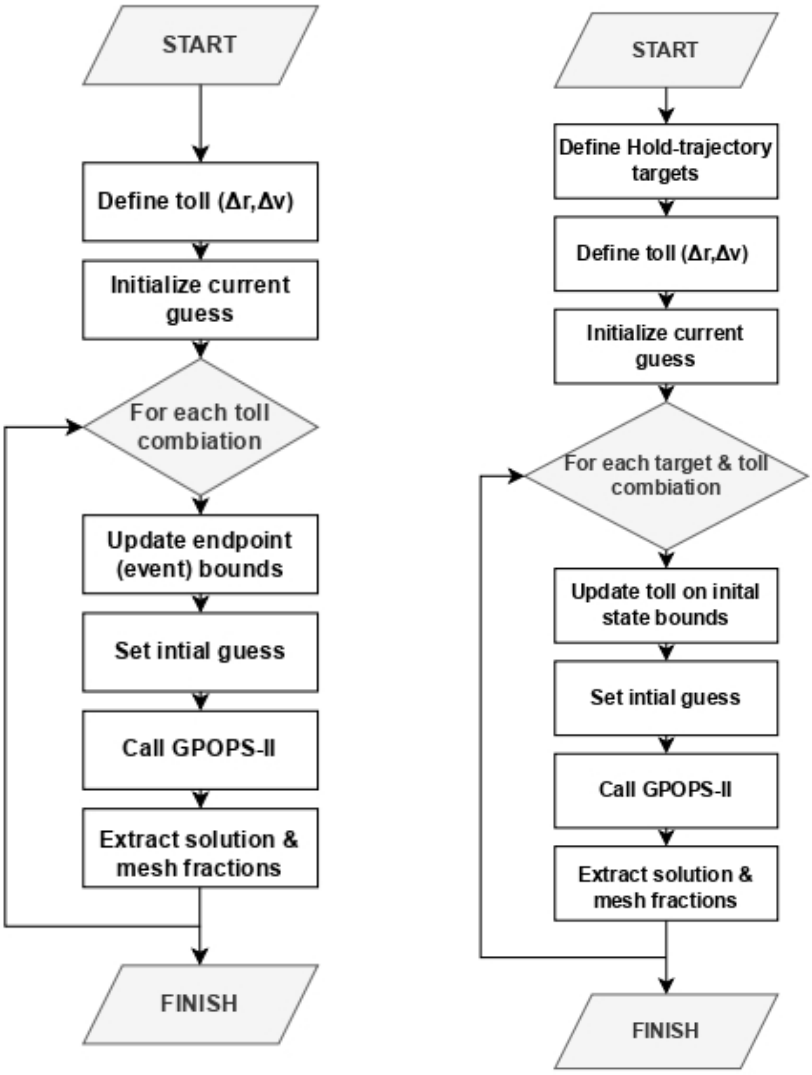

(a) Flowchart IL (WSE) **(b)** Flowchart Transfer

Figure 2.10: Optimization flowcharts.

Chapter 3

Close-Proximity Operations Study

The chapter follows the actual research flow: it begins with the exploration of Hold Trajectories (SE), proceeds to the development of the Inspection Loop, and concludes with the transfer that links with an earlier far-range rendezvous phase, adopting a backward-design approach.

3.1 Hold Trajectory Analysis

In traditional close-proximity and rendezvous operations, hold points serve as time-flexible elements from which the next mission phase is planned and by which the mission is calibrated against external events. However, when a solar sail is employed as the primary propulsion system, its large surface area and the continuous forces from atmospheric drag and solar radiation pressure make conventional hold points infeasible. To address this, Reichel in [20] introduced the concept of planar hold trajectories: paths that allow the sailcraft to remain near the target for extended periods, enabling detailed observations, system checks and preparation for subsequent rendezvous manoeuvres.

In the following section, we extend this idea to inclined hold trajectories, using as reference the concept of Safety-Ellipse natural relative motion. Inclined hold trajectories provide a clear safety advantage: the chaser's velocity vector never intersects that of the target, yielding a target-centred trajectory that significantly reduces collision risk compared to a planar encircling orbit. The scenario considered in the three optimisation problems is described in detail in the Design parameters paragraph of section 2.5.2 and is referred to unless otherwise indicated.

3.1.1 Test case

The chaser spacecraft approaches the target from a distance of several hundred metres in the negative V-bar direction. To define safe approach regions, two nested Keep-Out Zones (KOZs) are introduced: an outer ellipsoidal boundary and an inner spherical exclusion zone. The sailcraft's Hold Trajectory must remain inside the outer ellipsoid and outside the inner sphere, maintaining a stable orbit around the target throughout the proximity operations.

GPOPS-II requires an initial guess for the state and control. The sailcraft is initialized on a Keplerian elliptical orbit with its period matching that of the target orbit. The ellipse is sized

and oriented according to the KOZs definitions and the Safety-Ellipse formulation, ensuring the orbit lies entirely inside the prescribed hold volumes. The initial elliptical orbit is positioned midway between the outer ellipsoid and the inner sphere. The geometric parameters used in the analysis are listed in Table 3.1.

Outer Ellipsoid		Inner Sphere	Safety Ellipse			
Semi-major	Semi-minor	Radius	$x_{\max} = z_{\max}$	Δy	χ	θ
740	160	50	105	0	0°	−90°

Table 3.1: Geometric parameters.

The initial attitude is edge-wise to the Sun (cone angle $\alpha = 90°$ and clock angle δ of 0° constant). The initial state guess used in this analysis is listed in Table 3.2.

α	δ	Initial State vector
90°	0°	$[0; -210; -105; -0.1047; 0; 0]$

Table 3.2: Control settings and initial state vector.

The optimization formulation is detailed in Section 2.5.2 and Appendix B.3, including the objective function, boundary conditions, and path constraints. The simulations final time is set to ten orbital revolutions of the target: approximately 17.5 hours using a initial fixed time step of $dt = 10$ s.

Since a cone angle of 90° results in zero acceleration of the sail, the sail would simply follow its initial Keplerian orbit. However for solar-sail missions typically a constrain on cone angle is considered: for example, the NEA Scout mission limited the cone angle to $\alpha_{\max} = 70°$ [45]. To assess the impact of cone angle restrictions on inclined hold trajectories, six different cone angle constraints are analysed as in Table 3.3.

Table 3.3: Six maximum cone angles $\alpha_{\max}$ considered in the analysis.

$\alpha_{\max}$ [°]					
60	65	70	75	80	85

3.1.2 Cone angle limitations

The safety ellipse is a natural relative motion that, assuming no perturbations and if the sail is oriented edge-wise, does not require any intervention of the propulsion system, making it a perfect safe relative motion of the sailcraft to the target. However, the solar sail follows non-Keplerian orbits since the SRP is constantly acting on the sail and because of sailcraft dynamics, the thrust direction is limited, and that is reflected in cone and cone angle constraints. The objective of the simulation is to maximize the time that the sail remains within the Keep Out Zones (KOZs). It is found that an optimal trajectory can be established, allowing the sail to remain within the volume between the KOZs for the maximum allowable time of 10 target period revolutions when

α_{max} is further constrained. This analysis applies to all six constraints on the maximum cone angle, which are: 85°, 80°, 75°, 70°, 65°, and 60°.

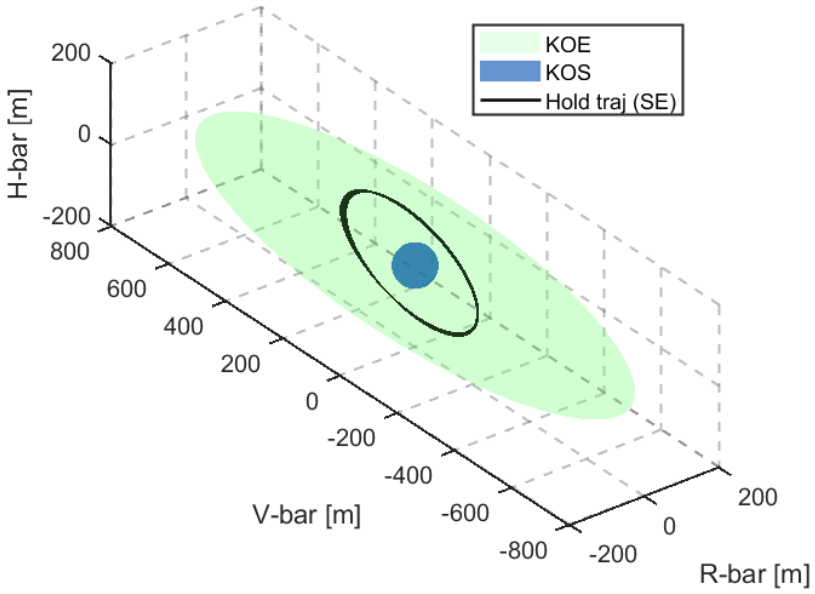

(a) SE trajectory

Figure 3.1: Hold trajectory (SE) with a maximum cone angle of 85°: (a) trajectory.

In Fig. 3.1 it can be seen that with a constrained cone angle of 85° the sailcraft stays within the designated hold volumes. The increase/decrease of the semi-major axis of the chaser orbit is controlled as there is almost no drift along the V-bar direction as show in Fig. 3.2. Indeed the general movement along the V-bar can be explained as a change of the semi-major axis.

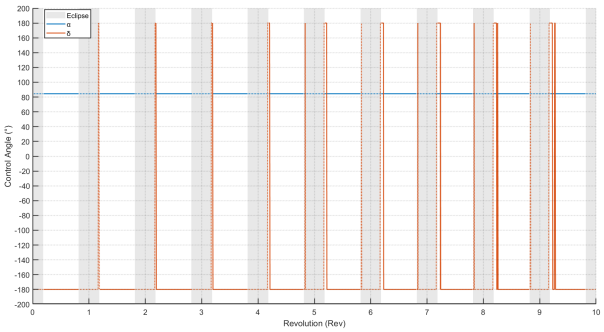

(b) Control inputs

Figure 3.1: (continued) (b) Controls resulting from the optimization (the control line is continuous when the trajectory is not eclipsed).

In the specific cases with $\alpha_{max} = 85°$ and 80° in Fig. 3.3, the optimal control found has the cone angle α immediately to its upper limit for the entire flight time (ToF). During the sunlit portions of the orbit the maximisation of the cone angle is effective because it reduces drift and

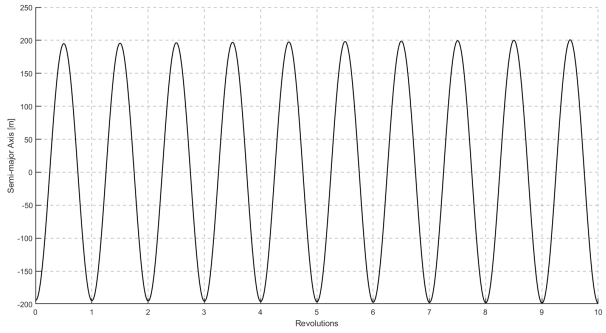

Figure 3.2: Change of semi-major of the optimised trajectory of test case for hold trajectory with α_{max} 85°.

perturbations.

The clock angle δ, while not affecting the thrust magnitude, governs the thrust direction and exhibits frequent switching behaviour in both cases. In both scenarios, δ oscillates between $+180°$ and $-180°$, but not with a perfectly regular periodic behaviour.

In the $\alpha_{\max} = 85°$ case, during the illuminated portion of the first revolution, δ remains at $-180°$. Starting from the second revolution, as the spacecraft exits eclipse, δ begins switching, first jumping to $+180°$ and then immediately back to $-180°$. As the number of revolutions increases, the duration of the control staying at $+180°$ progressively increases, forming an asymmetric pattern in the switching.

In the $\alpha_{\max} = 80°$ case, δ switches to $+180°$ already during the first sunlit segment. However, unlike the 85° case, the portion of time where δ stays at $+180°$ gradually decreases over the course of the revolutions. By the time the spacecraft completes ten revolutions, δ remains almost entirely at $-180°$ during the illuminated arcs. When $\alpha_{\max}$ is reduced to 70°, as shown in Fig. 3.5b, the first period of the control profile indicates that, after re-entering sunlight, α starts slightly below its upper limit and gradually increases as the available thrust grows. In this case, the behaviour of δ differs from the previous control profiles observed: while it still exhibits switching, the pattern becomes more irregular and less clearly periodic compared to higher $\alpha_{\max}$ cases. Any constant control profiles or oscillations during eclipse, when no solar radiation pressure is present, have no impact on the trajectory. These control behaviours during the shadow phases are most likely the result of numerical effects introduced by the discretization and the collocation method used in GPOPS-II.

Regarding the trajectory profile, trajectories with tighter cone angles experience a faster increase or decrease of the semi-major axis along the V-bar directions can be seen in Fig. 3.4.

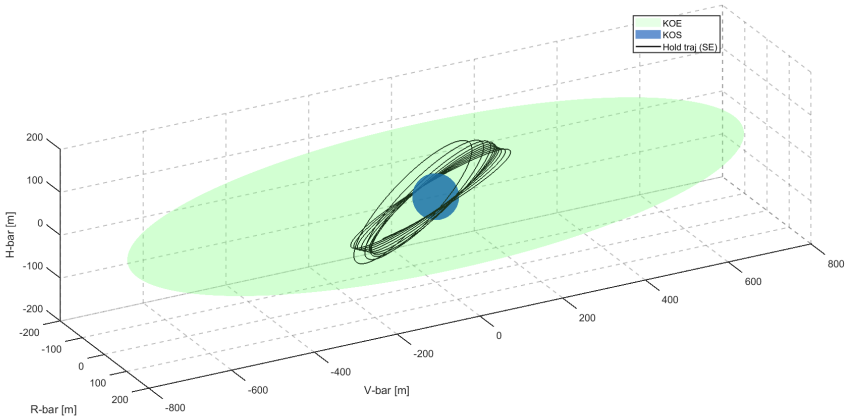

(a) Hold trajectory ($\alpha = 80°$)

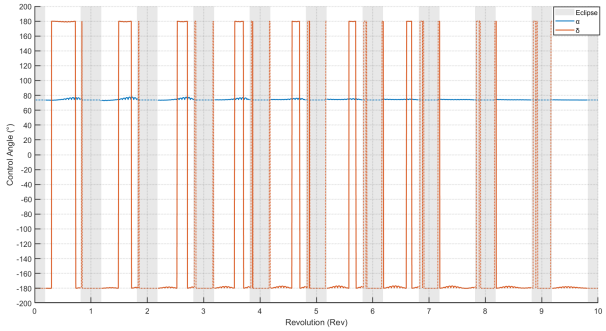

(b) Controls for $\alpha = 80°$

Figure 3.3: Hold trajectories (SE) with maximum cone angles of 80° (a) and first revolution relative interval control(b).

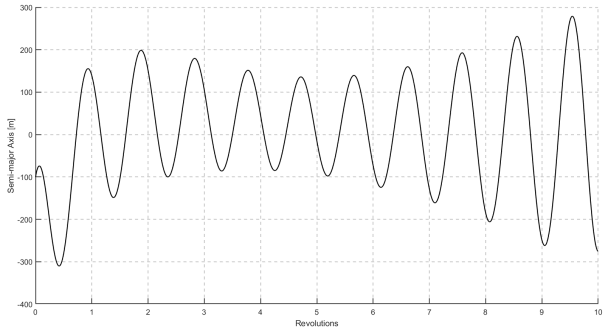

Figure 3.4: Change of semi-major of the optimised trajectory of test case for hold trajectory with α_{max} 70°.

Indeed, it can be seen in Fig. 3.5a that with a maximum α of 70°, the sail no longer exhibits a Safety Ellipse behaviour; a noticeable drift along the V-bar is present.

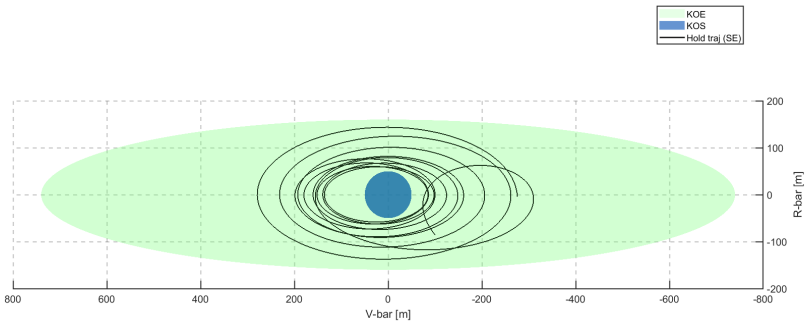

(a) (a) Hold trajectory ($\alpha = 70°$)

Figure 3.5: Hold trajectory (SE) with a maximum cone angle of 70°.

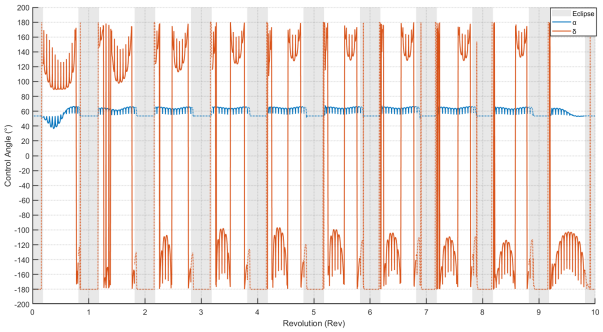

(b) (b) Controls for $\alpha = 70°$

Figure 3.5: (continued) First revolution relative interval control.

3.1.3 Safety assessment

Ensuring mission safety is one of the most important requirements in close-proximity operations in order not to collide with the target. A passive safety orbit design is incorporated in the trajectory optimization, aiming to guarantee that the spacecraft naturally avoids the Keep-Out Zone (KOZ) even in the event of control system failure. Therefore, a safety assessment is performed, two representative points are selected from the first revolution of each optimized trajectory for $\alpha_{\max} = 85°$, $75°$, and $65°$. These points correspond to one-quarter ($T_t/4$) and one-half ($T_t/2$) of the target orbital period, where T_t denotes the period of the target. The associated state vectors and corresponding control inputs (cone and clock angles) are reported in Table 3.4. Each case is forward-propagated for 15 target revolutions (approximately 26 hours), assuming constant attitude — i.e., fixed α and δ values derived from the selected points — simulating a scenario in which the sail becomes stuck in a specific orientation.

Case	x	y	z	$\dot{x}$	$\dot{y}$	$\dot{z}$	α	δ
	−97.3164	−2.2008	−4.8314	−0.0013	0.1942	0.1033	84.4810	−180.0000
$\alpha_{\max} = 85°$	−1.1486	195.0933	103.1693	0.0972	0.0023	0.0042	84.4811	−179.9999
	51.6206	−251.5464	−89.2576	−0.0374	−0.1351	0.0189	59.2469	−176.6665
$\alpha_{\max} = 75°$	−83.5142	−252.3476	17.3832	−0.0785	0.1580	0.0880	62.0138	160.5921
	67.9072	−185.2307	−63.5310	0.0076	−0.1767	0.0557	58.5429	169.0790
$\alpha_{\max} = 65°$	−51.0193	−299.6024	55.2871	−0.1020	0.0911	0.0631	60.8862	136.8569

Table 3.4: State vectors and corresponding controls for the safety assessment. The first row corresponds to the first target state $T_t/2$ and the second row to the second target state $T_t/4$.

In total 6 cases where analysed. Resulting in Fig. 3.6 for the first point at $Tt/4$ state and in Fig. 3.7 for the second target state at $Tt/2$.

The safety assessment shows that if the sailcraft gets stuck in a certain attitude on the Hold Trajectory it will not collide with the target.

For both points selected from the optimized trajectory with $\alpha_{\max} = 85°$, if the sailcraft becomes stuck in a fixed attitude it continues to follow the Hold Trajectory. This is because the optimal control found for the cone angle in this case is almost constant over time.

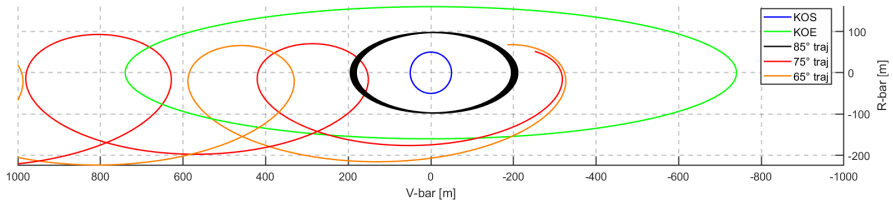

Figure 3.6: Safety assessment Hold trajectory (SE) from target point 1 with maximum α_{max} 85°,75° and 65°.

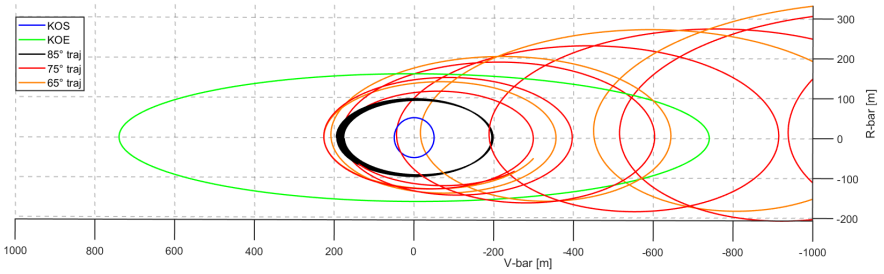

Figure 3.7: Safety assessment Hold trajectory (SE) from target point 2 with maximum α_{max} 85°,75° and 65°.

The more the cone angle is constrained $(75°, 65°)$, the greater the drift in the event of a failure along the V-bar direction. For the first point chosen along the trajectory, the propagation shows motion of the chaser in the positive V-bar direction, and the trajectory never enters the KOS. For the second point chosen, the drift is along the negative V-bar direction. However, since the trajectory is inclined, it passes above or below the KOS without ever crossing the target.

3.2 Inspection Loop Analysis

The inspection of the target is required in the close-approach and it must be carried out at short range, using relative trajectories that permit observations from multiple viewing angles while preserving passive safety.

In this section, a WSE trajectory - already introduced in 2.3.2 and hereafter referred to as the Inspection Loop (IL) — is optimized. The IL stating range considered is between -1 km and -740 m (where the ellipsoid starts), behind the target's orbit and terminates on the Hold Trajectory (SE).

Time of inspection

The duration of the Inspection Loop is not predetermined; it is governed by the specific mission objectives and operational constraints. Drawing on the mission scenarios discussed in [21] and [46], together with the sensor capabilities outlined in paragraph 2.2, the sailcraft time-of-flight (ToF) for inspection is bounded between a minimum of five target revolutions, approximately nine hours, and a maximum of 24 hours. The upper limit is chosen both in line with the cited references and for computational efficiency, although longer inspection times remain feasible if required.

With regard to the observation distance, the maximum operating range of the LiDAR sensor, specifically used in the context of Active Debris Removal (ADR), is 1 km. Consequently, the maximum extension range of the IL is $\pm 1000\,\mathrm{m}$.

3.2.1 Test Case

Initial guesses for the state and control variables required by GPOPS-II are generated by starting from the desired final point on the safety ellipse (SE). Four points on the optimized safety ellipse (Fig. 3.8), evenly spaced along the first revolution of the chaser orbit, are selected to limit the scope of analysis. These target points, listed in Table 3.5, define the desired final states for the WSE trajectory.

The hold trajectory corresponding to a maximum cone angle of 85° is chosen since this configuration, as described in Section 3.1, produces the most stable hold trajectory, exhibits minimal drift along the V-bar and most closely approximates an ideal SE. The same maximum allowable α value is applied in the subsequent IL discussion. For further details on the optimization formulation, refer to Section 2.5.2 and Appendix B.4.

Target	α	δ	State vector $[x,\ y,\ z,\ \dot{x},\ \dot{y},\ \dot{z}]$
1	84.481°	−180°	[1.4195, −194.2959, −103.8081, −0.0971, −0.0028, −0.0049]
2	84.481°	−180°	[−97.4207, −1.8025, −4.6959, −0.0012, 0.1944, 0.1034]
3	84.481°	−180°	[−1.4618, 195.3918, 103.1717, 0.0973, 0.0029, 0.0046]
4	84.481°	−180°	[97.5469, 2.6670, 3.8516, 0.0012, −0.1947, −0.1034]

Table 3.5: Control and state vectors of target points on the Hold Trajectory (SE).

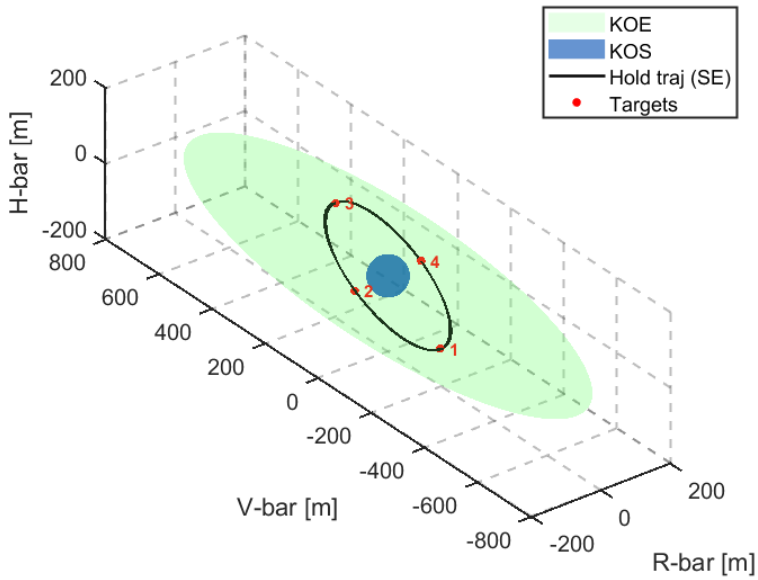

Figure 3.8: Illustration of the 4 equally spaced target points on the Hold trajectory(SE).

For each terminal point, an initial-state guess is produced by propagating the dynamics backward for 14 target revolutions ($\approx$ 24 hours). Every component of the resulting state vector is then scaled by a uniform factor of 1.5, ensuring that the starting point lies outside the outer ellipsoid. The corresponding control guess employs a constant cone angle of 85°. Since as can be seen in the safety assessment 3.1.3 by propagating a point along the Hold Trajectory with a constant cone angle 85°, the trajectory remains with almost zero V-drift, an artificial drift is introduced by subtracting a value of $\epsilon = -0.001 m/s$ from along-track velocity component, introducing the required drift along the V-bar direction and obtaining an initial guess that has a Walking-Safety Ellipse behaviour.

The initial guesses results in the state guesses in Table 3.6:

Case	α	δ	State vector $[x;\ y;\ z;\ \dot{x};\ \dot{y};\ \dot{z}]$
1	85°	0°	$[1.9366;\ -715.2710;\ -155.6077;\ -0.1485;\ -0.0054;\ -0.0155]$
2	85°	0°	$[-146.0923;\ -404.5742;\ -6.7093;\ -0.0044;\ 0.2900;\ 0.1467]$
3	85°	0°	$[-146.0923;\ -404.5742;\ -6.7093;\ -0.0044;\ 0.2900;\ 0.1467]$
4	85°	0°	$[146.3576;\ -430.9976;\ 5.6721;\ -0.0012;\ -0.2936;\ -0.1634]$

Table 3.6: Controls and initial state vectors IL.

Optimized IL trajectories are obtained for all four target points. However only case 1 and 4 give in output a optimized trajectory which resembles more a WSE and loops around the Ellipsoid. These two "best" trajectory have their respective target points along the R-bar, so on the right and left with respect of the target.

Therefore, only results for cases 1 and 4 are discussed here, while the plots and control profiles for cases 2 and 3 are provided in the Appendix C.

Illumination conditions Since during the inspection the illumination of the sensor is fundamental especially for cameras, the percentage of the optimized trajectory illuminated is

compared to the eclipsed one. Case 1 and Case 4 result in 62.7 % of the IL illuminated on the total ToF, meaning a total of 15.87 hours of illuminated trajectory.

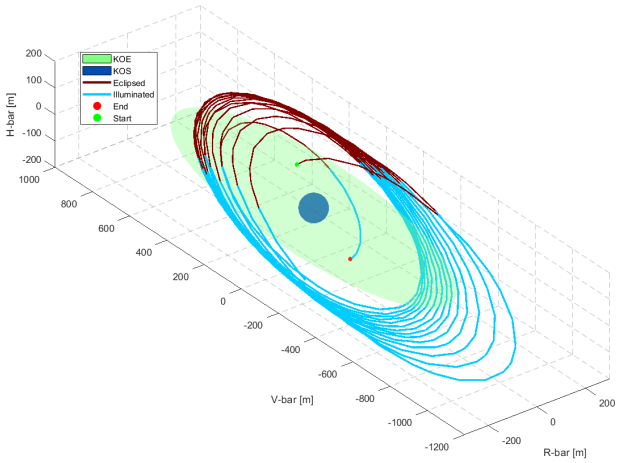

(a) IL Case 1

Figure 3.9: IL with eclipsed and illuminated trajectory segments highlighted. (a) Case 1.

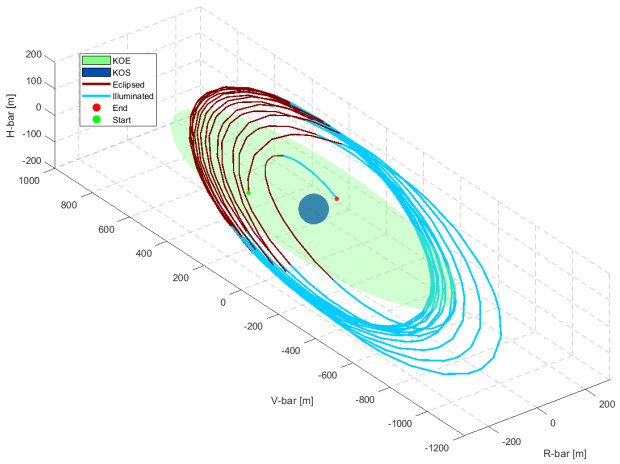

(b) IL Case 4

Figure 3.9: (continued) (b) Case 4.

The controls relative to the previously described IL are in Fig. 3.10.

In both Case 1 and Case 4, the cone angle, α, initially decreases slightly during the first revolution, resulting in increased SRP-induced acceleration (a_{SRP}). It then gradually increases toward the maximum allowable value of 85°, which reduces the acceleration. After this initial phase, α remains close to the upper limit with small oscillations during sunlit periods. In Case 1, the clock angle, δ, begins at $-180°$ and rises to approximately 100° during the first illuminated arc. It then resets to $-180°$ upon re-entering eclipse. In the following revolutions, δ evolves across

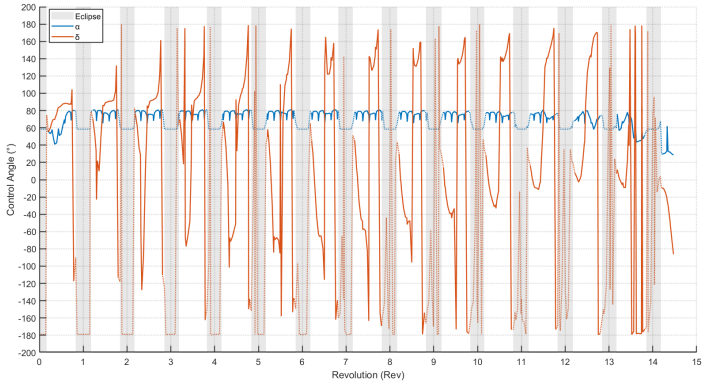

(a) Control IL Case 1

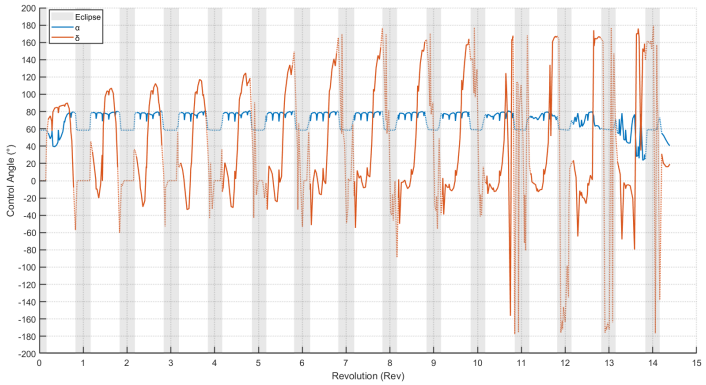

(b) Control IL Case 4

Figure 3.10: Control of IL for Case 1 and 4.

the full range between $-180°$ and $+180°$. The abrupt changes observed at the eclipse transitions are numerical artifacts resulting from the direct collocation method used in GPOPS-II; since SRP is zero during eclipse, the control has no physical effect in that phase, and the solver is free to adjust the control arbitrarily.

In Case 4, the clock angle, δ, starts at $0°$ upon eclipse exit and increases toward $+180°$ during the first revolution. Over time, it also exhibits full-range variation between $-180°$ and $+180°$. However, the transitions in this case appear smoother and less abrupt than in Case 1, likely due to different initial guesses imposed for this trajectory.

3.2.2 Safety assessment

The IL is optimized to stay out of KOE ensuring mission safety and passively avoiding the risk of collision with the target. However the possibility that the sail gets stuck in a certain attitude persists; therefore a safety assessment is performed through a Montecarlo analysis. This study is carried out to quantify the minimum separation that would be maintained in the event of an attitude-hold failure. The safety study is performed by randomly sampling points along the optimised IL trajectory (Case 1), freezing both the cone angle α and clock angle δ

at their commanded values at each sampling instant, and then propagating the resulting state with constant attitude for 50 revolutions of the target. For each of the 1,000 Monte Carlo simulations,the minimum separation between the chaser and the target is recorded and these values are used to construct the histogram in Fig. 3.11. The average of these minima is 169.7 m, while the closest recorded approach is around 4 m and occurred only once in the Monte Carlo analysis.

Section 2.2 describes how the 50 m radius of the keep-out sphere already includes a safety margin of two plus a o1σ uncertainty allowance. Without these margins, the combined hard-body radii of the chaser and target sum to just 8 m. Accordingly, although separation distances below 50 m (i.e., below the red threshold line in the histogram) carry a non-negligible collision risk, any approach within 8 m would inevitably result in impact.

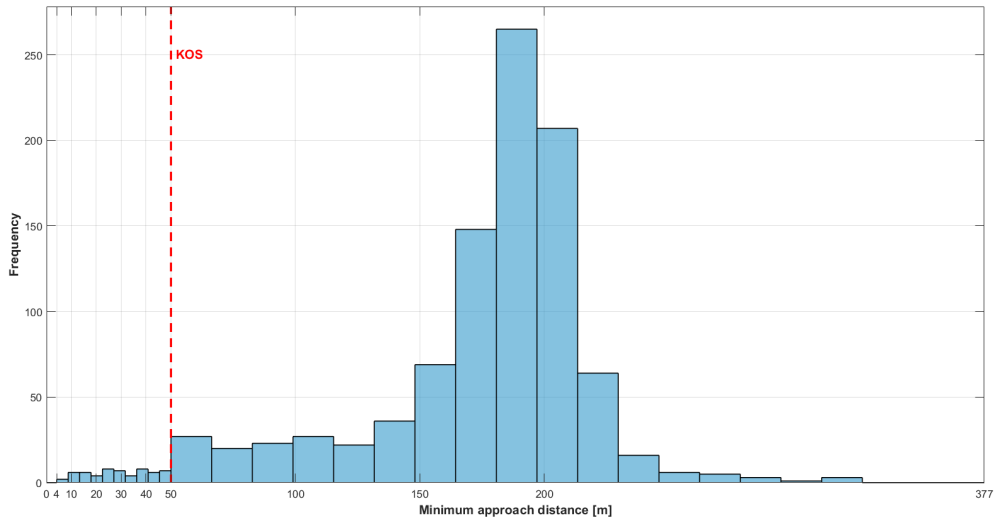

Figure 3.11: Monte Carlo Safety Assessment. A red threshold line indicate the limit (0-50 m)where the KOS, so the inner safety volume starts.

Plotting the forward propagation of the optimized IL initial state that produced the lowest minimum distance in the Monte Carlo analysis reveals that the smallest separations occur immediately after propagation begins. Figure 3.12 illustrates the propagated trajectory of this initial state over 50 revolutions, with a minimum separation of 4 m from the target, and depicts how the chaser subsequently drifts away along the V-bar direction.

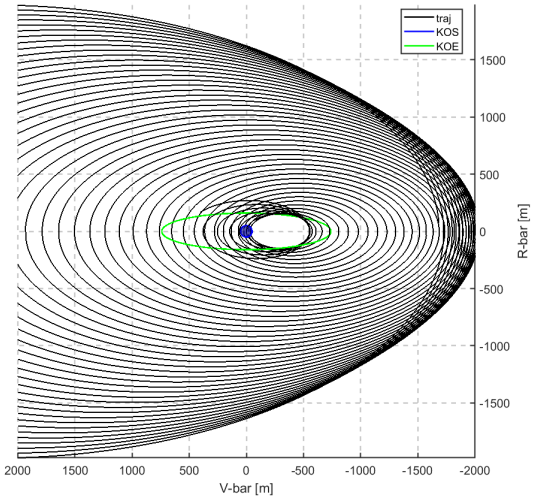

(a)

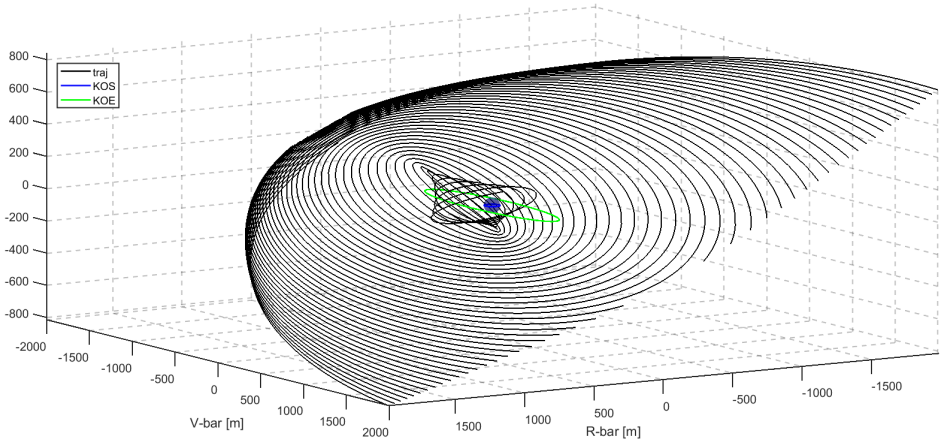

(b)

Figure 3.12: Forward propagation with fixed controls over 50 orbital revolutions of the state on the optimized IL that results in a minimum separation of 4 m.

3.3 Transfer Trajectory Analysis

The transfer begins on a target point of a Hold Trajectory (SE) placed behind the target at -1 km and end on aselected target point on the IL. The Hold Trajectory (SE) considered is optimized to stay in its Hold Volume for a max of 10 revolution.

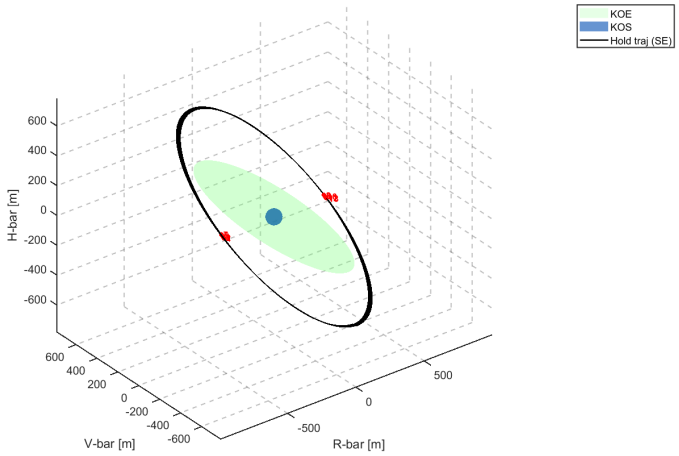

Figure 3.13: SE with 4 selected target points.

In Tab. 3.7, the initial guess used to obtain the SE is presented. From the SE, four points on the first optimized orbital revolution are selected just below and just above the 0 H-bar plane 3.13.

x_0	y_0	z_0	$\dot{x}_0$	$\dot{y}_0$	$\dot{z}_0$	α	δ	KOS radius	KOE
0	-750	-375	-0.3741	0	0	90°	0°	50 m	600x1000 m

Table 3.7: SE/Hold trajectory setup: initial state, constant control angles, and keep-out geometry.

Regarding the final target points, four locations are selected on the IL for Case 1 (see Sec. 3.2). The target points on the IL and SE are listed in Tab. 3.8 and Tab. 3.9, respectively.

IL	α	δ	State vector $[x;\ y;\ z;\ \dot{x};\ \dot{y};\ \dot{z}]$
1	53.49°	59.49°	$[258.0375;\ -455.3224;\ 7.4890;\ 0.0213;\ -0.5487;\ -0.1869]$
2	53.26°	59.77°	$[258.5977;\ -475.3433;\ 0.6735;\ 0.0093;\ -0.5494;\ -0.1869]$
3	53.17°	59.88°	$[258.7193;\ -495.3753;\ -6.1390;\ -0.0027;\ -0.5493;\ -0.1867]$
4	79.81°	113.99°	$[-297.1771;\ -282.3618;\ 12.8284;\ 0.0474;\ 0.5869;\ 0.1838]$

Table 3.8: Final target states on the IL.

SE	α	δ	State vector $[x;\ y;\ z;\ \dot{x};\ \dot{y};\ \dot{z}]$
1	81.9652°	−179.9361°	[376.5301; −989.4622902; 5.6121; 0.0071; −0.7512; −0.3727]
2	81.6607°	−179.9461°	[376.5895; −998.9733921; 0.8933; 0.0023; −0.7514; −0.3728]
3	80.7967°	−179.9635°	[376.5660; −1013.241004; −6.1853; −0.0048; −0.7513; −0.3727]
4	79.1014°	−179.7493°	[−374.7901; −975.1253975; 12.2216; 0.0124; 0.7480; 0.3731]

Table 3.9: Initial target states on the SE.

The optimization problem and logic is formulated in Section 2.5.2 and has two simultaneous goals: (i) to minimize the error between the velocity offset Δv and (ii) terminal-position mismatch small Δr, both between the transfer end-state and its corresponding target IL point, and the transfer initial-state and between its counterpart on the Hold Trajectory (SE).

Four transfers are analysed, each pairing a target state on the IL with its corresponding state on the SE (e.g., IL 1 with SE 1, and so on). The target points along the Hold Trajectory for the WSE are shown in Fig. 3.13, while those selected behind the target on the SE are displayed in Fig. 3.14.

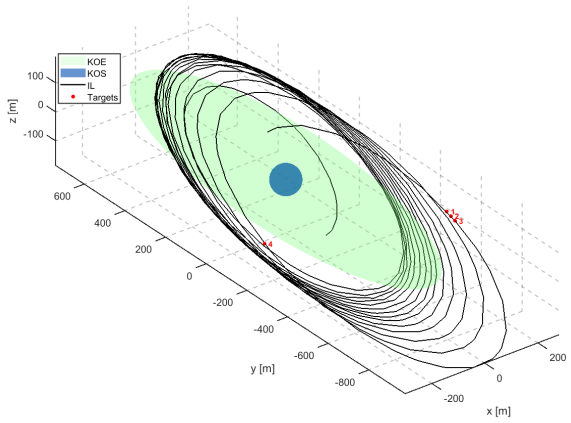

Figure 3.14: IL with 4 selected target points.

For combination from 1 to 3, to generate the initial guess state the following strategy is adopted: the final target state on the IL are propagated back in time for 1 orbital revolution of the target, then the final state of this propagation is used as initial guess and propagated forward for 1 revolution of the target.

For the fourth transfer a different propagation time is used, since using the previous described strategy the final state obtained is too far from the wanted initial state (at ≈ -1 km along the V-bar). Therefore the target state 4 on the IL is propagated back in time for 10 orbital revolution and the found final state is used as initial state and propagated again forward for the same time interval. For the control initial guess, a constant control with clock angle $\alpha = 85°$ and cone angle $\delta = -90°$ is used. A summary of the strategy discussed previously is given in Table 3.10. That table summarizes the initial guesses used for the propagation: "Revs" is the number of target revolutions propagated backward/forward, and "IN" and "FIN" report the position/velocity mismatches at the start and end of the optimized transfer, respectively.

Case	Revs	Initial-guess state	IN error		FIN error	
			Δr[m]	Δv[m/s]	Δr[m]	Δv[m/s]
1	1	$[261.4536; -1092.5173; 5.9992; 0.0189; -0.5549; -0.1870]$	14.17	0.10	10.11	0.08
2	1	$[261.9182; -1104.6497; -0.8161; 0.0069; -0.5554; -0.1869]$	14.17	0.10	6.80	0.06
3	1	$[261.9441; -1118.2066; -7.6268; -0.0051; -0.5551; -0.1866]$	13.02	0.10	10.05	0.08
4	10	$[-264.6399; -849.8129; 12.7735; 0.0493; 0.5280; 0.1838]$	7.14	0.06	4.80	0.004

Table 3.10: Initial-guess propagation: "Revs" is the number of revolutions propagated; "IN" and "FIN" denote the position/velocity mismatches at the transfer start and end.

Test cases

Four optimal transfers are found; however, Transfers 1, 2, and 3 show a mismatch with their respective desired initial states (on the SE), with an initial position error (δr) ranging from approximately 13 m to 14 m. For the final position, the error with respect to the target state on the IL ranges from approximately 7 m to 10 m. Velocity differences on the final an initial state are too large to make to make the transition from the Transfer to the IL and from the Hold Trajectory (SE) to the Transfer flyable by a solar sail, which has not impulsive but continuous thrusting. If lower δ are searched by enforcing lower tolerances the optimizer does not converge.

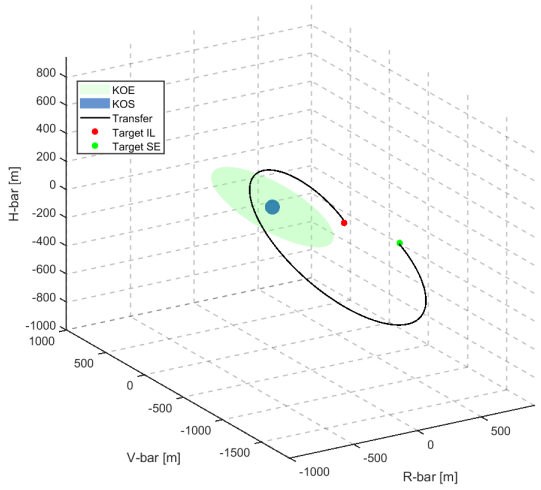

(a) Case 2 Transfer.

Figure 3.15: Trajectory and control of Case 2 Transfer.

Figure 3.15b shows the control angles for Case 2 Transfer. When the sailcraft trajectory is illuminated, the cone angle α starts just under 80°, then gradually decreases to just below 60° before slightly increasing again toward the end of the revolution. The clock angle δ begins just below 20°, then progressively decreases toward −180° during the sunlit phase. Shortly before the spacecraft enters eclipse, δ rises slightly to around −160°.

Transfer 4 has lower δ, especially δ_v on the final target velocity which is 0.004 m/s and δ_r is 4.8 m. The δ_r and δ_v on the initial state are greater but sill lower if compared to the other transfers. Transfer 4 achieves the lowest overall misalignment, with a velocity error at the final

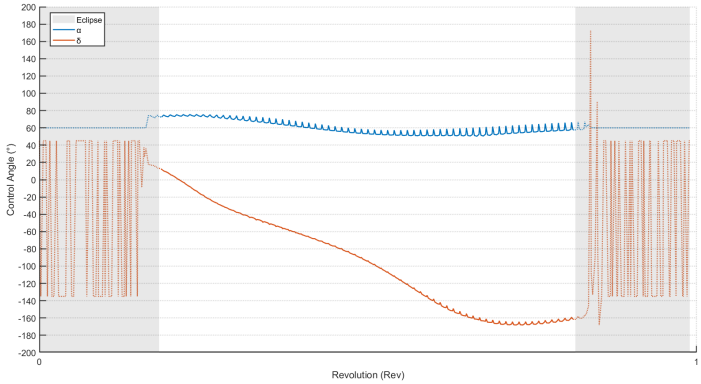

(b) Control of Case 2 Transfer.

Figure 3.15: (continued) Trajectory and control of Case 2 Transfer.

state of only δ_v ≈0.004 m/s and a position error of Δ_r ≈4.8 m. While the initial state errors in position and velocity are greater than those at the final state, they remain smaller than those observed in the other three transfers.

This outcome reflects the flow of the optimization process, which aims to minimize mismatches at both the initial and final states within the defined tolerance settings. Depending on the specific combination of tolerances chosen in the setup, the optimizer may favour a lower error at either the initial or final state. Consequently, the final optimized solution represents a trade-off between minimizing errors at both ends of the transfer.

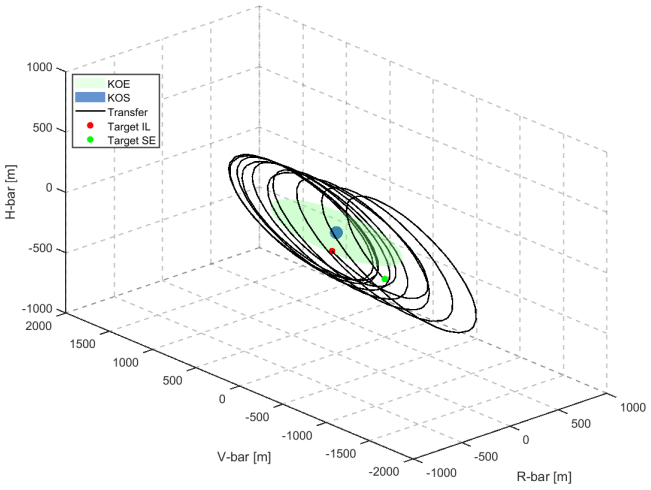

(a) Case 4 Transfer.

Figure 3.16: Trajectory and control of Case 4 Transfer.

Figure 3.16b shows the control angles for Case 4 over ten orbital revolutions. The cone angle α begins at approximately 80° and exhibits a smooth oscillation throughout the illuminated arcs. Its amplitude remains bounded between an upper limit close to 80° and a lower limit slightly

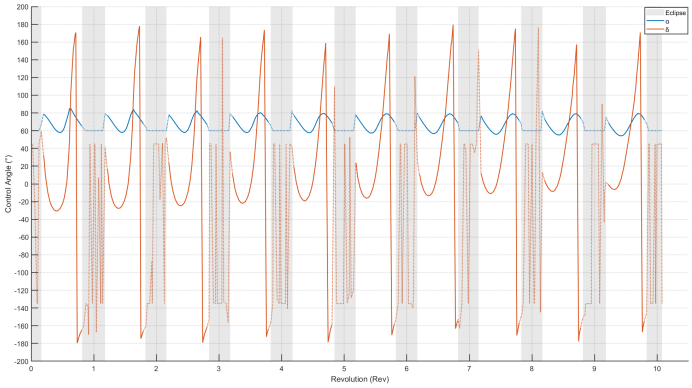

(b) Control of Case 4 Transfer.

Figure 3.16: (continued) Trajectory and control of Case 4 Transfer.

below 60° across all revolutions.

The clock angle δ starts near 20°, decreases to approximately −30°, then rises sharply to around 170°, and finally drops to −180° just before entering eclipse. In the following revolutions, the control follows a similar overall shape, but the maximum and minimum values are not strictly periodic. Specifically, the maximum values reached vary between approximately 160° and 180°, while the minimum values range between −160° and −180°. This indicates a recurrent but not fully periodic control profile.

3.4 Discussion

The analyses presented in this chapter demonstrate that inclined hold trajectories (SE) and inspection loops (IL) are feasible using solar-sail propulsion. More importantly, they are safe relative motions, as shown in the safety assessment study. The transfer from a Hold Trajectory in the far-range rendezvous phase to the IL remains challenging under the current design scenario.

Hold Trajectory When the maximum cone angle is constrained to $\alpha_{\max} = 85°$ or 80°), the solver naturally drives the sailcraft to its upper limit throughout the orbit, minimizing drift and keeping the chaser well within the nested KOZs for ten target revolutions. Even if the sail becomes "stuck" at a fixed attitude, the almost constant control profile preserves the nominal hold path and avoids collision. As the cone-angle constraint tightens (down to 70° and below), drift in the V-bar direction becomes more significant, and the trajectory does not resemble the classical safety ellipse; nevertheless, it remains inclined above or below the KOS, preserving passive safety.

Inspection Loop Among four equally spaced terminal points on the SE, two produced IL solutions (Cases 1 and 4) that loop around the ellipsoid and maximize illumination ($\approx$ 62.7 % of the ToF). These "best" loops maintain good sensor visibility while satisfying KOZ constraints. A safety assessment, with a 1000-samples Monte Carlo analysis, confirms minimum separations with no trials resulting in collision. The other two cases (Cases 2 and 3), presented in Appendix C, do not exhibit the desired looping behaviour. Although the optimization reaches the target

state points, the trajectories remain outside the KOE along the negative V-bar throughout the ToF and do not drift over the KOE. As these results do not resemble the intended IL behaviour, they are not discussed in detail here.

Transfer Trajectories Linking SE and IL via optimal transfers proved the most challenging task, especially matching position and velocity to within a few meters and millimetres per second of accuracy. Case 4 achieved the best performance (Δr= 4.8 m, Δv=0.004 m/s at the IL), but other design scenarios without the Sun in the orbital plane could provide better results. The transfer studied is complex because it requires a change in the eccentricity of the orbit. One of the main difficulties with the transfer is that the Sun is in the orbital plane, which makes it very difficult to change the eccentricity of the orbit. In reference [47] it has been proven that changing from a circular or elliptical orbit, when the Sun is in the orbital plane, is very challenging; if the problem were changed to one where the chaser and target are perpendicular to the direction of the Sun, i.e. in a polar orbit (AA=0°), this could be an easier scenario and could improve the results. In addition, the transfer time in this problem is not optimized but rather assumed based on a guessed value, with a narrow allowed range (e.g., between 10 and 12 target revolutions). This constraint could, in general, prevent the optimizer from finding better solutions that require shorter times of flight. For instance, if the true optimal ToF were closer to 9 revolutions, such a solution would be excluded. In this specific case, preliminary tests showed that, with the chosen initial guess for Case 4 Transfer, a time of flight shorter than 10 revolutions was not sufficient to complete the transfer, confirming that a minimum ToF $\geq 10, T_t$ is justified. In this regard, a future optimization could explore not only progressively tightening the tolerances on the initial and final state mismatches, but also relaxing the constraints on the transfer time, as this may lead to even better alignment with the desired target states.

Verification and Validation of the results To ensure the physical consistency of the optimized trajectories, a forward propagation of the state using the control profiles obtained from GPOPS-II is performed. This validation process is detailed in Appendix A.5 and includes the SE, IL, and Transfer trajectories. Forward integration is used to verify that the optimized solutions are not only valid at the collocation nodes but also satisfy the constraints and system dynamics between them. This validation confirms the accuracy of the optimizer and the resulting control profiles, as the forward-propagated trajectories closely follow the optimal state vectors in output from GPOPS-II in all three cases. This consistency is particularly evident when a finer initial mesh and strict mesh error tolerance are used.

Chapter 4

Parametric Analysis

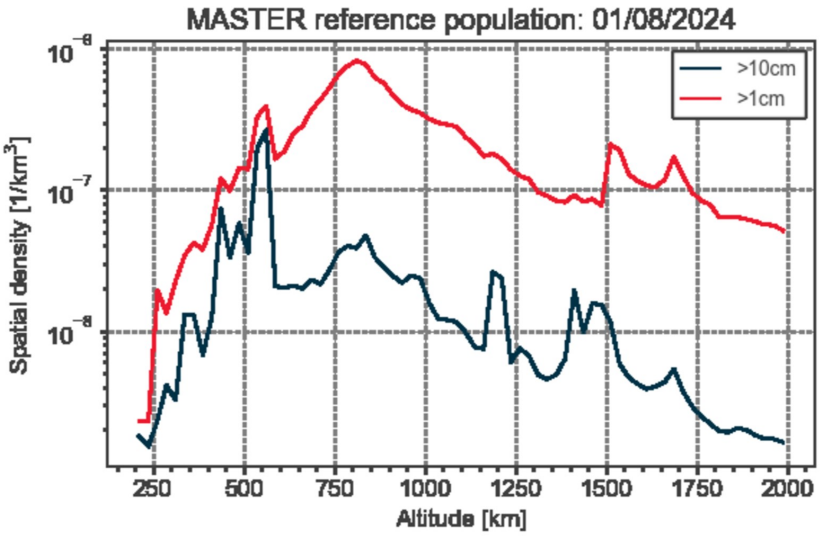

Figure 4.1: Spatial and temporal distribution of space debris and orbital objects [1].

As shown in Fig. 4.1 from [1], the density of debris > 10 cm (red line) in Low Earth orbit (LEO) shows an increasing trend starting from 250 km, with a peak around 850 km, then decreasing with secondary peaks at approximately 1400 km and 1700 km.

In order to consider additional scenarios beyond the one analysed in Chapter 3 and to conduct a comprehensive analysis, a parametric study is carried out. The optimization setup is the same as that used for the Hold Trajectory discussed in Section 2.5.2. Regarding the control, all parametric analyses are conducted by constraining $\alpha_{\max}$ to 85°. As previously stated, a cone angle of 90° would result in zero acceleration, causing the sailcraft to follow a purely Keplerian trajectory in the absence of other perturbations. Moreover, solar sail missions typically impose an upper bound on the cone angle.

The following parameters are varied:

- Orbit altitude (km);
- Initial true anomaly (ν°);

- Characteristic acceleration a_c (by adjusting the sail parameter β);
- Aspect angle (AA);
- KOZs size;

The three selected altitudes (850 km, 1000 km, and 1400 km) correspond to the main peaks in spatial density of space debris in Fig. 4.1: 850 km to the first peak, 1400 km to the second major peak following 1000 km, which is the altitude at which the analysis in Chapter 3 has been conducted.

Four values of true anomaly (TA) (0°, 90°, 180°, and 270°) are considered to represent equally spaced positions along the orbit, thus capturing four distinct starting illumination conditions.

For the characteristic acceleration, three values are analysed: 0.000046 m/s^2 as the one of the sail of the ACS3 mission [15], while 0.0001 m/s^2 and 0.000023 m/s^2 correspond to approximately twice and half that value, respectively.

The "Aspect Angles" (AA) is defined as the angle between the line of the Sun and the orbital angular momentum vector. Variations in AA take into account different orbital inclinations and the right ascension of the ascending node (RAAN). For example: equatorial orbits have AA = 90° and inclination $i = 0°$, while polar orbits can have AA = 90° or 0° with $i = 90°$:

- When AA = 90°, the RAAN is 0°;
- When AA = 0°, the RAAN is 90°;

Two configurations are also considered for the keep-out sphere (KOS): a 50 m radius, obtained using the strategy described in Section 2.2 with a safety factor of 2, and a 40 m radius, corresponding to a reduced safety factor of 1.5. Similarly, two sets of dimensions are evaluated for the keep-out ellipsoid (KOE): 160×740×160 m (safety factor of 2) and 122×552×122 m (safety factor of 1.5), both derived using the same methodology described in Section 2.2.

The specific values of the parameters used in the analysis are listed in Table 4.1.

Table 4.1: Parameters used in the parametric analysis.

Parameters	**Value 1**	**Value 2**	**Value 3**	**Value 4**
True anomaly (°)	0	90	180	270
Altitude (km)	850	1000	1400	-
AA (°) (i and Ω)	90 (equatorial)	0 (polar)	90 (polar)	-
a_c (β) (m/s^2)	0.0001	0.000023	0.000046	-
KOS - KOE (m)	50 160×740×160	50 122×552×122	40 160×740×160	40 122×552×122

All combinations in the parametric analysis result in a total of 432 cases. These are divided equally among the four KOS-KOE configurations, with 108 cases corresponding to each configuration. For each group of 108 cases, the same initial guess (reported in Table 4.2) is used, resulting in a total of four distinct initial guesses. For all 432 cases, an optimal solution is successfully found. This confirms that a Hold trajectory, remaining inside the outer KOE and outside the inner KOS, is always feasible, regardless of the orbital configuration.

Examining the resulting optimal trajectories, it becomes clear that the orbit does not always resemble a typical safety ellipse. In many cases, a significant drift along the V-bar direction is observed, despite the drift being limited by an additional constraint on the state, ensuring that the maximum value of y did not exceed $2x_{\max}$.

Value	KOS	KOE	α	δ	State vector $[x;\ y;\ z;\ \dot{x};\ \dot{y};\ \dot{z}]$
1	50m	160×740 m	90°	0°	$[0;\ -210;\ -105;\ 0;\ 0;\ 0]$
2	50m	122×552m	90°	0°	$[0;\ -172;\ -86;\ -0.0857981102033735;\ 0;\ 0]$
3	40m	160×740m	90°	0°	$[0;\ -200;\ -100;\ -0.0997652444225273;\ 0;\ 0]$
4	40m	122×552m	90°	0°	$[0;\ -162;\ -81;\ -0.0808098479822471;\ 0;\ 0]$

Table 4.2: Initial guesses for both the state vectors and control angles in each hold trajectory scenario considered in the parametric analysis. The corresponding KOZ sizes are also provided.

Evaluation of V-bar Drift

The secular drift along the V-bar direction, denoted as V_{bar}, is evaluated by analysing the oscillatory motion of the relative trajectory over time and studying its deviation from the desired SE trajectory, which is inherently periodic. For each optimal solution trajectory, we compute the sets $\{V_{\max,i}\}$ and $\{V_{\min,i}\}$ in meters. The drift along V-bar for each trajectory is calculated as:

$$\Delta_{\max} = V_{\max}^{\max} - V_{\max}^{\min}, \tag{4.1}$$

$$\Delta_{\min} = V_{\min}^{\max} - V_{\min}^{\min}. \tag{4.2}$$

The final value of the **maximum absolute secular drift** along the V-bar axis is defined as:

$$\boxed{\text{Drift}_{V\text{-bar}} = \max(\Delta_{\max},\ \Delta_{\min}).}$$

In Fig.4.6 maximum drift along the V-bar per altitude is compared for all the scenarios.

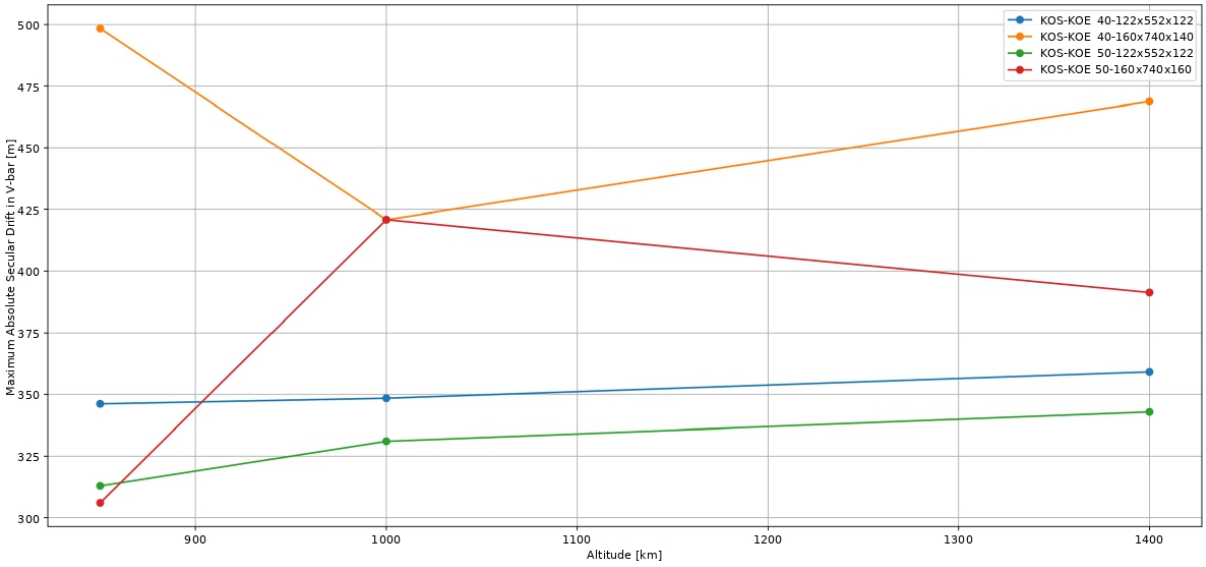

Figure 4.2: Maximum Absolute V-bar Drift vs Altitude by KOZs configuration.

It can be noticed that at the same altitude the drift in the V-bar direction increases as the volume between the KOZs used to design delimit the allowable zones grows. So more stable

trajectories are found with the narrowest combination of KOZ: 50 m of radius for KOS and 122X522X122 for KOE.

The orbits that experience the highest drift are the polar ones with AA=90° as can be seen in Fig. 4.3.

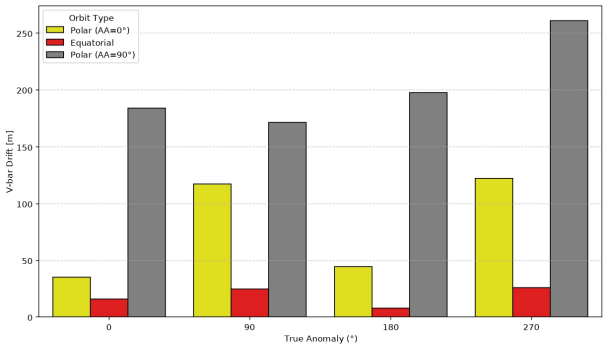

(a) V-bar drift for KOZ value 1

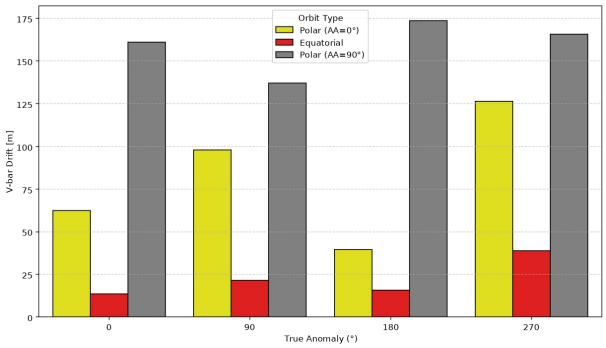

(b) V-bar drift for KOZ value 2

Figure 4.3: Comparison of V-bar drift by True Anomaly and Orbit Type for different Keep-Out Zone (KOZ) values: (a) KOZ value 1 and (b) KOZ value 2.

A peculiar behaviour is observed with the same Aspect Angle (AA) of 90° for equatorial and polar orbits. At the same orbital parameters (except inclination) the polar trajectories have a higher drift than the equatorial orbits. As can be seen in Fig. 4.4 when plotting the acceleration, a different behaviour is particularly evident in the z-direction. The z-acceleration is higher for the equatorial orbit, suggesting that the gravitational acceleration is more effectively compensated in this configuration. In contrast, for the polar orbit, the z-acceleration is lower, indicating that the out-of-plane component is less compensated. This leads to an increased out-of-plane drift in the relative trajectory, as also observed in the plots.

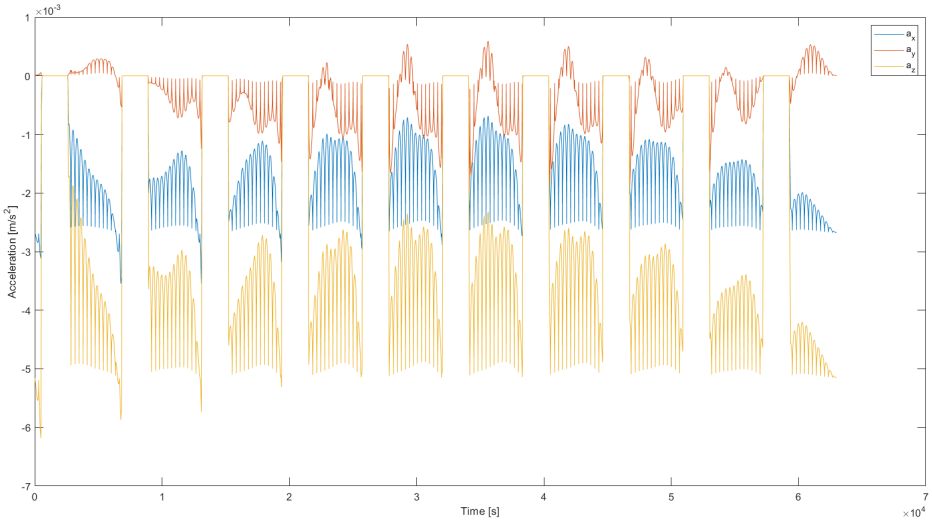

(a)

Figure 4.4: Acceleration (SRP) for equatorial orbit. Both orbits have the same orbital parameters with AA $= 90°$, $\nu = 270°$, $a_c = 1 \times 10^{-4}\,\mathrm{m/s^2}$, and $h = 1000$ km.

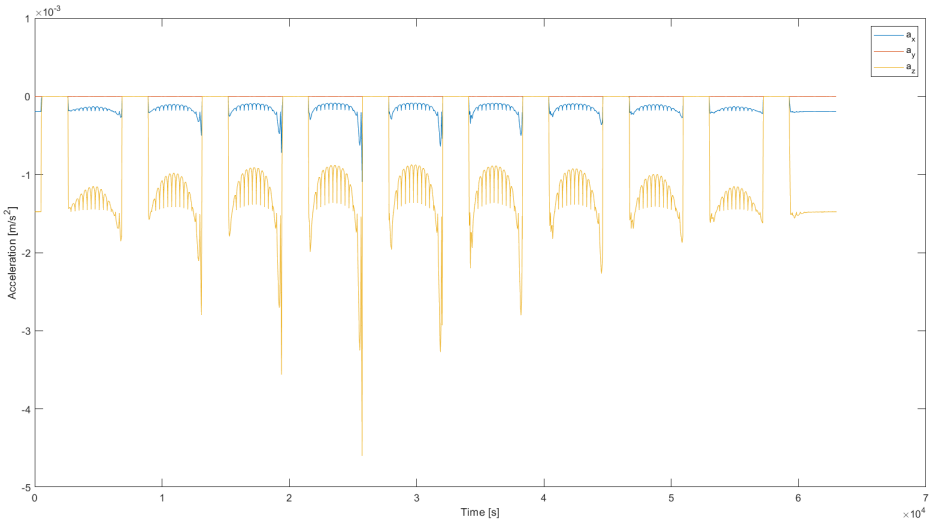

(b)

Figure 4.4: (continued) Acceleration (SRP) for polar orbit.

In conclusion a similar trend can be observed that suggest the use of equatorial orbits for more stable trajectories for larger and smaller KOZs, instead for polar orbits narrower KOZs would be necessary to maintain the desired Safety Ellipse behaviour. For what concerns the property of the sail, it is observed that varying the lightness number and therefore the characteristic accelerations: smaller accelerations tend to a better performance since the sail tends to follow a point mass behaviour and the effect of the SRP is reduced. In Fig. 4.5 it can be seen that, by

decreasing the characteristic acceleration, the trajectory approaches a Keplerian orbit; however, since SRP is still present, the motion is not truly Keplerian. As a result, in some cases, having less SRP leads to better performance because the trajectory requires less control effort, while in other configurations, higher SRP would be beneficial to increase manoeuvrability.

Analysing both heatmaps from an altitude point of view, it is apparent that, in general, a lower characteristic acceleration a_c is favourable, since the optimized trajectories have the smallest V-bar drift. However, higher values of a_c become more effective at reducing drift as altitude increases. In Figure 4.5a, for instance, the drift at 850 km for $a_c = 1.0 \times 10^{-4}\,\mathrm{m\,s^{-2}}$ is 138 m, whereas increasing the altitude to 1400 km reduces the drift to 119 m under the same a_c.

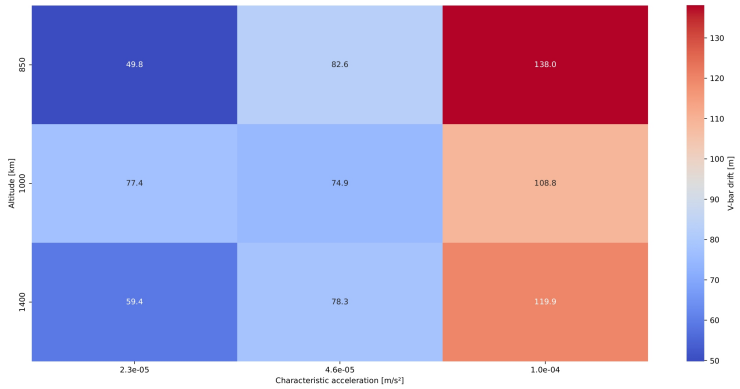

(a)

Figure 4.5: (Continued) Heatmap: V-bar drift by altitude and characteristic acceleration – Case 4 of KOZs.

A similar trend is observed in Figure 4.5b: for $a_c = 4.6 \times 10^{-5}\,\mathrm{m\,s^{-2}}$ and $a_c = 1.0 \times 10^{-4}\,\mathrm{m\,s^{-2}}$, where the minimum drift occurs at 1400 km.

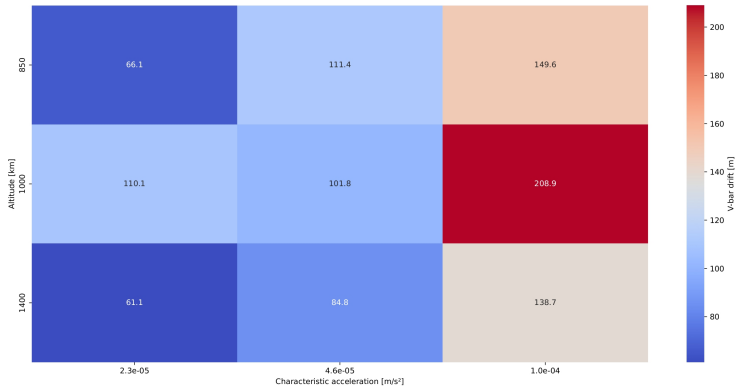

(b)

Figure 4.5: Heatmap: V-bar drift by altitude and characteristic acceleration – Case 3 of KOZs.

Reduction of V-bar Drift

In Fig. 4.6, the maximum absolute V-bar drift is identified for each KOZ configuration as a function of orbital altitude. To determine whether these drifts resulted from a bad initial guess, the optimization is re-run for each case using, as the initial guess, the locally optimal solution whose V-bar drift is already near zero. The resulting improvements in V-bar drift are presented in Tables 4.3—4.6.

To facilitate a comparison, for each Value of KOZ, a parameter configuration is chosen that optimized resulted in a locally optimal solution with more drift along the V-bar direction. Only the altitude is varied between 850 km, 1000 km, and 1400 km.

Value 1: KOS = 50 m, KOE = 160×740 m

Case	TA [°]	Altitude [km]	AC [m/s²]	AA [°]	Orbit Type	Original Drift [m]	Optimized Drift [m]
1	270	850	1.0×10^{-4}	90	Polar	306.01	61.42
2	270	1000	1.0×10^{-4}	90	Polar	420.91	85.04
3	270	1400	1.0×10^{-4}	90	Polar	391.30	46.69

Table 4.3: V-bar drift improvement using initial guess from previous optimization (Value 1)

Value 2: KOS = 50 m, KOE = 122×552 m

Case	TA [°]	Altitude [km]	AC [m/s²]	AA [°]	Orbit Type	Original Drift [m]	Optimized Drift [m]
1	180	850	1.0×10^{-4}	90	Polar	312.94	52.09
2	180	1000	1.0×10^{-4}	90	Polar	318.42	69.52
3	180	1400	1.0×10^{-4}	90	Polar	342.89	64.94

Table 4.4: V-bar drift improvement using initial guess from previous optimization (Value 2)

Value 3: KOS = 40 m, KOE = 160×740 m

Case	TA [°]	Altitude [km]	AC [m/s²]	AA [°]	Orbit Type	Original Drift [m]	Optimized Drift [m]
1	180	850	1.0×10^{-4}	90	Polar	384.90	165.97
2	180	1000	1.0×10^{-4}	90	Polar	384.33	81.84
3	180	1400	1.0×10^{-4}	90	Polar	468.76	92.73

Table 4.5: V-bar drift improvement using initial guess from previous optimization (Value 3)

Value 4: KOS = 40 m, KOE = 122×552 m

Case	TA [°]	Altitude [km]	AC [m/s²]	AA [°]	Orbit Type	Original Drift [m]	Optimized Drift [m]
1	90	850	1.0×10^{-4}	90	Polar	292.98	63.05
2	90	1000	1.0×10^{-4}	90	Polar	348.44	53.82
3	90	1400	1.0×10^{-4}	90	Polar	359.16	49.45

Table 4.6: V-bar drift improvement using initial guess from previous optimization (Value 4).

The table illustrates how orbital drift is influenced by varying altitudes, keep-out zone constraints (KOS and KOE), true anomaly (TA), aspect angle (AA), and characteristic acceleration (AC), considering only gravitational and solar radiation pressure (SRP) effects. A first optimal solution is obtained using constant control inputs, and a successive optimization — starting from the previous optimal solution as initial guess — results in a significantly reduced orbital drift, especially at higher altitudes where SRP-induced perturbations dominate due to the lower gravitational acceleration. An example of V-drift reduction by successive optimization is shown in Fig. 4.7.

Configurations with smaller KOS and more compact KOE dimensions allow for more effective optimization, likely because tighter constraints help focus the control effort and reduce unnecessary deviations. The true anomaly, which in this context refers to the target satellite, influences the initial relative geometry of the chaser-target system with respect to the Sun. Since the chaser's trajectory is defined relative to the target, variations in TA shift the entire configuration along the orbit, changing both the timing and starting of eclipse conditions.

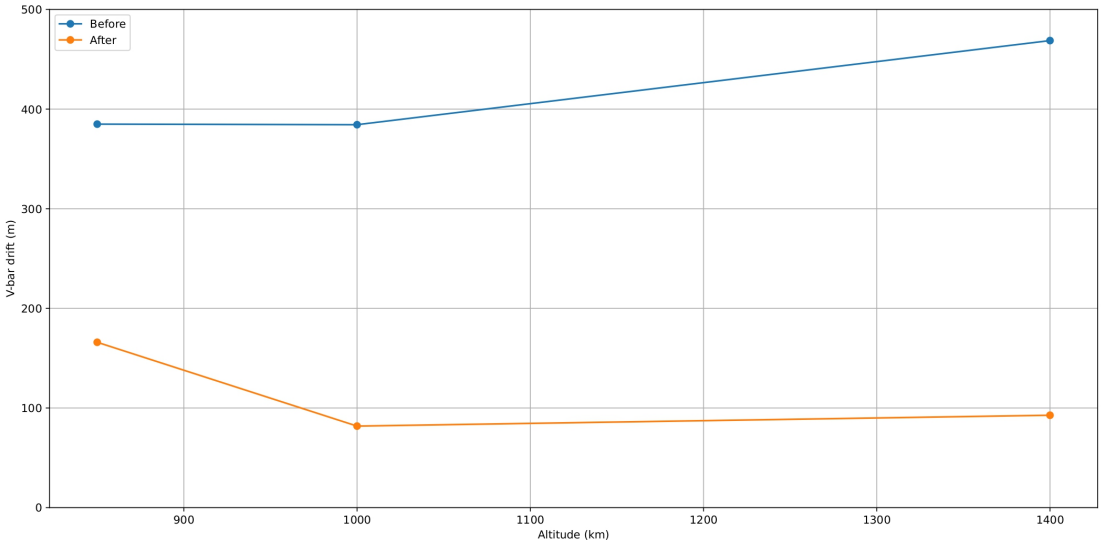

Figure 4.6: Maximum Absolute V-bar Drift vs Altitude by KOZ configuration (Value 3) using a locally optimal solution, with minimum drift in the V-bar direction, as the initial guess.

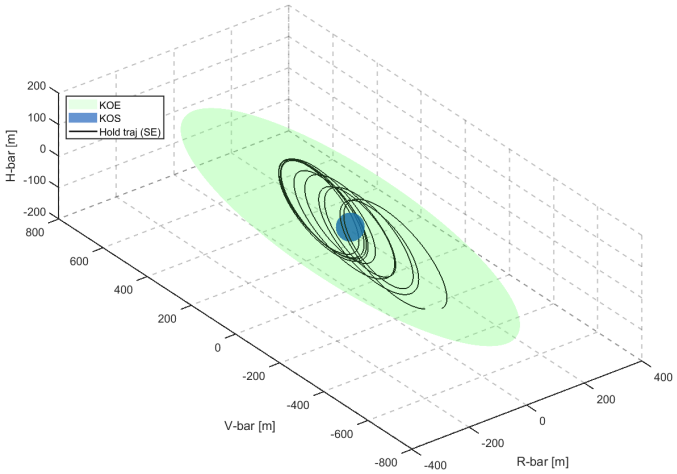

(a)

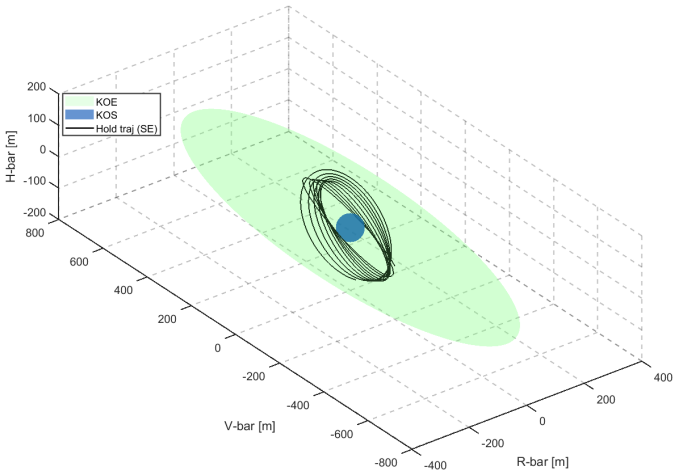

(b)

Figure 4.7: Comparison of V-bar drift for case 2 of value 3 of KOZs prior (a) and after (b) the successive optimization using as initial guess a previously found optimal solution.

Discussion

The parametric study confirms that Hold Trajectories (SE) remain feasible across a wide range of orbital altitudes, true anomalies, characteristic accelerations, aspect angles, and KOZ configurations: all 432 test cases converge in optimal solutions that respect the inner spherical and outer ellipsoidal keep-out volumes. However, the secular drift along the V-bar direction varies strongly with these parameters. In particular, higher altitudes and larger KOZ volumes produce larger drifts, since solar radiation pressure (SRP) perturbations dominate as gravitational acceleration decreases. Polar orbits (AA = 90°) consistently exhibit greater out-of-plane drift than equatorial orbits at the same altitudes, due to less effective SRP compensation in the

z–direction. Tighter KOZs (e.g. 50 m radius with 122 × 552 × 122 m ellipsoid) help constrain the drift. Finally, lower characteristic accelerations (smaller β) tend toward Keplerian-like behaviour and can reduce control effort, though excessively low SRP limits manoeuvrability and may increase drift in some configurations. Moreover, considering the optimal solutions obtained from successive re-optimization using optimal low-drift initial guesses (Tables 4.3–4.6), over 79.62% drift reduction is achieved in each of the three worst-case scenarios. This confirms that even the most adverse KOZ configurations admit feasible Hold–Trajectory solutions when initialized with a suitable guess — specifically, one exhibiting low V-bar drift. The largest absolute improvement occurs at 850 km. These findings not only validate the robustness of the Hold trajectory framework but also provide practical guidelines for mission design: favour lower altitudes with lower characteristic accelerations, and at higher altitudes employ higher a_c values and tighter KOZs.

Chapter 5

Conclusions and Recommendations

This thesis aims to contribute to the research gap in close-proximity operations using solar sail propulsion, building on previous research on phasing and far-range rendezvous operations with solar sails. The first section of this chapter contains the conclusions and evaluates the results obtained and puts them in relation to the research questions in Chapter 1, in order to assess whether and how far they have been answered. In the second section, recommendations for future work are proposed.

5.1 Conclusions

To answer the first research question,

What does an optimal trajectory for close-range operations look like with solar-sail propulsion?

this thesis explored Hold-Trajectories like Safety Ellipse and Inspection Loop, similar to the so-called Walking Safety Ellipse, to see whether inclined hold trajectories are feasible. These relative motions guarantee safety in close-proximity operations: the trajectory never crosses the velocity vector of the target, and the chaser never enters the inner keep-out volume, even when flying around it. This trajectory design approach answers the first research question.

This study has demonstrated that inclined Hold Trajectories can stay for an extended time interval (at least 10 target revolutions $\approx$ 17.5 hours) in defined Hold Volumes without colliding or exiting/entering the safety regions. It has been observed that constraining the cone angle leads to increased drift along the V-bar, while values closer to the upper bound (e.g., 90°) reduce drift by enabling more effective control.

The validity of these trajectories is assessed for multiple scenarios through a parametric analysis where various combinations of altitude (850, 1000 and 1400 km), KOZs, initial true anomaly, sail lightness number, AA and therefore orbit type (equatorial and polar) are tested.

A Walking Safety Ellipse-like relative trajectory of the chaser around the target is tested and optimized. Results show that Inspection Loop trajectories allow the sailcraft to approach the target while enabling its observation for an extended period of time. Furthermore, a useful

consideration for cameras and sensors used in ADR is that the optimal trajectories are illuminated for more than 62% of the total time of flight.

More optimal transfers are found; however, the Δv and Δr at the insertion point are not exactly zero, so further investigation is needed. Indeed, it won't be flyable by a solar sail since thrusting is continuous and not impulsive; therefore, more time for manoeuvring and transfer from the Transfer to the optimized IL is needed, since it is observed that better transfer has a longer ToF.

To find optimal trajectories and implement direct collocation methods, GPOPS-II is used. By answering the following research question,

Is direct collocation accurate, robust and suitable to obtain optimal close-range trajectories incorporating the main constraints?

it can be assessed whether this solution method is applicable to the problem scenarios under study. Indeed, optimal solutions are found for all the problems investigated, so the method is suitable and allows the incorporation of KOZs, control, state, and time constraints and bounds.

With regard to accuracy, answering the following subquestions provides a more detailed evaluation.

- *Accurate*: Does it compute trajectories that satisfy dynamics and constraints with sufficient precision not only at the collocation nodes? In Appendix A.5, forward propagation of the found optimal solution and control is performed to assess it. What can be seen is that, in general, the forward-propagated trajectories follow the optimal state vector of GPOPS-II. Thus, even between the collocation nodes, the constraints and the dynamics are satisfied, making them physically realistic trajectories. However, it has been noted that this is true only if a fine mesh with a high number of collocation points and a strict tolerance on the mesh error are used. A coarse mesh will more likely generate a less accurate trajectory.
- *Robust*: Can it consistently find feasible solutions even with uncertain inputs or poor initial guesses? Concerning this subquestion, it is found that the better the initial guess, the more physically feasible the solution is; hence, direct collocation highly depends on a good initial guess. This is true especially for highly constrained problems such as the Inspection Loop (IL) and Transfer problems where the initial guess did not exactly match the desired initial or final state bounds. Although initial guesses that closely satisfy the boundary constraints tend to produce better convergence, it is still possible to obtain feasible solutions even when the initial and final states did not match exactly. For the more challenging cases, in practice, techniques such as mesh refinement or intermediate solutions with relaxed constraints are used to guide the solver. This demonstrates that, although the method benefits from a good initial guess, it remains capable of converging towards optimal solutions under tight bounds.

  GPOPS-II, as the software used where direct collocation is implemented, reflects this behaviour. Moreover its adaptive mesh strategy adjusts the number of collocation points based on the user-defined allowable range. In some cases, this led to coarser meshes and slightly less accurate forward-propagated trajectories. Nevertheless, the method as a whole proved capable of converging to optimal and constraint-compliant solutions, even under tight bounds.
- *Suitable*: Is it capable of handling complex constraints (e.g., keep-out zones) efficiently ? It is possible to conclude from this study that Direct collocation is suitable for solving the types

of constrained trajectory optimization problems investigated in this work. The method successfully handled both single- and multi-objective formulations while incorporating complex constraints, including KOZs, control, state, and time bounds and constraints. GPOPS-II provided an effective implementation of the method across all test cases.

5.2 Recommendations

While this thesis has demonstrated the applicability of solar sails for close-proximity operations in ADR mission, several research gap still need to be filled and several problem addressed in this thesis require further investigation to ensure mission effectiveness. This section outlines the main recommendations for future work.

5.2.1 Simulation model

In this work the close-proximity operations study has been conducted considering mainly one scenario: the target is on a circular equatorial LEO orbit at 1000 km.

- **Sun Location:** The Sun is located at the autumnal equinox and its position is fixed along the negative X-axis, so it is assumed to be stationary. Consequently, the Sun lies in the orbital plane of both the target and the sailcraft, which increases the complexity of the optimization problem. One scenario to explore is a polar orbit with AA = 0°, which is investigated only for the Hold trajectory scenario but not for the Inspection Loop and Transfer. Exploring this scenario could potentially yield improved optimization results.
- **Eclipse model:** In this work, a simple cylindrical shadow model is adopted, and a logistic function is used to smooth its discontinuities. It may be interesting to consider the conical shadow model, as described in [23], which accounts for the penumbra and returns a continuous illumination function-provided that the numerical integrator samples the penumbral region adequately (otherwise the benefit over the cylindrical model would be negligible).
- **Perturbations:** The spacecraft is affected by various perturbations such as atmospheric drag, albedo radiation, third-body perturbations, and Earth's oblateness (J_2 effect). Including all of these simultaneously would significantly increase model complexity and could obscure the impact of each individual factor. Therefore, it is recommended adding perturbations incrementally, beginning with those of greatest influence. Since there is a high debris density in the 600-850 km altitude band [1], atmospheric drag has a considerable effect, as stated in [33], and should be included first. In particular, it significantly impacts solar sails, which present a large frontal area. Even if the sail is oriented edge-wise to the Sun to minimize solar radiation pressure, it remains exposed to drag. Because drag always opposes the velocity vector, it causes a reduction in semi-major axis and may help counteract the positive V-bar drift, though this effect must be verified.
- **Sail Model:** In this thesis the ideal solar-sail model is used because it is simpler and reduces complexity in the initial analysis phase. However, more complex models exist, such as the optical model, which accounts for the sail's reflection, absorption, and re-radiation, and the parametric model, which includes the effects of sail shape under load. Both models introduce additional complexity into trajectory analysis and optimization. Nevertheless, analysing perturbation effects like atmospheric drag should be prioritized over adopting a more complex sail model.

5.2.2 Optimization method

In this thesis work, direct collocation methods are used to solve the optimal control problem. Despite direct collocation's need for an initial guess, its selection is justified by its robust capability to handle complex trajectory-planning problems — especially those with non-linear and non-convex constraints such as keep-out regions and thrust limitations. This method discretizes the continuous trajectory into state and control variables at discrete time steps, representing the intervals between nodes with polynomial splines. By imposing constraints directly at collocation points, the algorithm ensures adherence across the entire trajectory, with accuracy improved by increasing the number of collocation points.

For future work, other optimization methods could be explored. Evolutionary algorithms and neurocontrollers like InTrance have been studied in [20]: they offer significant advantages by not requiring an initial guess and by being more likely to locate a global optimum; however, as Betts [38] points out, they are highly problem-dependent, employ randomized search heuristics without theoretical convergence proofs, and demand substantially more computational resources than direct collocation methods. Moreover, GPOPS-II proved capable of obtaining improved optimal solutions, as shown in Appendix A.4.2. In the appendix, the same optimization problem implemented in InTrance is reproduced using GPOPS-II, and the results are compared.

That is why convex programming [48] could be a promising option due to its deterministic convergence properties and its lack of requirement for an initial guess, making it highly suitable for real-time, autonomous on-board applications. It can efficiently achieve global optimal solutions and has been proven to offer robust performance. However, a significant challenge lies in the difficulty of convexifying non-convex constraints, such as those associated with KOZs.

5.2.3 Close-proximity operation study

To enhance the close-proximity study some recommendations for future work are:

- **Incorporate a angular-rate constraint** on the chaser's control, to ensure that the optimal controls obtained ensure a transition between successive attitude or orientations that adheres to a predefined maximum turning rate.
- **Constrain the resolution angle** Volpe et al. [49] define the resolution angle (Ψ) as the angle between the chaser's camera line of sight and the sunlight rays on the target, serving as a crucial index for relative illumination conditions and passive camera image quality. This angle is highly useful for optimization because, unlike the uncontrollable illumination angle, the resolution angle can be directly influenced by varying the chaser's trajectory. Minimizing its mean value (Ψ) directly enhances state-estimation accuracy, produces clearer images, and improves target-pose reconstruction — fundamental requirements for designing optimal docking trajectories with uncooperative satellites.
- **Explore transfer scenarios** in orbital configurations where the Sun does not lie in the orbital plane, such as a polar orbit (AA=0°), to test whether transfer trajectories flyable by a solar sail can be found that minimize both the δv and the relative position error δr.

5.2.4 Investigation of the next proximity phases

Future work should extend the analysis to the final rendezvous phase, i.e. study the trajectory to close and dock a dedicated target using a chaser module (separate from the solar sail) equipped with impulsive or low-thrust propulsion. In particular, the design and optimisation of this docking

trajectory should ensure the safe capture of an uncooperative space debris. To this end, the study should incorporate scenario-specific constraints such as line-of-sight requirements, KOZs, and attitude constraints to ensure both navigation accuracy and sensor visibility during the final approach.

Answering these questions will fill the remaining research gap of close-proximity operations and rendezvous of space debris using a solar sail.

Appendix A

Verification and Validation

This Appendix includes the verification and validation of the models used in this thesis work.

A.1 Clohessy-Wiltshire Frame

The reference frame and the equation of motion used in this study where validated through the following examples.

A.1.1 Coordinate transformation

To verify the coordinate transformation from the inertial frame to the co-moving/LVLH frame, example 7.2 from [31] is replicated.
In the example a space station (target) and a spacecraft have their initial states in the ECI frame (presented in Tab.A.1). The transformation matrix presented in Table A.2 is taken from Curtis.

Table A.1: Initial States in the Inertial ECI Frame

	X_I [km]	Y_I [km]	Z_I [km]	$\dot{X}_I$ [km/s]	$\dot{Y}_I$ [km/s]	$\dot{Z}_I$ [km/s]
Space station	1622.39	5305.10	3717.44	-7.2997	0.49236	2.48318
Spacecraft	1612.75	5310.19	3750.33	-7.3532	0.46386	2.46920

These results are compared with those obtained using the setup implemented in this study, and the percentage error between the two is reported.

Table A.2: Comparison between transformation matrices.

Element	Curtis	Own result	Error %
Q_{11}	0.242,945	0.242,946	4.12×10^{-4}
Q_{12}	0.794,415	0.794,415	0.00
Q_{13}	0.556,670	0.556,670	0.00
Q_{21}	−0.944,799	−0.944,798	1.06×10^{-4}
Q_{22}	0.063,725	0.063,725	0.00
Q_{23}	0.321,394	0.321,395	3.11×10^{-4}
Q_{31}	0.219,846	0.219,847	4.55×10^{-4}
Q_{32}	−0.604,023	−0.604,023	0.00
Q_{33}	0.766,044	0.766,044	0.00

A.1.2 Motion of the chaser relative to the target in LVLH frame

Clohessy Wiltshire equations are used to propagate a spacecraft within the co-moving frame/LVLH frame. The CW equations are implemented in MATLAB and verified using various examples from [31]. An example is shown in A.12, where example 7.3 has been replicated. It can be seen that the results obtained are the same as the reference.

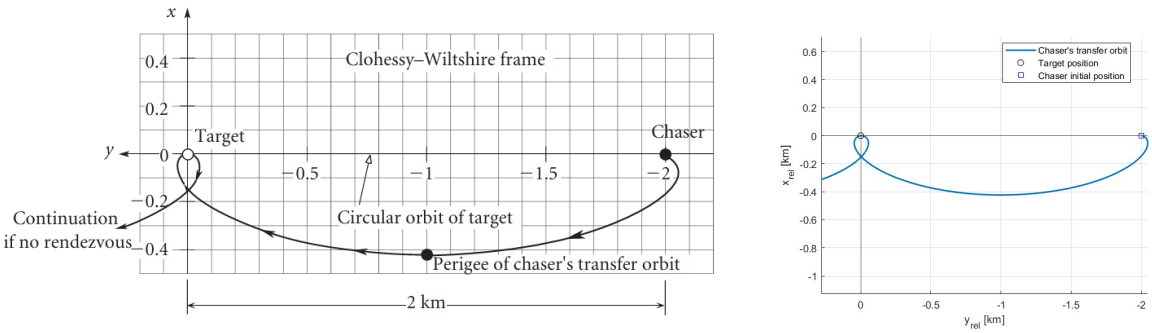

(a) **(b)**

Figure A.1: Comparing the propagation of an initial condition for results originating from (a) [31] and (b) this thesis work.

A.1.3 Accuracy assessment and step size selection for CW equations

The Clohessy–Wiltshire (CW) equations describe a simplified model of orbital relative motion, where the target is assumed to be in a circular orbit. These equations are a linearization of the two-body dynamics and therefore offer only an approximate solution [31]. This approximation introduces errors that become more significant as the spacecraft moves farther from the origin.

To evaluate the accuracy of the CW model, a baseline trajectory is computed using the RK45 ODE solver with a small time step of h = 0.05 s, propagating the state for four target revolutions.

The differences in position between the RK45 solution and the CW solution are then assessed for various step sizes of the CW propagator. The results are presented in Figure A.2.

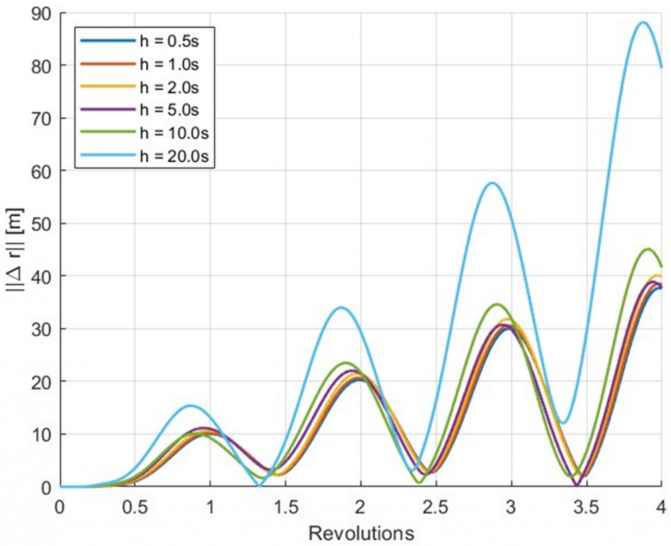

Figure A.2: Position difference between the 2-body and Clohessy-Wiltshire propagations over four orbital revolutions for different step sizes

As shown, increasing the step size leads to greater inaccuracies in the simulation. However, since high precision is not essential for the goals of this analysis, a step size of h= 10 s is chosen for all simulations. This choice balances computational efficiency with acceptable accuracy.

A.2 Shadow model

In this thesis, a cylindrical shadow model approximated using a smoothed logistic function is employed. To validate the model, several Keplerian orbits have been propagated with particular attention given to assessing whether the chosen coefficients (c_s and c_t) provided an accurate representation of the eclipse function.

Figure A.3 shows the resulting ECI trajectory, where the red segment represents the eclipsed portion. It can be observed that only the segments within Earth's cylindrical shadow are marked as eclipsed, demonstrating that the model correctly identifies shadow regions and has been implemented properly.

A direct comparison between the ideal eclipse model and the smoothed (logistic) version is shown in Figure A.4.

In the top figure of Fig. A.4, the two functions overlaps, while the bottom Figure A.4 illustrates the error between them. As expected, the greatest error occurs during the transitions in and out of eclipse, where the logistic function smooths the step change. Despite this, the overall deviation is small, and the approximation using $c_s = 298.78$ and $c_t = 1$ provides a reliable and accurate estimation of the eclipse status. A $c_t = 1$ is chosen to avoid any shift in the eclipse transition, while a $c_s = 298.78$ is selected, as computed in [32], to minimize the error the error between the logistic sunlight fraction and the discontinuous eclipse model for a circular LEO orbit.

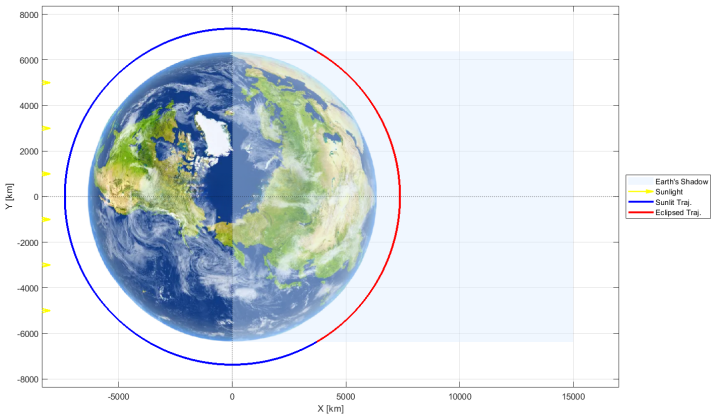

Figure A.3: Shadow model for a Keplerian Orbit

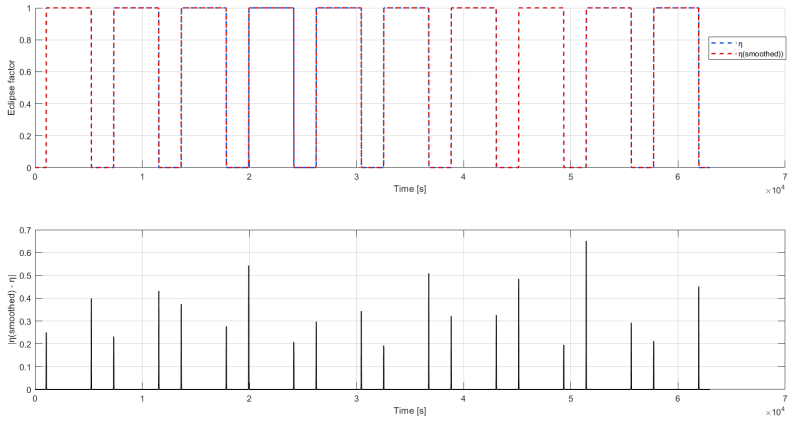

Figure A.4: In the top figure the eclipse factor using a ideal cylindrical shadow model and the smoothed is compared. In the bottom figure the error between the smoothed shadow model and the ideal one is shown.

The root-mean-square error (RMSE) between the two models is found to be approximately 0.022, confirming the validity of the smoothed approach for use in solar-sail dynamics and mission planning.

A.3 Dynamical model

To validate and verify the correct implementation of the solar-sail relative motion a test case is introduced. This test case is taken from reference [20] and the aim of this validation is to see if the CW equations are correctly implemented and allow to obtain the same propagation of the dynamics. It analyses the relative motion of a solar sail in proximity to a target object.

Based on the altitude where most debris are located [50] and the altitude at which ACS3 operate [15] the target is assumed to be in a circular, equatorial orbit with an altitude of 1000 km. At the start of the simulation, the sail and the target have identical initial state vectors,

placing the sail on the same orbit as the target at a true anomaly $\theta_0 = 0°$. A lightness number $\beta = 7.7e-3$ is used for the sail, consistent with the parameters of the ACS3 mission. The sail maintains a constant attitude throughout the simulation, which simplifies the analysis and isolates the effects of the parameters under study. The cone angle is set constant to $\alpha = 0°$. The sail's movement is simulated over ten revolutions of the target (17.5 hrs), with a time step of 10 s.

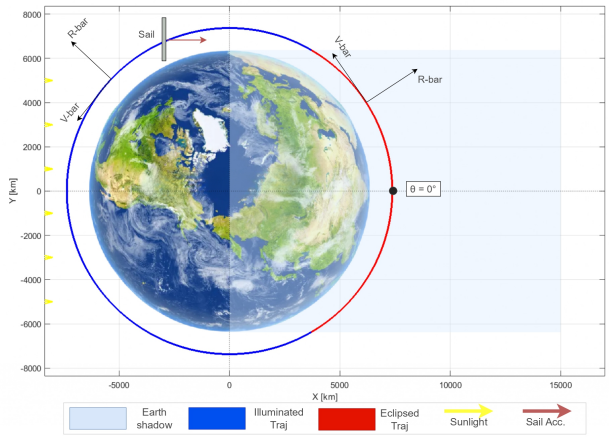

Figure A.5: Trajectory of the chaser for the test case in the ECI frame.

The solar sail, with its movement towards the Sun, causes the force of solar radiation pressure (SRP) to act in the opposite direction to its velocity. This initially reduces the sail's orbital velocity and energy relative to a target spacecraft, causing the sail to fall behind and descend into a more eccentric orbit with a lower periapsis. As the sail approaches periapsis, its orbital velocity increases again, allowing it to catch up with and overtake the target along the direction of the V-bar (i.e., in-track).

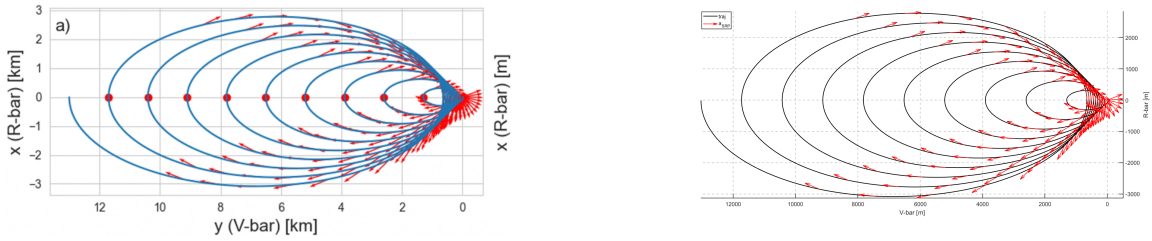

(a) **(b)**

Figure A.6: Comparing the propagation of the same initial state using CW equation from the test case shown in (a) [20] and (b) with the dynamical model used in this study.

Once the sail passes the perihelion, it has reached its maximum relative velocity. Moving away from the Sun, the SRP now has a component along its velocity vector, which increases the sail's orbital energy (see Fig.A.7) and pushes its aphelion above the target's altitude. As the sail climbs towards this higher apoapsis, its velocity drops below that of the target, causing a

relative drift in the positive direction of the R-bar and a slowdown in the positive movement of the V-bar. Just before crossing the target's orbit, the sail enters the Earth's shadow and enters the Earth's shadow and proceeds without SRP. At the moment of crossing its relative speed in the track (V-bar) is essentially zero, placing it directly in front of the target along the V-bar axis.

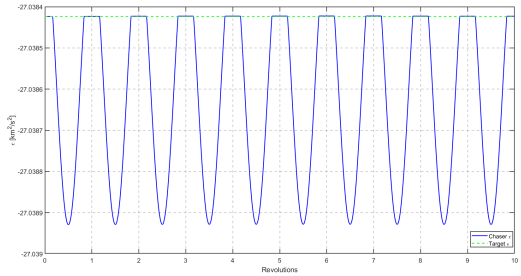

Figure A.7: Orbital energy of the chaser and the target.

During the first revolution, the sail remains at a lower radius than the target. After crossing the second revolution (now above the target), it moves slower than the target, causing a drift in the negative direction of the V-bar until it reaches its new apoapsis, where the relative velocity is at a minimum. Once past the apoapsis, the sail's speed increases again as it falls towards the periapsis, reducing its backward drift until it passes the target again (positive movement of the V-bar). During subsequent revolutions, the periapsis continues to descend and the apoapsis continues to rise, so the sail's orbit becomes increasingly eccentric.

A.4 Trajectory Optimization - GPOPS-II

This section presents the validation of GPOPS-II optimizer, used in this work. In order to verify and validate the optimizer two optimal control problems are considered. The first optimal control problem regards non-Keplerian orbit using a solar sail, the second problem is from ref. [20] about Encircling Hold Trajectories.

A.4.1 Non-Keplerian orbits

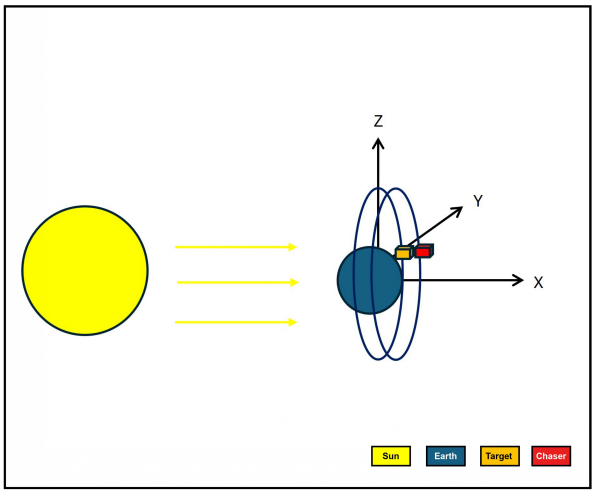

Figure A.8: Chaser and target orbits in ECI frame.

The objective of this study is maximize the time the sail orbit can keep a minimum deviation from a optimal non-Keplerian orbit. This non-Keplerian orbit maintains a constant offset, in the anti-sun direction (along $+X$ axis), relative to a target debris in a circular polar orbit around Earth. The primary dynamic force considered is solar radiation pressure, with additional adjustments for eclipse effects impacting the sail's operation. The target is at an altitude of r=20,539.66 km. The chaser (solar-sail) orbit is on a non-Keplerian polar orbit with radius ρ ($\rho = \sqrt{r^2 - z^2}$) with an off-set of 1 km from the target orbit.

To obtain the non- Keplerian orbit displaced in the anti-sun direction the two gravity components need to be considered are:

- $-(\mu/r^3) \cdot z$ along z direction: it is cancelled with the solar radiation pressure

$$a_{gz} = -\frac{\mu}{r^3} \cdot z \quad \Longrightarrow \quad a_{gz} = a_{5RP,z}$$

$$a_{SRP,z} = 4.6 \times 10^{-5}\,\mathrm{m/s^2} \quad \Longrightarrow$$

$$r = 20539663.04\,m$$

The chosen displacement is of z = 1000 m. The value is "small" since CW equations are used as dynamical model and require a small relative distance between the chaser and the target to be accurate.

$\omega = \tilde{\omega}$ results from selecting the first family of non-Keplerian orbits so that the chaser's period ω is synchronous with a Keplerian target orbit with $\tilde{\omega}$, radius r and z=0. Under this

condition, the required pitch (cone) angle is obtained as:

$$\tan\alpha = \frac{\rho}{z}\left[1 - \left(\frac{\omega}{\tilde{\omega}}\right)^2\right] \quad \Longrightarrow \quad \alpha = 0^\circ \tag{A.1}$$

- $-(\mu/r^3)\cdot y$ along y direction: this component is responsible for the circular motion of the chaser orbit (radius ρ) but with angular velocity $\sqrt{(\mu/r^3)}$.

The optimization leverages GPOPS-II to refine an initial trajectory that slightly deviates from the non-Keplerian path. The problem is set to direct the optimization from this initial guess towards the predefined trajectory, utilizing known control profiles essential for maintaining the required orbit offset.

Therefore, imposing the following initial relative position of the solar sail:

$$X_0 = [0; -(r-\rho); z; 0; 0; 0]$$

.

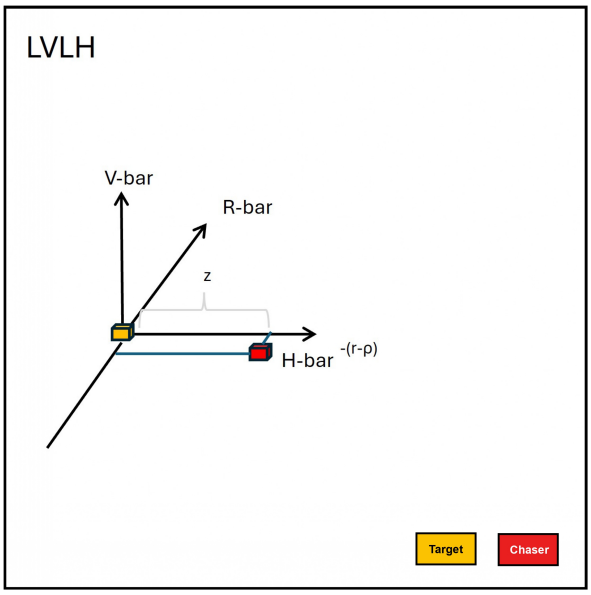

Figure A.9: Chaser trajectory in the co-moving (LVLH) frame.

Optimization problem

The optimization setup on GPOPS-II is the following. The objective of this formulation is to maximize the duration t_f during which the solar sail (chaser) remains within a prescribed tolerance of the non-Keplerian orbit. Control is achieved using the sail's cone and clock angles $\alpha(t)$ and $\delta(t)$. The dynamic is modelled by the linearized Hill–Clohessy–Wiltshire equations with SRP. Large bounds are placed on the state variables (position and velocity) to allow freedom of motion, while tight path constraints enforce that the state may only deviate by a small tolerance tol from the desired state throughout the interval $[t_0, t_f]$.

$$\min_{\alpha(t),\,\delta(t)} \; J(\alpha,\delta) = -t_f$$

controls: $\alpha(t),\ \delta(t)$ (cone & clock angles)

Dynamics

$\ddot{x} - 2n\dot{y} - 3n^2x = u_x$ (HCW with SRP)

$\ddot{y} + 2n\dot{x} = u_y$

$\ddot{z} + n^2 z = u_z$

$t_0 = 0, \quad t_f \in [t_{f,\min},\, t_{f,\max}]$ (Time bounds)

State bounds

$x, y, z \in [-10^6,\, 10^6]$ m

$v_x, v_y, v_z \in [-10^6,\, 10^6]$ m/s

$\alpha(t) \in \left[-\frac{\pi}{2}, \frac{\pi}{2}\right],\ \delta(t) \in [-\pi, \pi]$ (Control bounds)

Path constraint

$x(t) = 0 + / - \text{tol}$

$y(t) = -(R_{\text{target}} - \rho), \quad z(t) = z_0$

$v_x(t) = v_y(t) = v_z(t) = 0 + / - \text{tol}$

Initial and final state

$\mathbf{x}_0 = [0,\ -573159.09,\ 10^6,\ 12925.59,\ 0,\ 0]$

For the initial guess of controls, control angles are set to produce no thrust, i.e., $\alpha = 90°$, $\delta = 0$. The initial state guess is generated by forward propagating for 1 period of the target orbit, with constant controls. The initial state is evaluated as: $X_0 = [0; -(r - \rho); z; 0; 0; 0]$.
The final time t_f is set to 10 target revolutions. This complete setup is used as input for GPOPS-II, enabling high-fidelity time-optimal trajectory optimization under solar-sail propulsion in a non-Keplerian configuration.

Results

From Figures A.10 and A.11 in output from optimization it results that GPOPS-II "finds" the optimal required pitch angle to have a non-Keplerian displaced orbit: $\alpha = 0°$. The resulting trajectory of the solar sail relative to the target is a "dot".

We conclude that the GPOPS-II optimization is successfully verified and validated for the presented user configuration. To further validate this analysis (see Fig. A.12), control history plots are generated for initial cone angles other than $\alpha = 90°$, specifically examining cases with $\alpha = 70°$ and $\alpha = 45°$. In all scenarios, the optimizer consistently converges to $\alpha = 0°$, the expected optimal cone angle. This demonstrates robust performance across varied initial conditions.

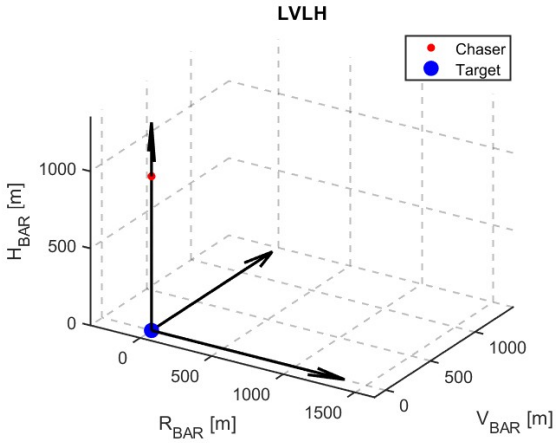

Figure A.10: Non-Keplerian trajectory result output from GPOPS-II.

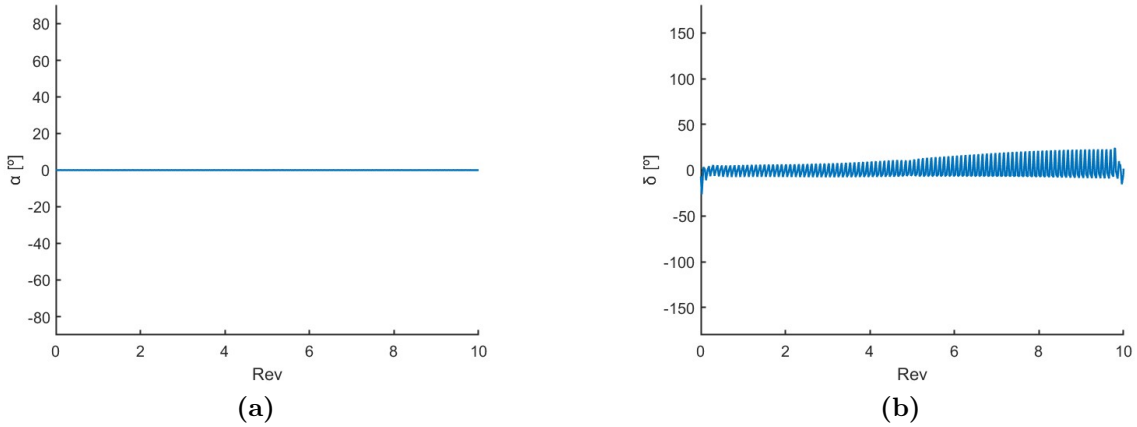

(a) **(b)**

Figure A.11: Cone angle (a) and clock angle (b) from GPOPS-II output.

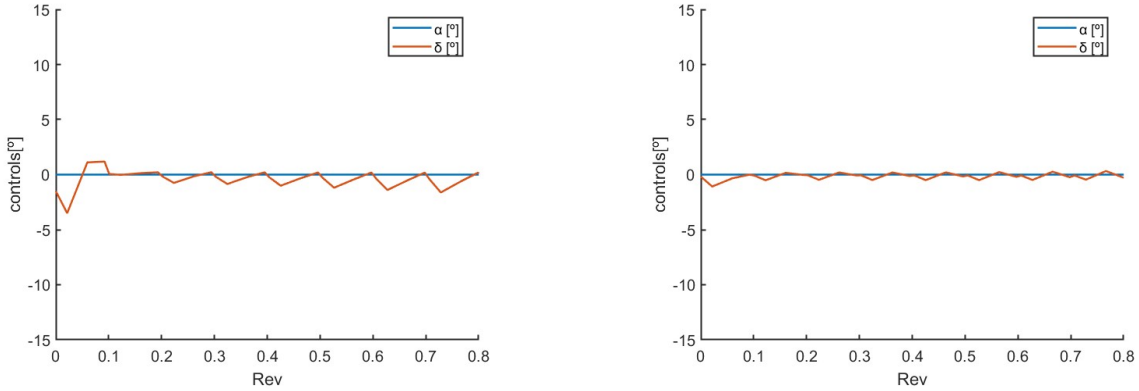

(a) **(b)**

Figure A.12: Non-Keplerian results with initial guessed cone angles of 70° (a) and 45° (b).

A.4.2 Hold Trajectories (Encircling case)

To further verify and validate GPOPS-II user setup the Encircling Hold Trajectories analysis done by [20] is replicated. The analysis of the hold trajectory investigates the impact of the sail's operational constraints, specifically cone angle limitations. A parametric analysis is conducted varying the size of the hold volumes (KOZ) and the maximum allowable cone angle constraint. Four sizes of hold volumes are used for the analysis. The dimensions of the outer and inner ellipsoids defining each holding area, along with the initial conditions of the sail, are provided in Table A.3. The semi-major and minor axes of the inner ellipsoid are set to 97% of those of the outer ellipsoid. This ratio has been empirically chosen to allow easy comparison of hold trajectories under different operational constraints. The initial Keplerian elliptical orbit, which lies within the hold volume, is positioned midway between the two ellipsoids.

	Outer Ellipsoid		Inner Ellipsoid		sail	
Case	Semi-Major	Semi-Minor	Semi-Major	Semi-Minor	x_0	v_{y0}
1	4000	2000	3880	1940	−1968.794	3.929
2	2000	1000	1940	970	−984.766	1.965
3	1500	750	1455	727.5	−738.574	1.474
4	1000	500	970	485	−495.331	0.988

Table A.3: Geometric parameters and sail settings for each case.

The optimization problem aims to maximize the time the trajectory remains within the defined hold volumes, namely the outer and inner ellipsoids. The maximum hold time is set to 10 target revolutions, corresponding to approximately 17.5 hours. The optimization setup is formulated as follows:

$$\min_{u(t)} -t_f$$

with a_i, b_i, c_i semi-axes of the inner ellipsoid.

a_o, b_o, c_o semi-axes of the outer ellipsoid.

subject to:

$$\ddot{x} - 2n\dot{y} - 3n^2 x = u_x \qquad \text{(State dynamics)}$$

$$\ddot{y} + 2n\dot{x} = u_y$$

$$\ddot{z} + n^2 z = u_z$$

$$x(0) \in [x_{\min}, x_{\max}] \qquad \text{(Initial state)}$$

$$x_{\min} = [-10^4, -10^4, -10^4, -100, -100, -100] \qquad \text{(State lower bounds)}$$

$$x_{\max} = [10^4, 10^4, 10^4, 100, 100, 100] \qquad \text{(State upper bounds)}$$

$$\left(\frac{x}{a_o}\right)^2 + \left(\frac{y}{b_o}\right)^2 + \left(\frac{z}{c_o}\right)^2 \leq 1 \qquad \text{(Outer KOE)}$$

$$\left(\frac{x}{a_i}\right)^2 + \left(\frac{y}{b_i}\right)^2 + \left(\frac{z}{c_i}\right)^2 \geq 1 \qquad \text{(Inner KOE)}$$

$$\|u(t)\| \in [0, 1] \qquad \text{(Control path constraint)}$$

$$[0, -1, -1]^T \leq u(t) \leq [1, 1, 1]^T \qquad \text{(Control bounds)}$$

$$t_f \in [t_0, t_{f_{\max}}] \qquad \text{(Time bounds)}$$

Results

The results obtained using `GPOPS-II` are more favourable compared to those reported in [20], which were obtained using `InTrance`, especially for lower maximum cone angle values (65° and 60°). As shown in Table A.4 (where the results from [20] are reported in brackets), for lower cone angle constraints ($\alpha_{\max} = 60°$ and 65°), the number of revolutions during which the sail remains within the hold volume reaches the maximum allowed, that is 10 target revolutions. For example, in Case 1 with $\alpha_{\max} = 60°$, the hold trajectory remains within the hold volume for 10 target revolutions, whereas [20] reports 8.79 revolutions.

Case	$\alpha_{\max}$ [°]					
	60	65	70	75	80	85
1	10 (8.79)	10	10	10	10	10
2	10 (4.87)	10 (8.43)	10	10	10	10
3	10 (3.99)	10 (7.12)	10	10	10	10
4	10 (2.64)	10 (5.95)	10	10	10	10

Table A.4: Maximum allowable cone angle $\alpha_{\max}$ for each case.

A likely reason for this discrepancy lies in the different optimization strategies. The results in [20] were obtained using `InTrance`, an optimizer that does not require an initial guess for the steering strategy, but only the sail's initial state. In contrast, in `GPOPS-II`, the optimal solution for each case is found progressively: starting from a relaxed constraint of $\alpha_{\max} = 85°$, the resulting solution is then used as the initial guess for the next tighter constraint (e.g., 80°), and so on, down to 60°.

Figure A.13 shows the optimized trajectory for Case 4 with $\alpha_{\max} = 60°$. The plot also includes the forward propagation of the trajectory using the computed optimal control, showing that the propagated trajectory perfectly matches the state profile found by `GPOPS-II`.

It is also clear that the trajectory is not planar but has an offset in the H-bar direction.

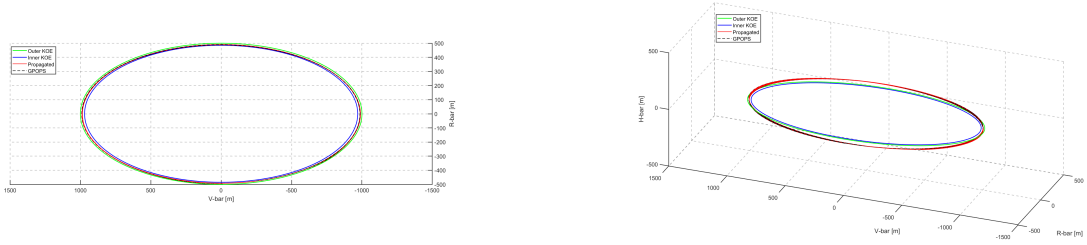

(a) **(b)**

Figure A.13: Optimal trajectory for Case 4 with $\alpha_{\max} = 60°$: planar (a) and 3D (b) views.

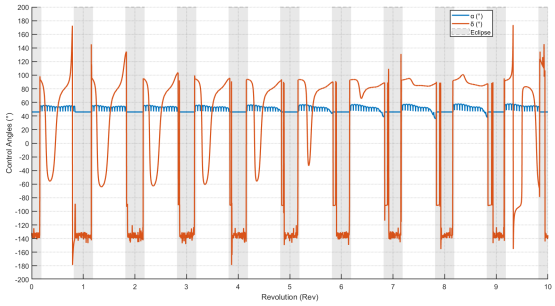

Figure A.14: Control profile of Case 4 with $\alpha_{max} = 60$ °.

A.5 Output Solution of Optimization

In this section, the results obtained from the optimisation problems discussed in Section 3 are validated by forward propagation. The initial state obtained through the optimisation process is then propagated using the control obtained from GPOPS-II output. Only a subset of the forward-propagated solutions from Chapter 3 is shown, since a similar trend is observed for the other cases. It is essential to ensure the physical validity of the results obtained. Direct collocation methods require that the optimal solution satisfies the optimality condition only at the intermediate points (collocation points), where the constraint on dynamics is imposed. In the interval between these points, it is necessary to further assess by forward propagation that the results obtained do not violate the constraints.

Hold Trajectory propagation

To validate the results obtained in Section 3.1, the initial state from the optimization is forward propagated in time using the optimal computed control. Figure A.15a shows that the forward propagation of the initial state from case $\alpha_{\max} = 85°$ with its optimal control exactly overlaps the state trajectory returned by GPOPS-II.

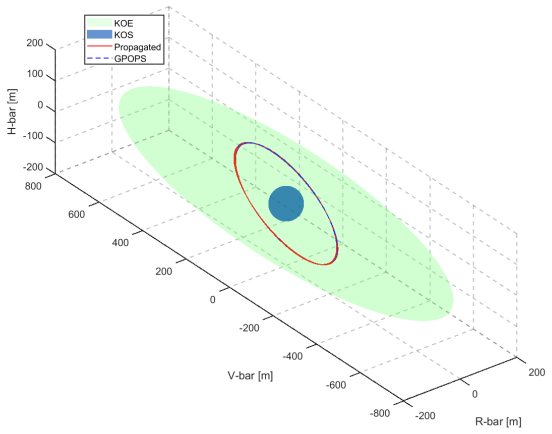

(a) 3D trajectory: GPOPS-II (dashed blue) vs. propagated (solid red).

Figure A.15: Hold Trajectory case (a): GPOPS-II output state vector compared with the analytical solution obtained by forward propagation. Components continued in Fig. A.16.

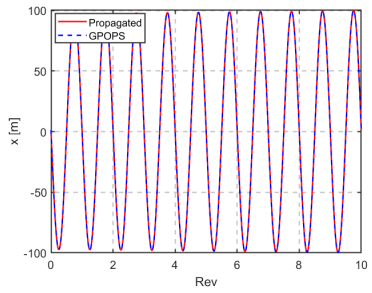

(a) Component x.

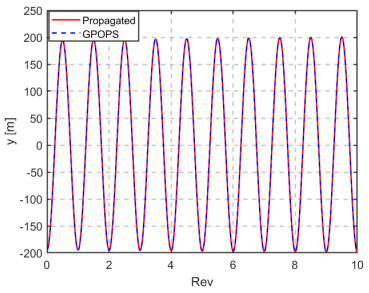

(b) Component y.

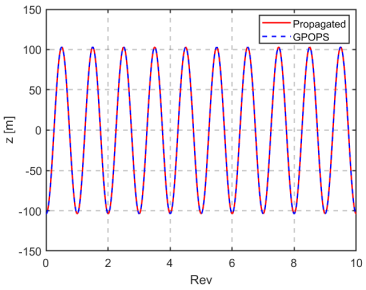

(c) Component z.

Figure A.16: Hold Trajectory case (b-d): Cartesian components of the GPOPS-II state vector compared with the propagated trajectory. Continuation of Fig. A.15.

Inspection Loop propagation

Figure A.17a shows the forward propagation of the initial state for IL Case 1 using the optimal control from GPOPS-II. A complete discussion of this results can be found in Section 3.2. In Fig. A.18a-A.18c the plots of the three state components x, y, and z are displayed. The propagated trajectory overlaps the GPOPS-II solution almost exactly for up to ten revolutions; however, the final propagated state does not exactly match the GPOPS-II trajectory (dashed blue line). This discrepancy is likely due to the interpolation of the control profile output by GPOPS-II. Employing a finer interpolation scheme should improve the accuracy of the forward propagation.

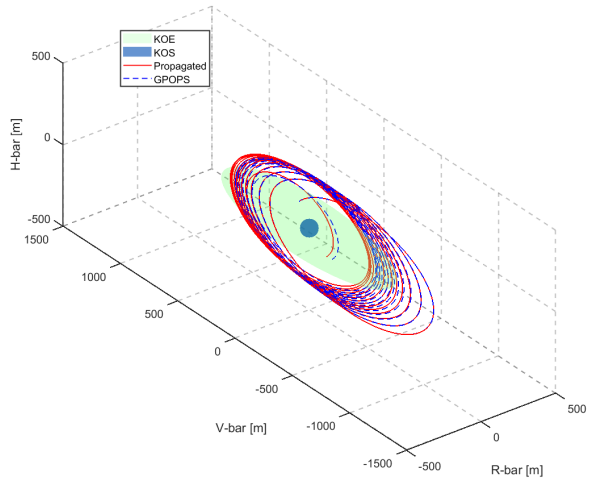

(a) 3D trajectory: GPOPS-II (dashed blue) vs. propagated (solid red).

Figure A.17: Inspection-loop case (a): GPOPS-II output state vector compared with the analytical solution obtained by forward propagation. Components continued in Fig. A.18.

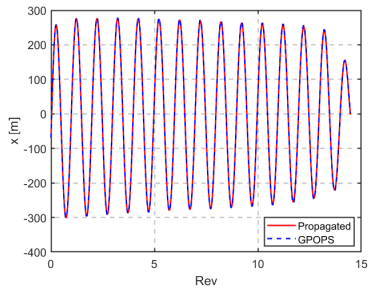

(a) Component x.

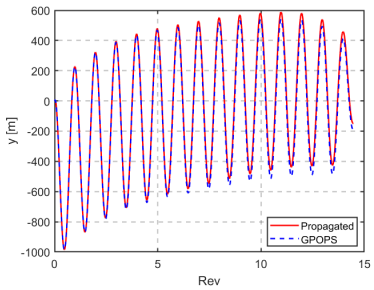

(b) Component y.

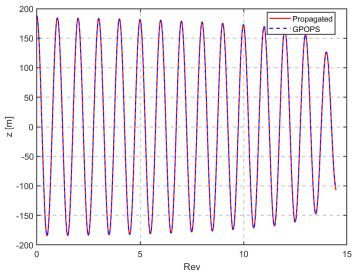

(c) Component z.

Figure A.18: Inspection-loop case (b-d): Cartesian components of the GPOPS-II state vector compared with the propagated trajectory. Continuation of Fig. A.17.

Transfer propagation

Figure A.19a shows Transfer 4 from Section 3.3, forward propagated to verify whether the resulting state coincides with the GPOPS-II output. It can be seen that the propagated state almost exactly matches the GPOPS-II trajectory, confirming the accuracy of the optimal control.

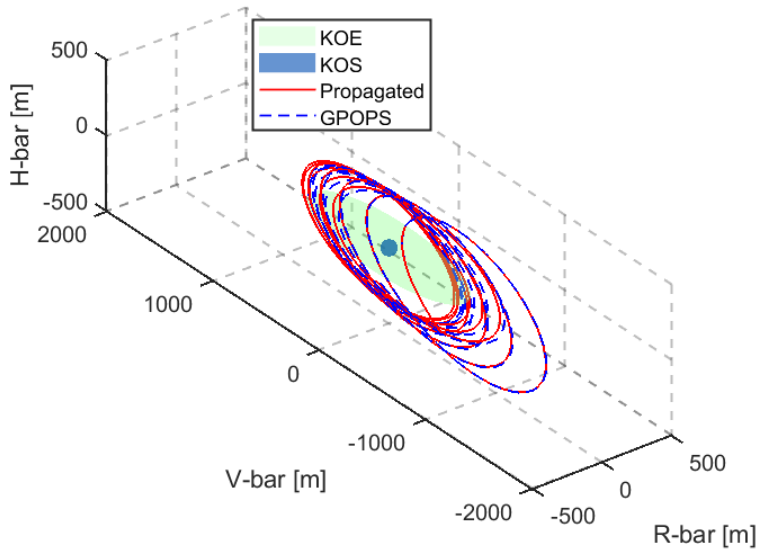

(a) 3D trajectory: GPOPS-II (dashed blue) vs. propagated (solid red).

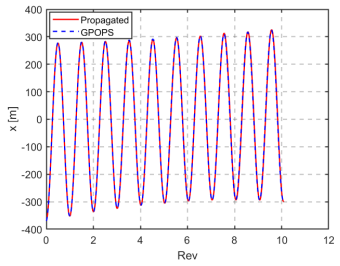

(b) Component x.

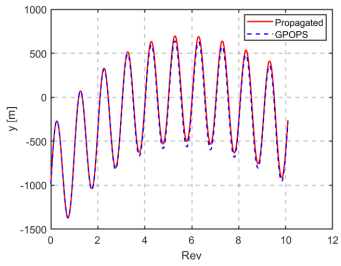

(c) Component y.

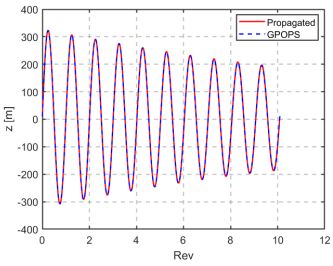

(d) Component z.

Figure A.19: Transfer case: GPOPS-II output state vector compared with the analytical solution obtained by forward propagation.

Appendix B

GPOPS-II

This appendix provides a sensitivity analysis conducted on the problem discussed in A.4.2 and the configuration used in GPOPS-II for the result section.

B.1 Sensitivity Analysis

This sensitivity analysis is performed on A.4.2 to tune mesh fraction, tolerance and collocation points range. The selection of values for mesh fraction, collocation points, and tolerance in the sensitivity analysis is based both on prior examples provided in the GPOPS-II User Guide [41] and on practical experience gained from the optimization problems discussed in Chapters 3 and 4. A total of 324 cases are analysed.

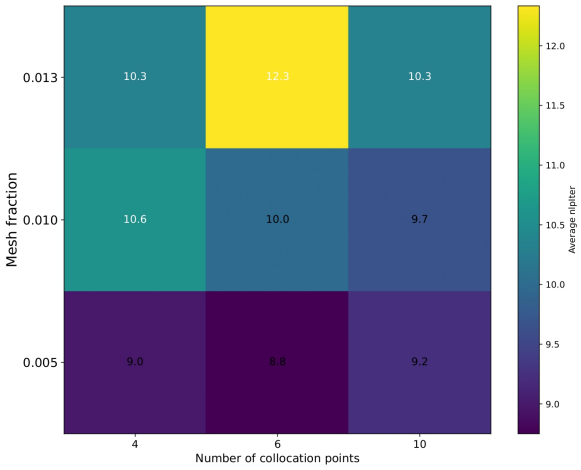

Figure B.1: Sensitivity analysis on problem Hold trajectory (Encircling) with maximum cone angles of 85°, 80°, and 70°. In the Heatmap NLP iterations, mesh fraction and collocation points number are compared.

The mesh fraction value of 0.013 corresponds to 80 mesh segments into which the initial guess state is divided, so 0.010 corresponds to 100 mesh segments and 0.005 to 200 mesh segments. A fine mesh fraction is used, which helps reduce the number of iterations needed for convergence. This statement is true because the problem is given a good initial guesses.

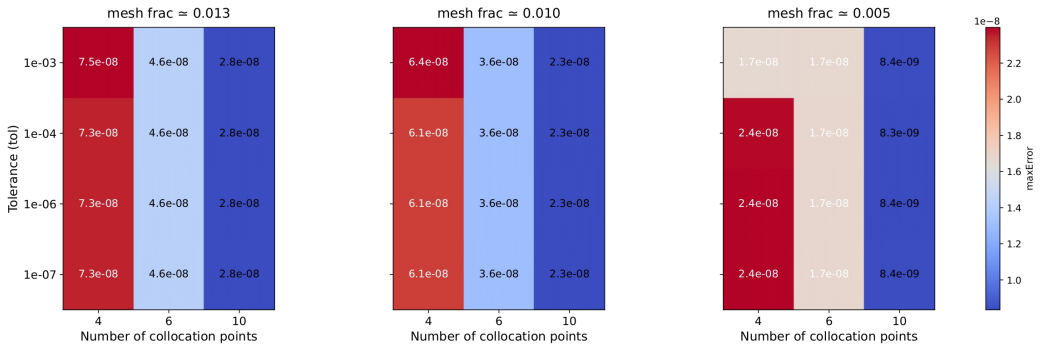

(a)

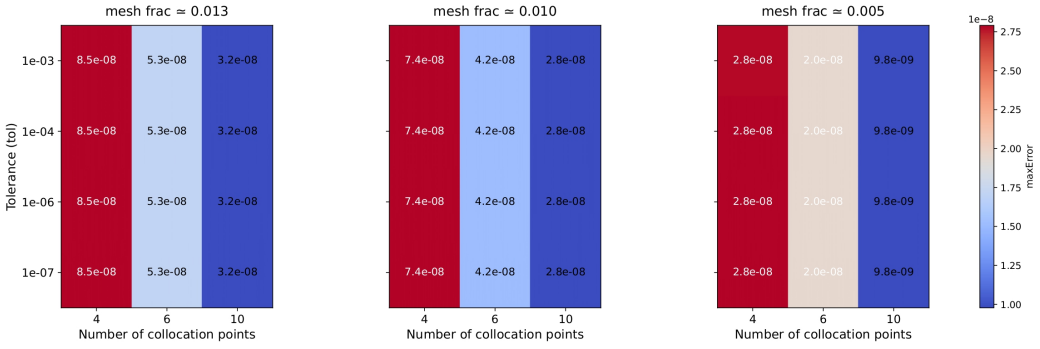

(b)

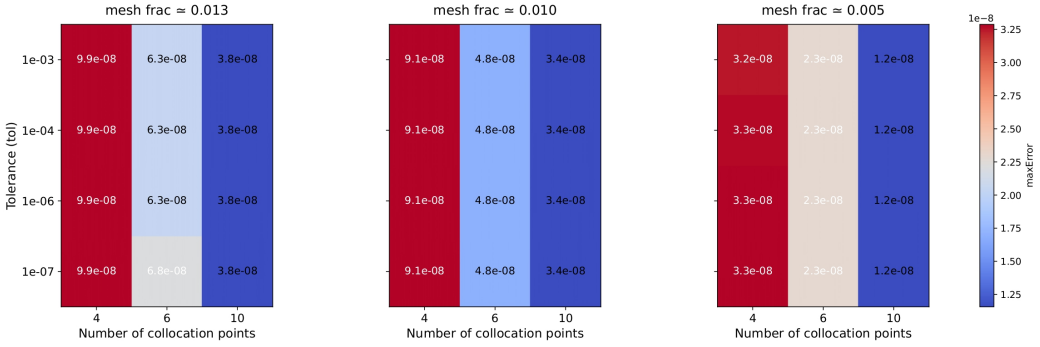

(c)

Figure B.2: Sensitivity analysis on problem Hold trajectory (Encircling) with maximum cone angles of 85° (a), 80° (b), and 70° (c). In the Heatmaps tolerance, mesh fraction and collocation points number are compared.

A number of collocation point of 6 and mesh fraction of 0.05 has the lower NLP iteration before convergence. Figure B.2c illustrates how the tolerance (or error) of the output varies as a function of the mesh fraction and the number of collocation points, for a Hold-Trajectory case with cone angle constrained to 70°. As the mesh fraction decreases from 0.013 to 0.005, the error decreases steadily, indicating that finer meshes significantly improve accuracy. Similarly, increasing the number of collocation points from 4 to 6 and then to 10 results in progressively

lower errors, although the rate of improvement decreases, especially with lower mesh fractions. For example, with a mesh fraction of 0.005, the error improves from approximately 3.3e-08 to 1.2e-08 across the collocation range. Overall, the graph confirms that finer meshes and a greater number of positioning points improve the accuracy of the solution.

B.2 GPOPS-II Setup and Numerical Values

B.3 Hold Trajectory

To compute the hold-trajectory problem in GPOPS-II, the mesh and solver options are selected to balance accuracy and computational effort. Table B.1 summarizes the mesh settings (e.g., collocation method, number and length of mesh intervals, tolerance) and IPOPT solver parameters (linear solver, convergence tolerances, maximum iterations, derivative settings). The tolerance values are based on the sensitivity analysis in Section B.1 and examples from the GPOPS-II user guide.

Table B.2 then lists the numerical bounds on the state and control variables. The "Initial state" block constrains the starting position and velocity; "State" applies across the trajectory; "Final state" fixes the terminal limits; and "Control bounds" enforce actuator limits. All values are given in unscaled units and must be adjusted according to the user-defined scaling.

Mesh settings	
`mesh.method`	hp-LiuRao-Legendre
`mesh.tolerance`	1×10^{-6}
`mesh.maxiterations`	4
`mesh.colpointsmax`	20
`mesh.colpointsmin`	10
N =`length(guess.fraction)`	M(mesh intervals)=200[1]
`mesh.phase.colpoints`	10
`mesh.phase.fraction`	`guess.fraction`
Solver settings	
`setup.displaylevel`	2
`setup.nlp.solver`	`'ipopt'`
`setup.nlp.ipoptoptions.linear_solver`	`'ma57'`
`setup.nlp.ipoptoptions.tolerance`	1×10^{-7}
`setup.nlp.ipoptoptions.maxiterations`	1000
`setup.auxdata`	`auxdata`
`setup.bounds`	`bounds`
`setup.guess`	`guess`
`setup.derivatives.supplier`	`'sparseFD'`
`setup.derivatives.derivativelevel`	`'second'`
`setup.mesh`	`mesh`

Table B.1: GPOPS-II optimizer setup (IPOPT options setup)

Variabile	Lower bound	Upper bound
Initial state		
x_0	-160	160
y_0	$-2x_0$	0
z_0	-160	160
$v_{x,0}$	-100	100
$v_{y,0}$	-100	100
$v_{z,0}$	-100	100
State		
x	-160	160
y	$-2x_0$	$2x_0$
z	-160	160
v_x	-100	100
v_y	-100	100
v_z	-100	100
Final state		
x_f	-160	160
y_f	$-2x_0$	$2x_0$
z_f	-160	160
$v_{x,f}$	-100	100
$v_{y,f}$	-100	100
$v_{z,f}$	-100	100
t_f	0	$10\,T_t$
Control bounds		
u_1	0.08716	1
u_2	-1	1
u_3	-1	1

Table B.2: GPOPS-II Set up. Numerical values here listed have to be scaled, according to user defined scaling.

B.4 Inspection Loop

Table B.5 summarizes the mesh configuration for the Inspection Loop scenario. The mesh settings differ from those used in the Hold Trajectory case, while the IPOPT options remain the same to enable GPOPS-II to iteratively refine the discretization. In this setup, the number of collocation points per interval is allowed to vary between 6 and 20, ensuring that the solver adapts the mesh

[1]In GPOPS-II the initial guess is provided via a user-defined function: this function propagates the system dynamics from the initial time t_0 to t_f over M segments, then constructs: `guess.time` (a strictly increasing time vector), `guess.state`, `guess.control`, and finally computes `guess.phase.fraction`.

until the optimal solution is reached (see Section 2.5.2 for the optimization problem formulation).

Table B.4 defines the bounds for this problem. The "Objective weights" block sets the trade-off parameters in the cost function, which in principle describe a full Pareto front; however, since the primary goals are to maximize observation time and loop duration, only those weight combinations emphasizing these objectives are analysed, as shown in Fig. B.3.

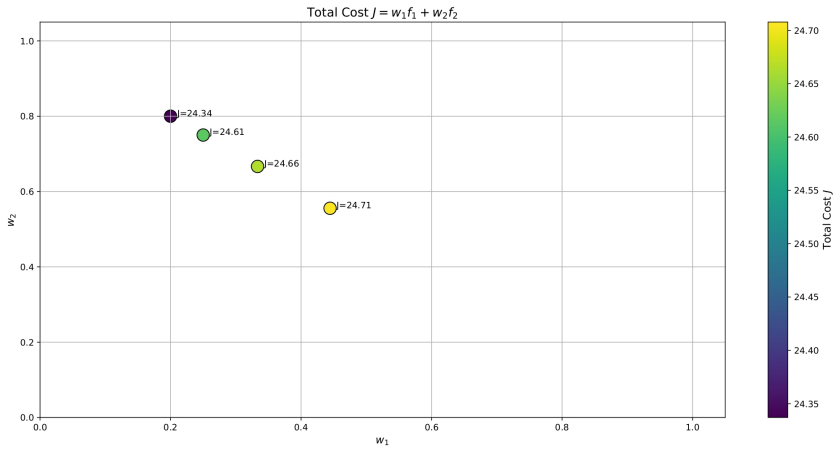

Figure B.3: Total cost $J = w_1 f_1 + w_2 f_2$ evaluated at selected weight pairs (w_1, w_2), illustrating how J varies along the sampled Pareto front.

The "Final time" block constrains the IL duration; "Initial state," "State," and "Final state" enforce position and velocity bounds; "Control bounds" restrict the inputs; and the "Event-group constraints" impose tightening tolerances on relative position and velocity so that the final Inspection Loop state matches the target SE state.

[2] `tol_pairs` = [10,0.10]; [10,0.05]; [10,0.02]; [10,0.01]; [5,0.02]; [1,0.02]; [5,0.01]; [1,0.01]
1) tighten both ($\Delta r = 10, \Delta v = 0.10$); 2) tighten Δv only ($\Delta r = 10, \Delta v = 0.05$); ... 8) ($\Delta r = 1, \Delta v = 0.01$).

Mesh settings	
`mesh.method`	hp-LiuRao-Legendre
`mesh.tolerance`	1×10^{-5}
`mesh.maxiterations`	4
`mesh.colpointsmax`	20
`mesh.colpointsmin`	6
$N =$`length(guess.fraction)`	M(mesh intervals)=100
`mesh.phase.colpoints`	6
`mesh.phase.fraction`	`guess.fraction`
Solver settings	
`setup.displaylevel`	2
`setup.nlp.solver`	`'ipopt'`
`setup.nlp.ipoptoptions.linear_solver`	`'ma57'`
`setup.nlp.ipoptoptions.tolerance`	1×10^{-7}
`setup.nlp.ipoptoptions.maxiterations`	1000
`setup.auxdata`	`auxdata`
`setup.bounds`	`bounds`
`setup.guess`	`guess`
`setup.derivatives.supplier`	`'sparseFD'`
`setup.derivatives.derivativelevel`	`'second'`
`setup.mesh`	`mesh`

Table B.3: GPOPS-II optimizer setup (IPOPT options setup)

Variabile	Lower bound	Upper bound
Objective weights		
w_1	$\frac{1}{3}$	–
w_2	$\frac{2}{3}$	–
Final time		
t_f	$5\,T_t$	$20\,T_t$
Initial state		
x_0	-400	400
y_0	-1000	0
z_0	-400	400
$v_{x,0}$	-100	100
$v_{y,0}$	-100	100
$v_{z,0}$	-100	100
State		
x	-10^6	10^6
y	-10^6	10^6
z	-10^6	10^6
v_x	-100	100
v_y	-100	100
v_z	-100	100
Final state		
x_f	$x_{\min}$	$x_{\max}$
y_f	$y_{\min}$	$y_{\max}$
z_f	$z_{\min}$	$z_{\max}$
$v_{x,f}$	-100	100
$v_{y,f}$	-100	100
$v_{z,f}$	-100	100
Control bounds		
α	0.0872	1
δ_1	-1	1
δ_2	-1	1
Event-group constraints[2]		
$\Delta r_x, \Delta r_y, \Delta r_z$	$-\,\mathrm{tol}_r$	tol_r
$\Delta v_x, \Delta v_y, \Delta v_z$	$-\,\mathrm{tol}_v$	tol_v

Table B.4: GPOPS-II Set up. Numerical values here listed have to be scaled, according to user defined scaling.

B.5 Transfer

For the transfer problem, a mesh settings similar to those used in the Inspection Loop (Table B.5) is employed, with four collocation points per interval and the same solver tolerances.

Table B.6 summarizes the bounds and constraints for the transfer scenario, including objective-weight parameters, control limits, time windows, state bounds during transfer, final-state tolerances (which vary by tolerance set), and initial-guess bounds. All values are given in scaled units and must be adjusted according to the user's scaling definitions.

Mesh settings	
`mesh.method`	hp-LiuRao-Legendre
`mesh.tolerance`	1×10^{-5}
`mesh.maxiterations`	4
`mesh.colpointsmax`	20
`mesh.colpointsmin`	4
N =`length(guess.fraction)`	M(mesh intervals)=100
`mesh.phase.colpoints`	4
`mesh.phase.fraction`	`guess.fraction`
Solver settings	
`setup.displaylevel`	2
`setup.nlp.solver`	`'ipopt'`
`setup.nlp.ipoptoptions.linear_solver`	`'ma57'`
`setup.nlp.ipoptoptions.tolerance`	1×10^{-7}
`setup.nlp.ipoptoptions.maxiterations`	1000
`setup.auxdata`	`auxdata`
`setup.bounds`	`bounds`
`setup.guess`	`guess`
`setup.derivatives.supplier`	`'sparseFD'`
`setup.derivatives.derivativelevel`	`'second'`
`setup.mesh`	`mesh`

Table B.5: GPOPS-II optimizer setup (IPOPT options setup)

[3]Tolerance sets are used depending on the target's velocity magnitude: Position tolerances $\text{tol}_{x,y} = 5$ or 10 m, $\text{tol}_z = 1$ or 0.5 m; Velocity tolerances $\text{tol}_{vx} = 0.01$ or 0.001 m/s, $\text{tol}_{vy}, \text{tol}_{vz} = 0.1$ or 0.05 m/s.These tolerance are not varied trough the optimization, since the minimization of the tolerance is done in the objective function.

[4]`tol_sets` rows are $[\text{tol}_x, \text{tol}_y, \text{tol}_z, \text{tol}_{vx}, \text{tol}_{vy}, \text{tol}_{vz}]$: 1) [10,10,1,1,1,1]; 2) [10,10,1,0.1,0.1,0.1]; 3) [10,10,1,0.05,0.1,0.1]; 4) [10,10,1,0.01,0.1,0.1]; 5) [10,10,1,0.01,0.05,0.05]; 6) [5,5,1,0.01,0.05,0.05]; 7) [5,5,1,0.01,0.01,0.01]; 8) [5,5,1,0.005,0.01,0.01].

Variable	Lower bound	Upper bound
Objective weights		
w_1	$\frac{1}{3}$	–
w_2	$\frac{2}{3}$	–
Control bounds		
u_1	0	1
u_2	-1	1
u_3	-1	1
Time bounds (Cases 1–3)		
t_0	t_0	t_0
t_f	$0.8\,T_t$	$1.5\,T_t$
Time bounds (Case 4)		
t_0	t_0	t_0
t_f	$10\,T_t$	$12\,T_t$
State bounds		
x	-10^6	10^6
y	-10^6	10^6
z	-10^6	10^6
v_x	-100	100
v_y	-100	100
v_z	-100	100
Final-state bounds[3]		
x_f	$x_T - \mathrm{tol}_x$	$x_T + \mathrm{tol}_x$
y_f	$y_T - \mathrm{tol}_y$	$y_T + \mathrm{tol}_y$
z_f	$z_T - \mathrm{tol}_z$	$z_T + \mathrm{tol}_z$
$v_{x,f}$	$v_{x,T} - \mathrm{tol}_{vx}$	$v_{x,T} + \mathrm{tol}_{vx}$
$v_{y,f}$	$v_{y,T} - \mathrm{tol}_{vy}$	$v_{y,T} + \mathrm{tol}_{vy}$
$v_{z,f}$	$v_{z,T} - \mathrm{tol}_{vz}$	$v_{z,T} + \mathrm{tol}_{vz}$
Initial-state guess bounds[4]		
x_0	$x_0 - \mathrm{tol}_x$	$x_0 + \mathrm{tol}_x$
y_0	$y_0 - \mathrm{tol}_y$	$y_0 + \mathrm{tol}_y$
z_0	$z_0 - \mathrm{tol}_z$	$z_0 + \mathrm{tol}_z$
$v_{x,0}$	$v_{x,0} - \mathrm{tol}_{vx}$	$v_{x,0} + \mathrm{tol}_{vx}$
$v_{y,0}$	$v_{y,0} - \mathrm{tol}_{vy}$	$v_{y,0} + \mathrm{tol}_{vy}$
$v_{z,0}$	$v_{z,0} - \mathrm{tol}_{vz}$	$v_{z,0} + \mathrm{tol}_{vz}$

Table B.6: Transfer problem: bounds and initial-guess numerical values. All the variables are scaled with a user-setup scaling.

Appendix C

Additional Figures and Tables

Hold Trajectory

In this section, the optimal trajectories and control outputs for the SE, with $\alpha_{\max}$ constrained to 75° (a), 65° (b), and 60° (c), are presented in Figures C.1, **??** and C.3. These additional figures support the discussion of cone-angle limitations in Section 3.1.2.

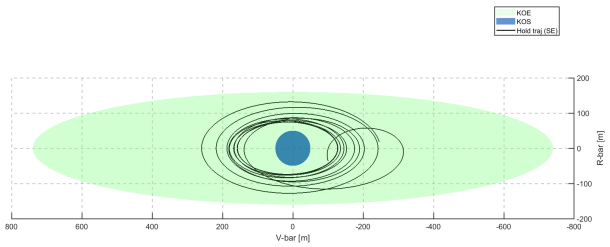

(a)

Figure C.1: Hold trajectory (SE) with maximum cone angle of 75° (a).

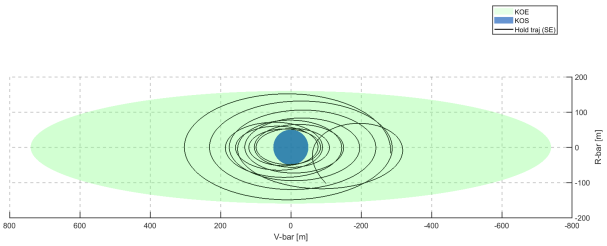

(a)

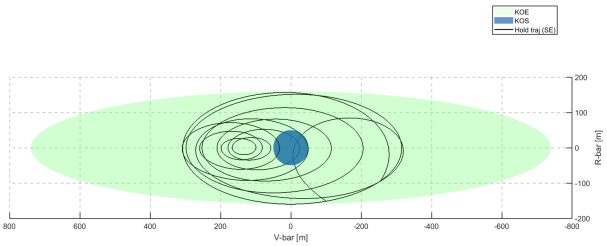

(b)

Figure C.2: Hold trajectories (SE) with maximum cone angles of 65° (b) and 60° (c).

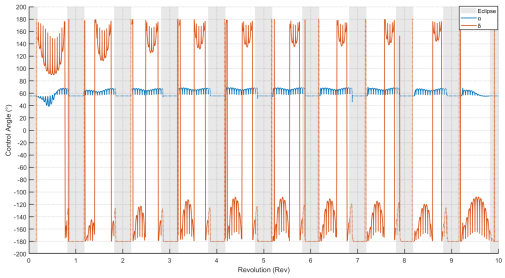

(a)

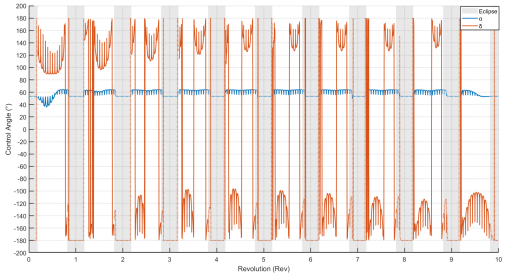

(b)

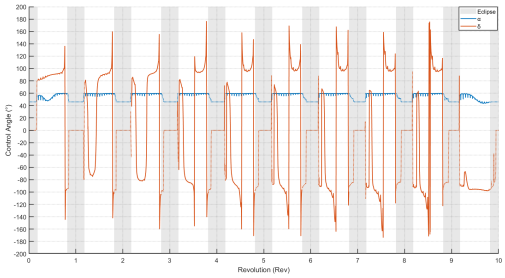

(c)

Figure C.3: Controls of Hold trajectory (SE) with maximum cone angles of 75° (a), 65° (b), and 60° (c).

Inspection Loop

In this section, we present the optimal trajectories and control outputs for the Inspection Loop (IL) in Cases 2 and 3 (Figures C.4 and C.5). These figures are not included in Section 3.2 because the resulting trajectories did not exhibit the desired walking-safety–ellipse behaviour. Although the optimization reached the target state points, the trajectories remained behind the KOE along the negative V-bar throughout the time-of-flight and never drifted over it, thus failing to produce the intended IL behaviour.

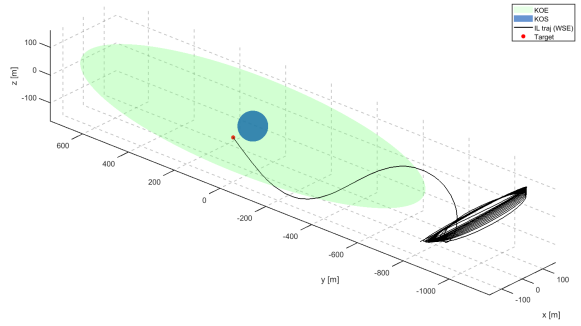

(a)

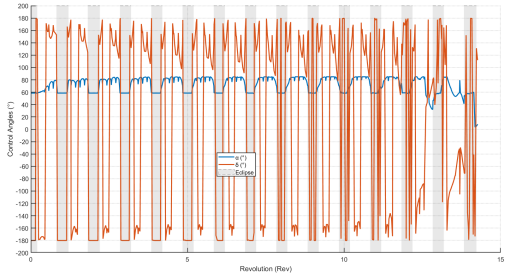

(b)

Figure C.4: IL trajectory Case 2 (a) and relative control (b).

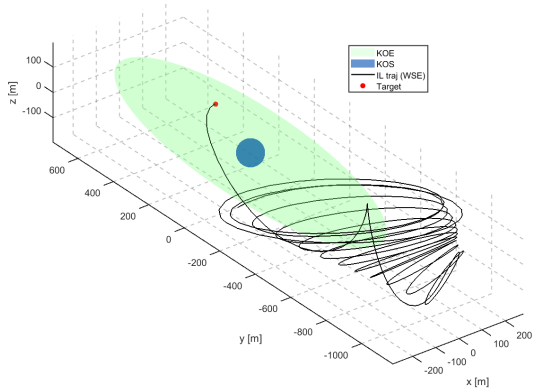

(a)

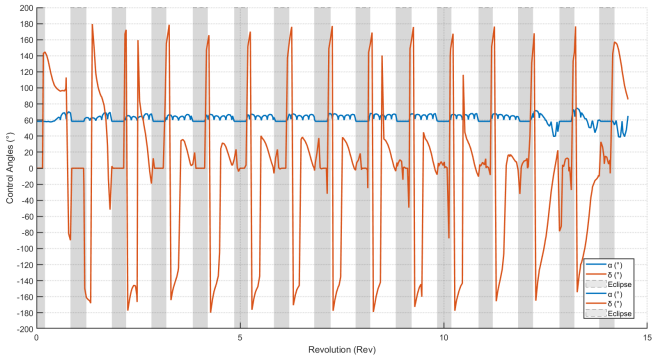

(b)

Figure C.5: IL trajectory Case 3 (a) and relative control (b).

Bibliography

[1] ESA Space Debris Office. *ESA's Annual Space Environment Report*. Tech. rep. GEN-DB-LOG-00288-OPS-SD. European Space Agency, 2025, p. 144 (cit. on pp. 1, 53, 65).

[2] T. S. Kelso and CelesTrak. *Iridium 33 and Cosmos 2251 Collision*. Accessed May 21, 2025. 2009. URL: https://celestrak.org/events/collision/ (cit. on p. 1).

[3] Debra Werner. *Major changes approved for ClearSpace-1 mission*. Accessed May 21, 2025. 2024. URL: https://spacenews.com/major-changes-approved-for-clearspace-1-mission/ (cit. on p. 1).

[4] D. Kessler, N. Johnson, J.-C Liou, and M. Matney. «The Kessler Syndrome: Implications to Future Space operations». In: *Advances in the Astronautical Sciences* 137 (2010) (cit. on p. 1).

[5] Donald J. Kessler and Burton G. Cour-Palais. «Collision frequency of artificial satellites: The creation of a debris belt». In: *Journal of Geophysical Research: Space Physics* 83.A6 (1978), pp. 2637–2646. DOI: 10.1029/JA083iA06p02637 (cit. on p. 1).

[6] ESA Space Debris Mitigation Working Group. *ESA Space Debris Mitigation Requirements*. Tech. rep. ESSB-ST-U-007. European Space Agency, 2023, Issue 1 (cit. on p. 2).

[7] Holger Krag. *Challenges Posed by Large Constellations*. 2019. URL: https://www.unoosa.org/documents/pdf/copuos/2019/Topic_2_Holger_Krag_Challenges_posed_by_large_constellations_20190611.pdf (cit. on p. 2).

[8] J.-C. Liou and N. L. Johnson. *A Sensitivity Study of the Effectiveness of Active Debris Removal in LEO*. Tech. rep. 20070013702. NASA Johnson Space Center, 2007 (cit. on p. 2).

[9] J.-C. Liou. «An active debris removal parametric study for LEO environment remediation». In: *Acta Astronautica* 66.5–6 (2010), pp. 648–653. DOI: 10.1016/j.asr.2011.02.003 (cit. on p. 2).

[10] Forshaw Jason L., Aglietti Guglielmo S., Fellowes Stuart, Retat Irvin, and et al. «The active space debris removal mission RemoveDebris. Part 1: From concept to launch». In: *Acta Astronautica* 168 (2019). DOI: 10.1016/j.actaastro.2019.09.002 (cit. on p. 2).

[11] Aleksander A. Lidtke, Toby Harris b, Cristina Perez Hernandezc, and et al. *SSA observation campaign of the ELSA-d mission*. 2022. URL: %7Bhttps://www.eusst.eu/sites/default/files/documents/IAC-22_ELSA-d.pdf%7D (cit. on p. 2).

[12] José Vasconcelos, Serena Gaggi, Tiago Amaral, and et al. «Close-Proximity Operations Design, Analysis, and Validation for Non-Cooperative Targets with an Application to the ClearSpace-1 Mission». In: *Aerospace* 12 (2025), p. 67. DOI: 10.3390/aerospace12010067 (cit. on pp. 2, 10).

[13] Colin R. McInnes. *Solar Sailing: Technology, Dynamics and Mission Applications*. Springer-Praxis Books in Astronautical Engineering. Springer-Verlag, 1999. ISBN: 978-1-85233-102-3. DOI: 10.1007/978-1-4471-3992-8 (cit. on pp. 2, 3, 12, 13).

[14] Les Johnson, Jason Everett, David McKenzie, and et al. *The NASA Solar Cruiser Mission – Solar Sail Propulsion Enabling Heliophysics Missions*. Tech. rep. 20220011260. NASA Marshall Space Flight Center, 2022 (cit. on p. 3).

[15] Keats Wilkie and Johnny Fernandez. *Advanced Composite Solar Sail System (ACS3) Mission Update*. Tech. rep. 20230008378. NASA Langley Research Center, 2023 (cit. on pp. 3, 10, 26, 54, 71).

[16] Wigbert Fehse. *Automated Rendezvous and Docking of Spacecraft*. Cambridge Aerospace Series. Cambridge University Press, 2003. ISBN: 9780521824927. URL: https://www.cambridge.org/9780521824927 (cit. on pp. 3, 7, 8).

[17] Christian Bianchi, Lorenzo Niccolai, Giovanni Mengali, and Matteo Ceriotti. «Preliminary design of a space debris removal mission in LEO using a solar sail». In: *Advances in Space Research* 73.8 (2024), pp. 4254–4268. DOI: https://doi.org/10.1016/j.asr.2024.01.024 (cit. on pp. 3, 4, 6, 15).

[18] P. Kelly and R. Bevilacqua. «An optimized analytical solution for geostationary debris removal using solar sails». In: *Acta Astronautica* 162 (2019), pp. 72–86. DOI: 10.1016/j.actaastro.2019.05.055 (cit. on pp. 3, 12).

[19] TU Delft. *SWEEP – Space Waste Elimination Around Earth by Photon Propulsion*. Accessed: 21 May 2025. URL: https://www.tudelft.nl/en/ae/sweep (cit. on p. 3).

[20] Markus Reichel. *Solar Sail Far-Range Rendezvous Operations For Active Debris Removal*. 2024. URL: http://resolver.tudelft.nl/uuid:847cf032-0944-4462-9b75-f32f6bef4dd6 (cit. on pp. 3, 4, 33, 66, 71, 72, 74, 78–80).

[21] G. Borelli, G. Gaias, and C. Colombo. «Rendezvous and proximity operations design of an active debris removal service to a large constellation fleet». In: *Acta Astronautica* 205 (2023), pp. 33–46. DOI: 10.1016/j.actaastro.2023.01.021 (cit. on pp. 4, 11, 41).

[22] L. Carzana, P. Visser, and J. Heiligers. «Locally optimal control laws for Earth-bound solar sailing with atmospheric drag». In: *Aerospace Science and Technology* 127.107666 (2022). DOI: 10.1016/j.ast.2022.107666 (cit. on p. 6).

[23] O. Montenbruck and E. Gill. *Satellite Orbits: Models, Methods, and Applications*. Springer, 2012. ISBN: 978-3-540-67280-7. DOI: 10.1007/978-3-642-58351-3 (cit. on pp. 7, 65).

[24] Vavrina, Skelton C, Deweese Keith, Naasz Bo, Gaylor David, and D'souza Christopher. *SAFE RENDEZVOUS TRAJECTORY DESIGN FOR THE RESTORE-L MISSION*. 2019. URL: https://www.researchgate.net/publication/330545815_SAFE_RENDEZVOUS_TRAJECTORY_DESIGN_FOR_THE_RESTORE-L_MISSION (cit. on p. 10).

[25] Kovacic Aleksandar, Siminski Jan, Merz Klaus, Burgis Simon, and Bertrand Reinhold. *Modelling and assessment of the impact of new space surveillance systems on sustainable spacecraft operations*. 2023. URL: https://ui.adsabs.harvard.edu/abs/2023sndd.confE...6K (cit. on p. 10).

[26] A. Comelllini, J. Vasconcelos, and K. McHugh. *Verification and Validation of Rendezvous and Proximity Operations Safety*. 2024. URL: https://nebula.esa.int/sites/default/files/neb_tec_study/2569/public/Executive%20Summary%20Report_Adina%20Cotuna.pdf (cit. on p. 10).

[27] eo Portal. *PROBA-1 (Project for On-Board Autonomy)*. Accessed May 21, 2025. 2024. URL: https://www.eoportal.org/satellite-missions/proba-1#mission-status (cit. on p. 10).

[28] Eijiro Atarashi, Hisashi Inoue, and Gene Fujii. *Ultra-close RPO On-Orbit Demonstration of the ADRAS-J Programme*. 2024. URL: https://iafastro.directory/iac/archive/tree/IAC-24/A6/6/IAC-24,A6,6,9,x87881.brief.pdf (cit. on pp. 10, 11).

[29] Markus Wilde. *CEU Session#4 - Space Robotics for On-Orbit Servicing and Space Debris Removal*. Presented at the 46th Space Congress, Session on Space Robotics. 2019. URL: https://commons.erau.edu/space-congress-proceedings/proceedings-2019-46th/presentations/3/ (cit. on p. 11).

[30] B. Dachwald. *Low-thrust trajectory optimization and interplanetary mission analysis using evolutionary neurocontrol*. 2004. URL: https://www.researchgate.net/publication/224787023_Low-Thrust_Trajectory_Optimization_and_Interplanetary_Mission_Analysis_Using_Evolutionary_Neurocontrol/citations (cit. on p. 13).

[31] Howard D. Curtis. *Orbital Mechanics for Engineering Students*. Elsevier, 2005. ISBN: 0 7506 6169 0. DOI: 10.1016/b978-0-08-102133-0.09982-7 (cit. on pp. 15, 16, 68, 69).

[32] Aziz, Jonathan, Scheeres D., PARKER Jeffrey, and Englander Jacob. «A Smoothed Eclipse Model for Solar Electric Propulsion Trajectory Optimization». In: *Transactions of the Japan Society for Aeronautical and Space Sciences, Aerospace Technology Japan* 17 (2019). DOI: 10.2322/tastj.17.181 (cit. on pp. 15, 70).

[33] Karel F. Wakker. *Fundamentals of Astrodynamics*. Delft University of Technology, 2015. ISBN: 978-94-6186-449-2. URL: https://repository.tudelft.nl (cit. on pp. 16, 65).

[34] David E. Gaylor and Brent William Barbee. «Algorithms for Safe Spacecraft Proximity Operations». In: *Advances in the Astronautical Sciences* 127 (2007), pp. 133–152. URL: https://www.researchgate.net/publication/287006615 (cit. on p. 17).

[35] Bo J. Naasz. *Safety Ellipse Motion with Coarse Sun Angle Optimization*. Tech. rep. 2005213556. NASA Goddard Space Flight Center, 2005 (cit. on pp. 17–19).

[36] Simone Fortuna. *Autonomous Rendezvous with a Non-Cooperative Satellite: Trajectory Planning and Control*. 2022. URL: https://thesis.unipd.it/retrieve/4818eeb2-1ce3-4ec0-89bd-45457b7e2be1/Fortuna_Simone.pdf (cit. on p. 17).

[37] Anil V. Rao. «A Survey of Numerical Methods for Optimal Control». In: *Advances in the Astronautical Sciences* 135 (2010). URL: https://www.researchgate.net/publication/268042868_A_Survey_of_Numerical_Methods_for_Optimal_Control (cit. on p. 20).

[38] John T. Betts. «Survey of Numerical Methods for Trajectory Optimization». In: *Journal of Guidance, Control, and Dynamics* 21.2 (1998), pp. 193–207. DOI: 10.2514/2.4231 (cit. on pp. 20, 66).

[39] David Morante, Manuel Sanjurjo Rivo, and Manuel Soler. «A Survey on Low-Thrust Trajectory Optimization Approaches». In: *Aerospace* 8.3 (2021), p. 88. DOI: 10.3390/aerospace8030088 (cit. on pp. 20–22).

[40] Michael A. Patterson and Anil V. Rao. «GPOPS-II: A MATLAB Software for Solving Multiple-Phase Optimal Control Problems Using hp-Adaptive Gaussian Quadrature Collocation Methods and Sparse Nonlinear Programming». In: *ACM Transactions on Mathematical Software* 41.1 (2014), 1:1–1:37. DOI: 10.1145/2558904 (cit. on pp. 20, 24, 25).

[41] Michael A. Patterson and Anil V. Rao. *GPOPS-II User's Guide: A General-Purpose MATLAB Software for Solving Multiple-Phase Optimal Control Problems*. 2016. URL: https://gpops2.com/resources/gpops2UsersGuide.pdf (cit. on pp. 20, 85).

[42] Topputo Francesco and Zhang Chen. «Survey of Direct Transcription for Low-Thrust Space Trajectory Optimization with Applications». In: *Abstract and Applied Analysis* 2 (2014), pp. 1–15. DOI: 10.1155/2014/851720 (cit. on p. 23).

[43] Ehsan Taheri and John L. Junkins. «Generic smoothing for optimal bang-off-bang spacecraft maneuvers». In: *Journal of Guidance, Control, and Dynamics* 41.11 (2018), pp. 2467–2472. DOI: 10.2514/1.G003604 (cit. on p. 29).

[44] Ryu Namhee and Min Seungjae. «Multiobjective optimization with an adaptive weight determination scheme using the concept of hyperplane». In: *International Journal for Numerical Methods in Engineering* 118.5 (2019), pp. 303–319. DOI: 10.1002/nme.6013 (cit. on p. 29).

[45] Pezent James, Sood Rohan, and Heaton Andrew. *Near Earth Asteroid (NEA) Scout Solar Sail Contingency Trajectory Design and Analysis*. 2018. DOI: 10.2514/6.2018-0199 (cit. on p. 34).

[46] Capuano Vincenzo, Saggiomo Fabio, Capuano Giuseppe, and et al. *SpEye: a CubeSat Technology Demonstration Mission for On-Orbit Inspection and Formation-Flying*. 2024. DOI: 10.52202/078365-0095 (cit. on p. 41).

[47] Gámez Losada F., P.N.A.M. Visser, and M.J. Heiligers. *Fundamentals of Solar-Sail Transfers Around Planetary Bodies*. 2024. URL: https://pure.tudelft.nl/ws/portalfiles/portal/219993906/ISSFDPaper_v5.0.pdf (cit. on p. 52).

[48] Lu Ping and Liu Xinfu. «Autonomous Trajectory Planning for Rendezvous and Proximity Operations by Conic Optimization». In: *Journal of Guidance Control and Dynamics* 36 (2013), pp. 375–389. DOI: 10.2514/1.58436 (cit. on p. 66).

[49] R. Volpe, C. Circi, and G. B. Palmerini. «Selecting Optimal Inspection Trajectories for Target Observation». In: *Aerotecnica Missili & Spazio* 97.2 (2018), pp. 60–67. DOI: 10.1007/BF03405801 (cit. on p. 66).

[50] C. Bonnal and D. S. McKnight. *IAA Situation Report on Space Debris 2016*. 2017. URL: https://iaaspace.org/wp-content/uploads/iaa/Scientific%20Activity/sg514finalreport.pdf (cit. on p. 71).